



## Luminous Team Final Report

Davide Sferlazzo (10565137)

[davide.sferlazzo@mail.polimi.it](mailto:davide.sferlazzo@mail.polimi.it)

Satwik Mohanty (10992699)

[satwik.mohanty@mail.polimi.it](mailto:satwik.mohanty@mail.polimi.it)

Francesco Scali (10614337)

[francesco.scali@mail.polimi.it](mailto:francesco.scali@mail.polimi.it)

Federico Marangi (10933713)

[federico.marangi@mail.polimi.it](mailto:federico.marangi@mail.polimi.it)

Louis Richard (10901804)

[louisolivier.richard@mail.polimi.it](mailto:louisolivier.richard@mail.polimi.it)

Andrea Favalli (10680576)

[andrea3.favalli@mail.polimi.it](mailto:andrea3.favalli@mail.polimi.it)

Gianluca Spigarelli (10682851)

[gianluca.spigarelli@mail.polimi.it](mailto:gianluca.spigarelli@mail.polimi.it)

Samuele Vincenzi (10706415)

[samuele.vincenzi@mail.polimi.it](mailto:samuele.vincenzi@mail.polimi.it)

Amirhossein Kermani (10862181)

[amirhossein.kermani@mail.polimi.it](mailto:amirhossein.kermani@mail.polimi.it)

Davide Bua (10520668)

[davide.bua@mail.polimi.it](mailto:davide.bua@mail.polimi.it)

Davide Gianmoena (10613858)

[davide.gianmoena@mail.polimi.it](mailto:davide.gianmoena@mail.polimi.it)

Kail Malatesta (10697364)

[kail.malatesta@mail.polimi.it](mailto:kail.malatesta@mail.polimi.it)

# Nomenclature

## Symbols

$\Delta v$	Change of speed	[m/s]
$\varepsilon$	Efficiency	[−]
$\mu$	Planetary constant	[m <sup>3</sup> /s <sup>2</sup> ]
$A$	Area	[m <sup>2</sup> ]
$c$	Speed of light	[m/s]
$C$	Capacity	[Wh]
$D$	Generic distance	[m]
$F_s$	Solar constant	[W/m <sup>2</sup> ]
$I$	Specific power	[W/m <sup>2</sup> ]
$P$	Power	[W]
$R$	spacecraft ( <a href="#">s/c</a> ) distance from planet	[m]
$T$	Period	[s]
$V$	Voltage	[V]
$H$	Albedo	[−]
$q$	Electric charge	[Ah]

# Acronyms

<b>ADCS</b>	Attitude Determination and Control System	<b>FACT</b>	Flexible Array Concentrator Technology
<b>AO</b>	Atomic Oxigen	<b>FOV</b>	Field of View
<b>AO</b>	Atomic Oxigen	<b>GCR</b>	Galactic Cosmic Rays
<b>APME</b>	Antenna Pointing Mechanism Electronic	<b>GMSK</b>	Gaussian Minimum Shift Keying
<b>AU</b>	Astronomical unit	<b>GNC</b>	Guidance, Navigation and Control
<b>BER</b>	Bit Error Rate	<b>GOES-U</b>	Geostationary Operational Environmental Satellite - U
<b>BOL</b>	Begin Of Life	<b>GS</b>	Ground Station
<b>BPSK</b>	Binary Phase Shift Keying	<b>GTO</b>	Geostationary Transfer Orbit
<b>CC</b>	Constant Current	<b>HGA</b>	High Gain Antenna
<b>CCCV</b>	Constant Current Constant Voltage	<b>HK</b>	House Keeping
<b>CCD</b>	Charge Coupled Device	<b>HLO</b>	High Lunar Orbit
<b>CCOR</b>	Compact CORonagraph	<b>IMU</b>	Inertial Measurement Unit
<b>CME</b>	Coronal Mass Ejection	<b>IPS</b>	Instructions Per Second
<b>CoG</b>	Center of Gravity	<b>ITU</b>	International Telecommunication Union
<b>COTS</b>	Commercial off-the-shelf	<b>JPL</b>	Jet Propulsion Laboratory
<b>CPU</b>	Central Processing Unit	<b>LASCO</b>	Large Angle Spectroscopic Coronagraph
<b>CRTBP</b>	Circular Restricted Three Bodies Problem	<b>LEO</b>	Low Earth Orbit
<b>CV</b>	Constant Voltage	<b>LGA</b>	Low Gain Antenna
<b>DET</b>	Direct Energy Transfer	<b>LTI</b>	Lunar Transfer Injection
<b>DMM</b>	Design Maturity Margin	<b>LTO</b>	Lunar Transfer Orbit
<b>DOD</b>	Depth of Discharge	<b>MA</b>	Mission Analysis
<b>DoF</b>	Degree of Freedom	<b>MJ</b>	Multi-Junction
<b>DRO</b>	Distant Retrograde Orbit	<b>MLI</b>	Multi-Layer Insulation
<b>DSB</b>	Data Storage Boards	<b>MMOD</b>	Micro-Meteoroid Orbital Debris
<b>ECC</b>	Error Correction Code	<b>NICM</b>	NASA Instrument Cost Model
<b>ECSS</b>	European Cooperation for Space Standardization	<b>NRHO</b>	Near-Rectilinear Halo Orbit
<b>EOL</b>	End Of Life	<b>OBDH</b>	On-Board Data Handling
<b>EPS</b>	Electrical Power Subsystem	<b>PBRFBP</b>	Planar Bicircular Restricted Four-Body Problem
<b>ESD</b>	ElectroStatic Discharge	<b>PCDU</b>	Power Control & Distribution Unit
<b>ESA</b>	European Space Agency	<b>PL</b>	Payload
<b>EVA</b>	Extra Vehicular Activity	<b>PPT</b>	Peak Power Tracking
		<b>PS</b>	Propulsion Subsystem



<b>PSP</b>	Parker Solar Probe	<b>SLM</b>	System Level Margin
<b>PVDF</b>	Polyvinylidene Flouride	<b>SMEI</b>	Solar Mass Ejection Imager
<b>QPSK</b>	Quadrature Phase Shift Keying	<b>SOHO</b>	Solar and Heliospheric Observatory
<b>RAAN</b>	Right Ascension of the ascending node	<b>SRP</b>	Solar Radiation Pressure
<b>RAM</b>	Random Access Memory	<b>SSAK</b>	Single-Sided Aluminised Kapton
<b>ROM</b>	Read Only Memory	<b>SUROM</b>	Start Up Read Only Memory
<b>RTG</b>	Radioisotope Thermonuclear Generator	<b>SPO</b>	Short Periodic Orbits
<b>RW</b>	Reaction Wheels	<b>TCS</b>	Thermal Control Subsystem
<b>RWU</b>	Reaction Wheel Unit	<b>TJ</b>	Triple-Junction
<b>s/c</b>	spacecraft	<b>TOF</b>	Time of Flight
<b>s/s</b>	subsystem	<b>TRL</b>	Technology Readiness Level
<b>SA</b>	Solar Arrays	<b>TTMTC</b>	Tracking,Telemetry and Telecommand
<b>SAA</b>	Sun Aspect Angle	<b>TWTA</b>	Travelling Wave Tube Amplifier
<b>SADA</b>	Solar Array Drive Assembly	<b>UV</b>	Ultra Violet
<b>SK</b>	station keeping	<b>VAB</b>	Van Allen Belts

# Contents

<b>1</b>	<b>Mission Overview</b>	<b>1</b>
1.1	Mission stimuli . . . . .	1
1.2	High Level Objectives . . . . .	1
1.2.1	Primary Objectives . . . . .	1
1.2.2	Secondary Objectives . . . . .	1
1.2.3	Fundamental Requirements . . . . .	2
1.3	Payloads overview . . . . .	2
1.3.1	Primary payload . . . . .	2
1.3.2	Secondary payload . . . . .	2
1.4	Environment . . . . .	3
1.4.1	Solar activity . . . . .	3
1.4.2	Cis-lunar environment . . . . .	3
1.4.3	Lunar gravity perturbations . . . . .	4
1.4.4	Lunar magnetic Field . . . . .	5
1.4.5	Lunar Wake . . . . .	5
1.4.6	Environmental effect on orbit . . . . .	5
1.5	Modeling of environmental effects . . . . .	5
1.5.1	Sun and Geomagnetic activity indexes . . . . .	6
1.5.2	Plasma environment . . . . .	6
1.5.3	Solar wind . . . . .	8
1.5.4	Solar particles . . . . .	8
<b>2</b>	<b>Mission Analysis</b>	<b>1</b>
2.1	Solar Corona Observation . . . . .	1
2.1.1	Scientific input . . . . .	1
2.1.2	Observation Model . . . . .	1
2.1.3	Observation Quality parameters . . . . .	2
2.2	High-level alternatives . . . . .	3
2.2.1	Earth solution . . . . .	3
2.2.2	Earth-Moon system solutions . . . . .	4
2.2.3	Moon solutions . . . . .	6
2.3	Moon Orbits . . . . .	6
2.3.1	Moon orbit - Final choice . . . . .	6
2.3.2	Example of the applied strategy . . . . .	11
2.4	Transfer to chosen orbit . . . . .	13
2.4.1	Best transfer . . . . .	13
2.4.2	Other transfers . . . . .	14
2.4.3	Trade-offs and margins . . . . .	14
2.5	Future Developments . . . . .	16
2.6	Disposal . . . . .	17



2.7	Launcher selection . . . . .	19
2.7.1	Launch location . . . . .	19
2.8	Conceptual Operations . . . . .	20
2.8.1	Mission ConOps . . . . .	20
2.8.2	Orbit ConOps . . . . .	21
<b>3</b>	<b>Attitude Determination and Control Subsystem</b>	<b>23</b>
3.1	Attitude Determination . . . . .	23
3.1.1	IMU . . . . .	23
3.1.2	Star Trackers . . . . .	23
3.2	Out-Of-Eclipse Attitude Strategies . . . . .	24
3.2.1	Proposal A: <i>Permanent Earth Visibility</i> . . . . .	25
3.2.2	Proposal B: <i>Modified Nadir Pointing</i> . . . . .	25
3.2.3	Conjunctions . . . . .	25
3.2.4	Trade-off: statement . . . . .	26
3.2.5	Trade-off: analysis . . . . .	27
3.2.6	Trade-off: conclusions . . . . .	29
<b>4</b>	<b>Propulsion Subsystem</b>	<b>30</b>
4.1	Trade-off analysis . . . . .	30
4.1.1	Primary propulsion . . . . .	32
4.1.2	Secondary propulsion . . . . .	32
4.2	Architecture . . . . .	32
4.2.1	Thrust and engine selection . . . . .	34
4.2.2	Pressurization system . . . . .	34
4.2.3	Tanks . . . . .	34
4.3	Propulsion system sizing . . . . .	35
4.3.1	Primary propulsion sizing . . . . .	35
4.3.2	Secondary propulsion sizing . . . . .	36
4.3.3	Total masses and volumes of propellant . . . . .	36
4.3.4	Pressurization system sizing . . . . .	36
4.3.5	Tank sizing . . . . .	37
<b>5</b>	<b>TTMTC</b>	<b>38</b>
5.1	Input data from other subsystems . . . . .	38
5.2	Communication operations . . . . .	38
5.3	Visibility windows . . . . .	39
5.4	Sizing and Justification of the architecture . . . . .	39
5.4.1	Groundstation . . . . .	39
5.4.2	On-Board architecture . . . . .	41
5.5	International Telecommunication Union (ITU) Regulations . . . . .	42
5.6	Link Budget . . . . .	42
5.6.1	Results of the link margin . . . . .	44
5.7	Effects of the Tracking, Telemetry and Telecommand (TTMTC) Subsystem on the other Subsystems . . . . .	44
5.7.1	TTMTC Mass budget . . . . .	44
5.7.2	TTMTC Thermal Budget . . . . .	44



5.7.3	TTMTC power Budget . . . . .	45
5.7.4	TTMTC's effect on the OBDH . . . . .	45
5.7.5	TTMTC Pointing budget . . . . .	45
<b>6</b>	<b>Electric Power Subsystem</b>	<b>46</b>
6.1	Power source . . . . .	46
6.1.1	Solar cells: Si-based . . . . .	47
6.1.2	Solar cells: multi-junction . . . . .	47
6.1.3	Solar cells: thin cells . . . . .	48
6.1.4	Nuclear power . . . . .	49
6.2	Energy storage . . . . .	49
6.2.1	Ni-Cd batteries . . . . .	50
6.2.2	Ni-H <sub>2</sub> batteries . . . . .	50
6.2.3	Li-ion batteries . . . . .	50
6.2.4	Li-S batteries . . . . .	50
6.2.5	Supercapacitors . . . . .	50
6.3	Power Regulation and Control . . . . .	51
6.4	Design rationale . . . . .	51
6.5	Results . . . . .	53
<b>7</b>	<b>Thermal Control Subsystem</b>	<b>55</b>
7.1	Problem Definition . . . . .	55
7.1.1	Temperature ranges . . . . .	55
7.1.2	Heating environments . . . . .	56
7.2	Preliminary analysis: single-node approximation . . . . .	56
7.3	Refined analysis: multi-node analysis and thermal network . . . . .	57
7.3.1	Thermal Network Description . . . . .	58
7.3.2	Heat transfer assumptions . . . . .	58
7.3.3	Results and comments . . . . .	59
7.4	Mass and Power computations . . . . .	59
7.4.1	Mass budget for the TCS . . . . .	60
7.4.2	Power budget for the TCS . . . . .	60
7.5	Future Developments . . . . .	60
<b>8</b>	<b>On-Board Data Handling Subsystem</b>	<b>62</b>
8.0.1	Partitioning of functionalities and preliminary trade-offs . . . . .	62
8.0.2	Resource needs estimation . . . . .	62
8.0.3	Selection of components . . . . .	64
<b>9</b>	<b>Configuration Subsystem Overview</b>	<b>65</b>
9.1	Introduction to Configuration Subsystem . . . . .	65
9.2	Spacecraft Shape Trade-off . . . . .	65
9.2.1	Initial Dimension for Inertia Matrix Calculation Methodology and Assumptions . . . . .	66
9.3	Final System Architecture . . . . .	66
9.4	Payload . . . . .	67
9.5	Propulsion Module . . . . .	67
9.5.1	Thrusters . . . . .	68



9.5.2 Propellant tanks (Fuel and Oxidizer) . . . . .	68
9.5.3 Pressurizing gas tank . . . . .	69
9.6 Solar Array . . . . .	69
9.7 Electrical power management module . . . . .	70
9.8 Antennae and OBDH . . . . .	71
9.8.1 High Gain Antenna . . . . .	72
9.8.2 Low Gain Antennas . . . . .	72
9.8.3 On Board Computer and Transceivers . . . . .	72
9.9 Actuators and Sensors . . . . .	72
9.10 Launch configuration . . . . .	73
<b>10 Structures</b> . . . . .	<b>74</b>
10.1 Material selection . . . . .	74
10.1.1 Aluminum 7075, T6 . . . . .	74
10.1.2 Titanium - Ti-6Al-2Sn-2Zr-2Mo (annealed) . . . . .	75
10.2 Modal Analysis . . . . .	75
10.2.1 Natural Frequency of LUMINOUS spacecraft . . . . .	75
10.2.2 Vibration Damper during Launch . . . . .	76
10.3 Static Structural Analysis . . . . .	77
10.3.1 Assumptions . . . . .	77
10.3.2 Equivalent stress(Von Mises) . . . . .	78
10.3.3 Safety Factor . . . . .	79
10.3.4 Total Deformation . . . . .	80
10.4 Science Mode Damping System . . . . .	80
10.4.1 Effect on the Electrical Power Subsystem (EPS) subsystem . . . . .	83
<b>11 FDIR, Development Plan and Cost Estimation</b> . . . . .	<b>84</b>
11.1 Fault Detection, Identification, and Recovery . . . . .	84
11.1.1 Mission criticalities . . . . .	84
11.1.2 Subsystems criticalities . . . . .	84
11.2 Development plan . . . . .	85
11.3 Preliminary Cost Estimation . . . . .	86
11.3.1 Spacecraft . . . . .	86
11.3.2 Payloads . . . . .	87
11.3.3 Primary launcher . . . . .	87
11.3.4 Results . . . . .	88
<b>12 System budgets</b> . . . . .	<b>89</b>
12.1 Mass budget . . . . .	89
12.2 Power budget . . . . .	90
<b>A Solar particles</b> . . . . .	<b>99</b>
<b>B Thermal Control Subsystem</b> . . . . .	<b>105</b>
B.1 TCS - Single Node Assumptions . . . . .	105
B.1.1 Planetary Data . . . . .	105
B.1.2 Orbital Data . . . . .	105



B.1.3	Spacecraft and material properties . . . . .	105
B.2	TCS - single-node computations . . . . .	106
B.2.1	Heat fluxes . . . . .	106
B.3	Heat Power . . . . .	106
B.4	Temperature, radiators, heaters . . . . .	108
B.4.1	Spacecraft Temperature and radiators . . . . .	108
B.4.2	Spacecraft Temperature and heaters . . . . .	108
B.5	TCS - thermal network computations . . . . .	109
B.5.1	Sink temperature . . . . .	109
B.5.2	View Factors . . . . .	109
<b>C</b>	<b>EPS sizing</b>	<b>110</b>
C.1	Preliminary analysis . . . . .	110
C.2	Solar arrays sizing . . . . .	110
C.3	Batteries sizing . . . . .	111
<b>D</b>	<b>EPS datasheets</b>	<b>112</b>
<b>E</b>	<b>Structures</b>	<b>115</b>
<b>F</b>	<b>PS datasheet</b>	<b>116</b>
F.1	Pressurization system sizing . . . . .	118
F.2	Tank sizing . . . . .	118
<b>G</b>	<b>OBDH datasheets</b>	<b>119</b>

# Abstract

Since the start of human space exploration, the Sun has been one of the biggest environmental challenges to be faced and studied. While studying the solar disc is achievable, the solar corona has been, and still is, one of the biggest mysteries of solar weather. Indeed, the Inner Corona cannot be studied in detail due to the architecture of every classic coronagraph, since the built-in obscurer reduces resolution and partially impedes visibility. The Lunar Utilization for Monitoring INteraction of OUter Solar Structures (LUMINOUS) mission aims to exploit the Moon as an external obscurer that could, thanks to its surface morphology and distance from the coronagraph, significantly improve observation of both the Inner and Outer solar corona. This report shows the feasibility study of one such spacecraft, considering all mission phases including disposal, and suggesting solutions for each subsystem. Mission overview is presented in the first chapter, with particular focus on objectives, high level requirements and payloads (whose design is inherited). Mission analysis is carried out next; the rationale for the selection of the operative orbit is detailed, and robust strategies for transfer, station-keeping and disposal are proposed. Being the Moon-centred orbit fixed as a baseline, the discussion shifts its focus on the trade-offs for solutions at subsystem level and their coherent integration in the final architecture, as well as on margin philosophy and redundancy of components to grant survivability until the planned disposal after six years operativity. The final proposed orbiter employs medium-high TRL technologies that can effectively translate into mission start before the end of the actual decade. It exploits state-of-the-art star trackers, reaction wheels and IMU for precise pointing of payloads, high gain antenna and solar arrays (which have one degree of freedom thanks to the use of solar array drive assemblies), while relying on chemical solutions for propulsion needs. After mass and power budgets are presented, high-level risk analysis, development plan and cost analysis are briefly discussed.

# Chapter 1 Mission Overview

## 1.1 Mission stimuli

The scientific advantages of using the lunar disc to produce eclipses are extensively explained in [1], a study that concentrates on the technical requirements and comparisons with classic coronagraphs of the to-be-developed payload. However, the cited article does not provide the feasibility study of a mission in the required environment and orbit, from this vacuum of information the LUMINOUS project is born. In Table 1.1 are presented the main advantages of observing the solar corona through the Lunar limb, as presented in [1], compared to the *Large Angle Spectroscopic Coronagraph (LASCO)* [2] and the *Compact CORonagraph (CCOR)* [3] payloads, respectively from *Solar and Heliospheric Observatory (SOHO)* and *Geostationary Operational Environmental Satellite - U (GOES-U)* missions.

Parameter	LASCO (1995)	CCOR (2024)	LUMINOUS (2027>)
Field of view [ $R_{Sun}$ ]	[1.2 - 32]	[3.7 - 17]	>1.002
Max brightness reduction [ $B_{Sun}$ ]	$10^{-12}$	$10^{-11}$	$10^{-14}$
Image resolution [arcsec/pixel]	5.6	33	0.7

**Table 1.1:** Comparison of existent coronagraphs and LUMINOUS

As can be easily noticed in Table 1.1, the Lunar Limb provides multiple advantages when confronted with man-made obscurers. Firstly, the Lunar morphology only covers a minuscule part of the solar corona, allowing for an FOV that goes down to the thousandth of solar radii, while contemporarily being smooth enough to grant an image resolution lower than the arcsecond. Both of these conditions would allow for a breakthrough in solar observation; in addition, the Lunar limb can also reduce the incoming light to 2 orders of magnitudes lower than a classical obscurer, allowing for more precise observation, while having a disturbance of the same order as background stellar disturbance, which is the typical value of classical operating coronagraphs [1].

## 1.2 High Level Objectives

The LUMINOUS mission aims to study the solar corona through the exploitation of the lunar disc as an obscurer. The main objectives and requirements for the success of the mission are reported hereafter.

### 1.2.1 Primary Objectives

- Map coronal temperature and density gradients
- Understand how the magnetic field in the solar wind source regions connects to the photosphere and heliosphere
- Understand sources of the solar wind to be steady or intermittent
- Study the evolution of structures in the corona into the solar wind

### 1.2.2 Secondary Objectives

- Search for potentially hazardous objects with perihelia inward of Earth's orbit
- Study the interaction at the limb between lunar surface dust and the Sun

### **1.2.3 Fundamental Requirements**

- Exploit the Moon disc as Sun occulter
  - Maximise the observation period
  - Launch date shall be after 01/01/2027
  - Operational life shall be at least 6 years (representing half of the solar cycle)

## 1.3 Payloads overview

As explained, the objective of this paper is to study the feasibility of the mission and does not account for payload development. Nevertheless, for the development of LUMINOUS, mass and power budget shall be allocated for the payloads, as well as a rough number for data production and pointing precision, therefore the following have been chosen as payload templates. Of course, an ad-hoc payload shall be developed both for primary and secondary objectives to consider this mission a complete success.

### 1.3.1 Primary payload

The very same Compact CORonagraph [3] mentioned in Table 1.1 is a good template for the mission: it has a mass of only 25kg (including the occulter) and its main purpose is white imaging of the solar corona. It has a 15-minute refresh rate and a maximum acquisition time of 30 seconds. It is also the direct descendant of LASCO, being developed by the same laboratory, giving clear evidence that the development intention of future coronagraphs tends towards miniaturization (as expected).

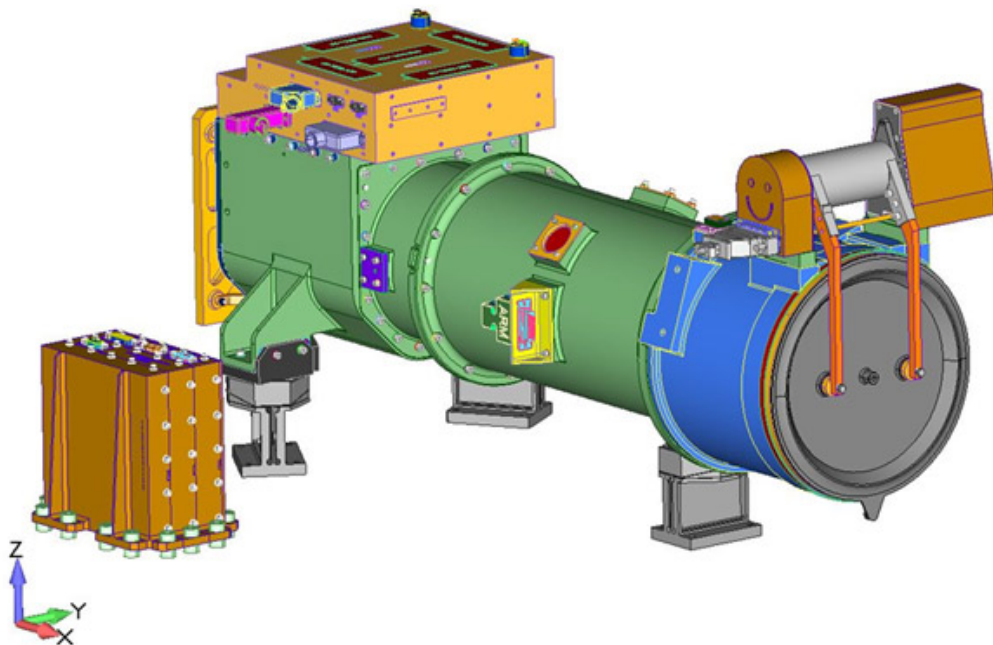


**Figure 1.1:** CAD image of the Compact CORonograph, including obscurer

### 1.3.2 Secondary payload

The Solar Mass Ejection Imager ([SMEI](#)) [4] has been chosen as a template for the secondary payload. The camera is sensitive enough to not only study mass ejections but also detect asteroids and comets, confirmed by the multiple instances of NEA objects identified by this instrument. The instrument is composed of 3 cameras, but only one has been considered as a template.



## 1.4 Environment

### 1.4.1 Solar activity

Tracking solar activity along the mission operative lifetime is both a mission enabler and a mission objective. Indeed, the Sun is a dynamic entity whose activity evolves following regular cycles of around 11 years, with a direct influence on space weather and thus on *s/c* survivability and operations [5].

In a first approximation, the Sun can be modeled as a giant thermonuclear reactor that radiates as a black body: 95% of emitted particles consists of protons and electrons, the rest being heavy ions. Darker regions of the photosphere characterized by low temperature and high magnetic activity are referred to as sunspots. When the number of sunspots increases, the Sun's activity hits the maximum: electromagnetic and mass emissions are experienced, with the generation of flares and intense, localized eruptions of electromagnetic radiation in the heliosphere. A Coronal Mass Ejection (CME) is a significant ejection of magnetic field transferring plasma mass from the Sun's corona into the heliosphere; it is related to flares and it is particularly dangerous for astronauts, especially if performing Extra Vehicular Activity (EVA)s [6]. The plasma ejected from the Sun travels in space, generating the Solar Wind. In Figure 1.2 and Figure 1.3 the Solar Cycle Progression and Forecast provided by the Space Environments Team in the Natural Environments Branch of the Engineering Directorate at Marshall Space Flight Center [7] is shown. From 2023 on, data is retrieved statistically; the minimum in solar activity is pointed around the year 2031, while the maximum should be around 2035/2036 [8].

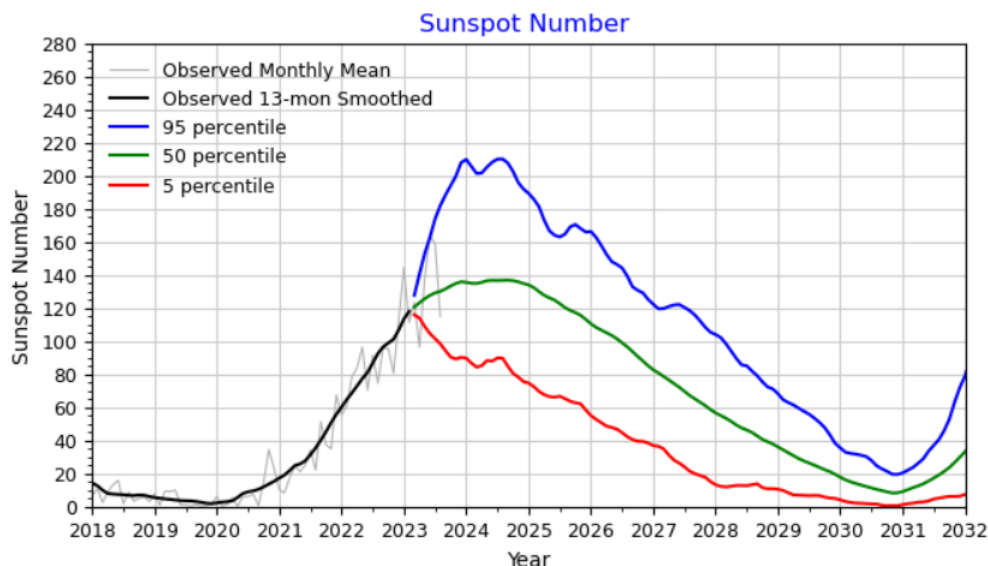


**Figure 1.2:** Sunspot number prediction up to 2032

Solar irradiance in the cis-lunar environment lies approximately in the range  $1300 \text{ W/m}^2$ -  $1430 \text{ W/m}^2$ , depending on the *s/c* position inside the Moon sphere of influence.

The solar wind can affect the EPS, Thermal Control Subsystem (TCS), and TTMTC, but at the same time, it shields the *s/c* against Galactic Cosmic Rays (GCR), highly energetic particles reaching energy above  $10^{20}$  eV.

### 1.4.2 Cis-lunar environment

Earth's atmospheric effects can be totally neglected above 2000 km of altitude, and drag, magnetic, and gravity gradient torques vanish as well. To reach the Moon, the *s/c* will have to cross the high energetic environment of the Van Allen Belts (VAB) and exit the magnetosphere of the Earth, being directly exposed to the solar wind particles. The effects of particle strikes are several, all equally dangerous; moreover, secondary emission shall be taken into account, since it has a relevant role in noise production ("background signal") for detector systems [9]. With regard to LUMINOUS mission, displacement damage from a direct strike might mean a single-point failure if one of the Charge Coupled Device (CCD) embedded in the payload is hit.

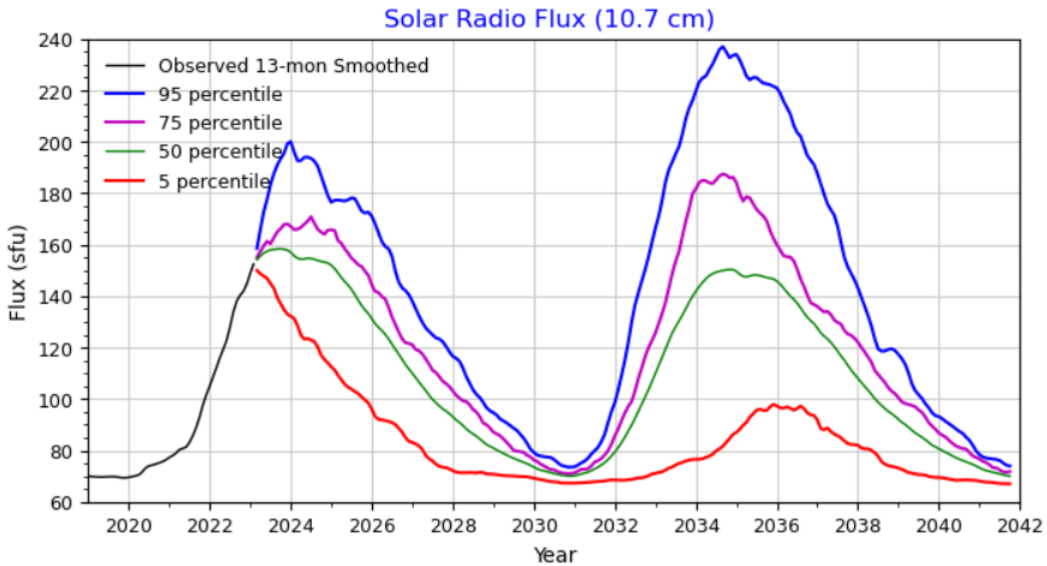


**Figure 1.3:** Solar Radio Flux (10.7 cm) prediction up to 2042

### 1.4.3 Lunar gravity perturbations

Based on the Earth's mass and shape properties, the  $J_2$  perturbation is a few orders higher than the other harmonics. On the other hand, the lunar  $C_{22}$  and  $J_2$  gravitational accelerations have the same order of magnitude, which is one order higher than that of the tesseral  $C_{31}$ ,  $C_{32}$ , and  $C_{33}$  [10]. For the lunar missions with an orbit higher than 1500 km, the third-body perturbation for circum-lunar orbits is the largest. Evolution of Moon perturbations with respect to altitude is shown in Figure 1.4, taken from [11].

These effects are modeled considering the 3rd-degree terms of harmonics, the rotation of the Moon, and the effect of the Earth, as detailed in [12]. From this model, it is shown that there exist some "frozen" low orbits, for which variations of inclination, eccentricity, and argument of pericentre are small and do not lead to chaotic/collision orbits. This means that the *s/c* would require minimal control and station keeping (SK) effort.

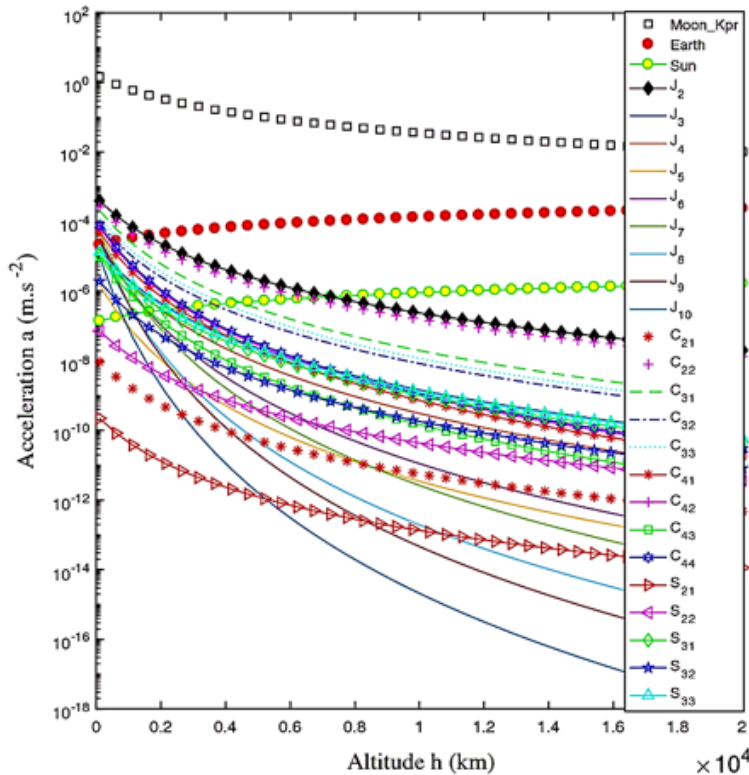


**Figure 1.4:** Perturbation accelerations for a lunar orbiter



#### 1.4.4 Lunar magnetic Field

The magnetic field of the Moon is essentially negligible. However, an extremely weak magnetic field of  $3\text{-}300 \times 10^{-5}$  Gauss has been measured. Additionally, an external field due to the solar wind of  $5\text{-}10 \times 10^{-5}$  is present when the Moon transits in the Earth's geomagnetic tail during 4 days per orbit [13]. Hence, it is not possible to use the magneto-torques and magnetometers for the Attitude Determination and Control System (ADCS).

#### 1.4.5 Lunar Wake

Another particularity of the Moon is the so-called "lunar wake". When the solar wind hits the surface of the Moon it charges the sunlight side of the Moon, while the hidden side has no charges from plasma, as depicted in Figure 1.5. This can lead to important discharges of the *s/c* when entering those "charge-less" zones, as well as lead to the creation of some small magnetic perturbations. This phenomenon is still not well understood, and science missions are still ongoing to study it [14]. Literature research, however, might suggest that an unshielded system might reach a few hundred V of positive voltage [15], based on the data collected by THEMIS missions.

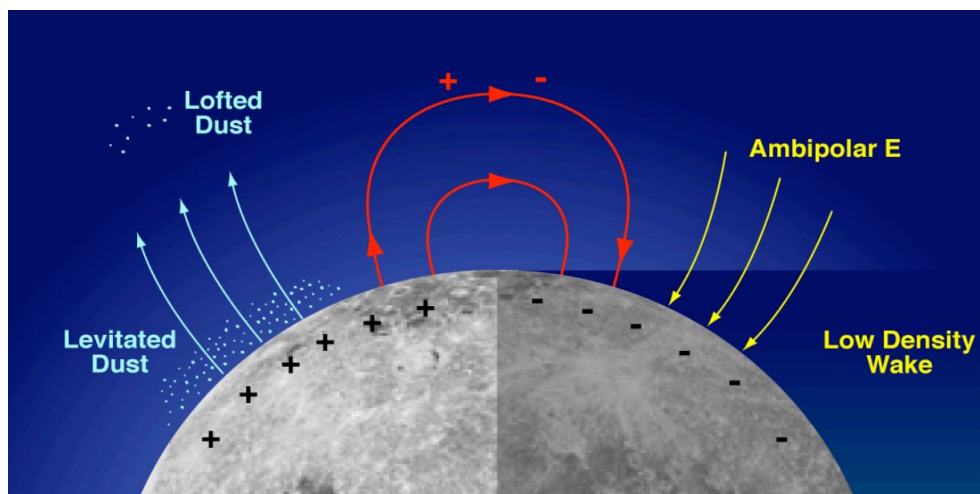


Figure 1.5: Lunar wake phenomena

#### 1.4.6 Environmental effect on orbit

Four main orbital perturbations can affect the *s/c* orbit. For LUMINOUS mission, the third body (Earth), fourth body (Sun), and Solar Radiation Pressure (SRP) are the most important perturbations on the *s/c*. Since the Moon does not have an atmosphere, the drag will be zero. In addition to this, the Moon's oblateness perturbation is considerable only when the orbit is not too high. These effects will be considered in the mission analysis section in order to find the behavior of the orbit around the Moon.

### 1.5 Modeling of environmental effects

The models employed for the evaluation of environmental effects on the mission are embedded in one or more requirements from the European Cooperation for Space Standardization (ECSS) standard document [9]. The following Table 1.3 links each effect/perturbation to a model/regression to fulfill the reported requirements. It is not the aim of this section to explain how each model is built; this information is exhaustively discussed in [9]. For the sake of the environmental modeling for the mission, please just keep in mind most parameters are connected since they are input for other parameters sizing. The mutual interconnection among them is traced in this section so that the workflow is clear and, possibly, replicable. The modeling of the environment has focused on the main threats for the mission, namely solar particles and GCR.



### 1.5.1 Sun and Geomagnetic activity indexes

The first parameters to be evaluated are the Sun and geomagnetic activity indexes. As the mission seeks to carry out scientific observations during a long time span including both solar minimum and maximum, tracing of the Sun-linked perturbations on the mission playground is of paramount importance. In the framework of ECSS standard [9], the peak of solar activity is defined as an interval spanning from  $T_{mss} - 2.5y$  to  $T_{mss} + 4.5y$ , being  $T_{mss}$  the moment of maximum sunspots number. In Table 1.2 best, worst, and 81-days-averaged (three solar rotations) scenarios for the principal solar indexes are reported.

Parameter	Minimum		Maximum	
	Long term	Short term	Long term	Short term
F 10.7	65	65	250	300
S 10.7	60	60	220	235
M 10.7	60	60	220	240
$A_p$	0	0	45	240

(a) Sun and geomagnetic activity indexes: best and worst case scenario

Parameter	Minimum	Maximum
F 81	61	227
S 81	58	213
M 81	63	214

(b) Sun and geomagnetic activity indexes: 81-days-averaged best and worst case scenario

**Table 1.2:** Sun and geomagnetic activity indexes for mission design

### 1.5.2 Plasma environment

Ionosphere is not modeled, since the launcher is expected to release the s/c above its limit.

The plasmasphere originates from the ionosphere; it is composed of cold plasma trapped by Earth's magnetosphere. Typically, particles in this layer do not exceed 0.5 eV; they tend to prevent charging of the s/c, damping out voltage mismatches [9].

GCPM is the model to be used for the assessment of plasma density, along with the information coming from IRI. Apart from position and time, GCPM requires the  $K_p$  parameter as input. To shape the worst case scenario,  $K_p = 9$  shall be applied, since this is the case in which the plasmasphere has minimum volume, thus damping of ElectroStatic Discharge (ESD) is severely reduced. Results spanning from one to 8  $R_E$  for nearly-equatorial orbits are shown in Figure 1.6. Please note the difference in span for the plasmasphere for turbulent Sun ( $K_p = 9$ ) with respect to the one for quiet Sun.

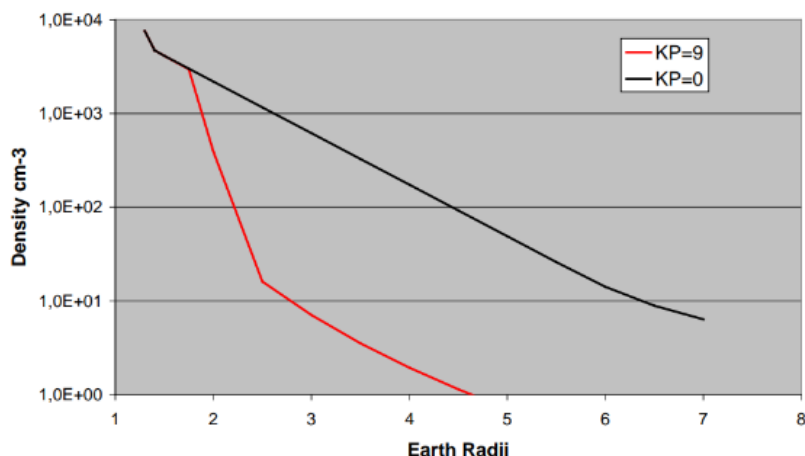


**Figure 1.6:** Plasmasphere density vs distance from the surface of Earth for nearly-equatorial orbits



Parameter	Model	Requirement (from ECSS-E-ST-10-04C)
Earth gravity	EIGEN-GL04C	ECSS-E-ST-10-04_0760004
Internal magnetic field	IGRF13 Jensen Cain 1960 GSFC 12/66 1970	ECSS-E-ST-10-04_0760008, ECSS-E-ST-10-04_0760053
External magnetic field	Tsyganenko 1996	ECSS-E-ST-10-04_0760011
Solar constant	Table 6-2	ECSS-E-ST-10-04_0760014
Solar activity	Table A-1 (Solar cycle 23) Table 6-3	ECSS-E-ST-10-04_0760017, ECSS-E-ST-10-04_0760018 ECSS-E-ST-10-04_0760021, ECSS-E-ST-10-04_0760023 ECSS-E-ST-10-04_0760029, ECSS-E-ST-10-04_0760030 ECSS-E-ST-10-04_0760031
$a_p$ evolution	Table 6-4	ECSS-E-ST-10-04_0760019, ECSS-E-ST-10-04_0760020
Atmosphere figures	NRLMSISE-00	ECSS-E-ST-10-04_0760025
Earth wind	HWM07	ECSS-E-ST-10-04_0760033
Ionosphere	IRI-2016	ECSS-E-ST-10-04_0760038
Auroral charging	Equation 8-1 Equation 8-2	ECSS-E-ST-10-04_0760042, ECSS-E-ST-10-04_0760043 ECSS-E-ST-10-04_0760133
Plasmasphere	GCPM	ECSS-E-ST-10-04_0760044, ECSS-E-ST-10-04_0760045
Outer magnetosphere	Table 8-1	ECSS-E-ST-10-04_0760046
Solar wind	Table 8-2	ECSS-E-ST-10-04_0760047, ECSS-E-ST-10-04_0760048
Magnetosheath, magnetotail	Annex H	
Plasma from spacecraft surface interactions	Annex H	
Trapped particle fluxes	AE-8 (electrons) AP-8 (protons) FLUMIC-V3 (worst case electrons)	ECSS-E-ST-10-04_0760052, ECSS-E-ST-10-04_0760054 ECSS-E-ST-10-04_0760055, ECSS-E-ST-10-04_0760067
South Atlantic Anomaly	TREND-2	ECSS-E-ST-10-04_0760056
Particles fluxes near GEO	IGE-2006 (electrons) AP-8 (protons)	ECSS-E-ST-10-04_0760057, ECSS-E-ST-10-04_0760058 ECSS-E-ST-10-04_0760059
Solar particles fluence	ESP model	ECSS-E-ST-10-04_0760069, ECSS-E-ST-10-04_0760070
Geomagnetic shielding/Solar particles peak flux	CREME 96 Table B-10 Table B-11 TableB-12 None (worst case scenario for shielding)	ECSS-E-ST-10-04_0760138, ECSS-E-ST-10-04_0760074
Galactic cosmic rays	ISO 15390:2004	ECSS-E-ST-10-04_0760075
Atmpospheric albedo neutron fluxes	Annex I7	ECSS-E-ST-10-04_0760142
Space debris	MASTER-8	ECSS-E-ST-10-04_0760087, ECSS-E-ST-10-04_0760088 ECSS-E-ST-10-04_0760089, ECSS-E-ST-10-04_0760146
Meteoroids	Grün model Table J-5 Table C-1 Table C-2 MEMR-2	ECSS-E-ST-10-04_0760091, ECSS-E-ST-10-04_0760092 ECSS-E-ST-10-04_0760094, ECSS-E-ST-10-04_0760151 ECSS-E-ST-10-04_0760153, ECSS-E-ST-10-04_0760156 ECSS-E-ST-10-04_0760102, ECSS-E-ST-10-04_0760103 ECSS-E-ST-10-04_0760104

**Table 1.3:** Effects, their model and reference requirements from [9]

The outer magnetosphere is a dynamic region for which modeling is a rather complex task. Because of this, the assessment of worst case scenario is typically more interesting than a proper time and Sun-activity dependent model. ECSS document



[9] requires the use of a 3-Maxwellians population fit based on a sunlight charging event that occurred to the Scatha spacecraft, reported in Table 1.4.

	<b>Electron density</b> ( $cm^{-3}$ )	<b>Electron temperature</b> (KeV)	<b>Ion density</b> ( $cm^{-3}$ )	<b>Ion temperature</b> (KeV)
<b>Populaion 1</b>	0,2	0,1	1	3
<b>Population 2</b>	2	10	1	20
<b>Population 3</b>	0,01	50	0,05	40

**Table 1.4:** Worst case scenario for the modeling of the outer magnetosphere

### 1.5.3 Solar wind

Solar wind at 1 AU is described in Table 1.5. For any application at a distance different from the aforementioned, inverse quadratic scaling shall be applied [9].

<b>Parameter</b>	<b>Mean</b>	<b>5-95% Range</b>
Speed ( $Kms^{-1}$ )	468	320 - 710
Density ( $cm^{-3}$ )	8,7	3,2 - 20
$T_p$ (K)	$1,2 \times 10^5$	$1 \times 10^4 - 3 \times 10^5$
$T_e$ (K)	$1,0 \times 10^5$	$9 \times 10^4 - 2 \times 10^5$
$N_{alpha}/N_{proton}$	0,047	0,017 - 0,078

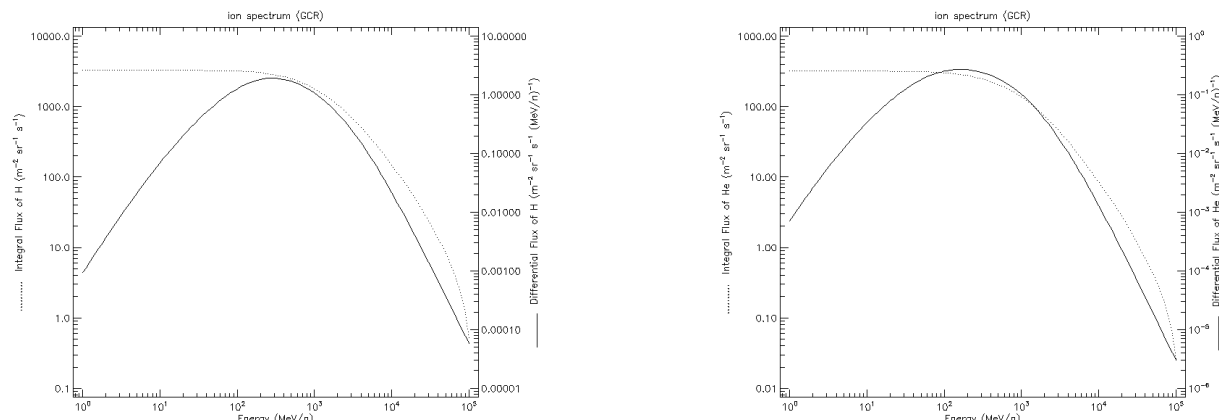
**Table 1.5:** Solar wind parameters (mean and 2- $\sigma$ )

### 1.5.4 Solar particles

Solar particle fluence requires the ESP model (empirical, data from solar cycles 20, 21, 22) to be applied, while solar particle peak fluxes are determined with CREME96. GCR are modelled using ISO 15390:2004. Geomagnetic shielding is neglected since most of the mission will take place outside the Earth's magnetosphere. The worst case scenario is assumed to be characterized by a flux of  $3e10 cm^{-2}$  for protons with energy exceeding 30 MeV [9].

Results are obtained by simulating with CREME96 a s/c orbiting the Earth at a mean distance equal to the mean Earth-Moon distance, during solar minimum and maximum of solar cycle 23, for all elements from hydrogen (1) to uranium (92). For the sake of brevity, only figures for hydrogen and alfa particles (He nuclei) are reported in Appendix A.

GCR worst case scenario is assessed during the period of solar minima, since the shielding effect of the solar window is drastically attenuated. Again, simulations have been run for elements up to U, but only results for H and He nuclei are shown (Figure 1.7).



**(a) H-flux from GCR**

**(b) He-flux from GCR**

**Figure 1.7:** GCR worst case scenario

# Chapter 2 Mission Analysis

The high-level requirements of the mission are to **exploit the Moon**<sup>1</sup> as Sun occulter to image the solar corona and to **maximize the observation time**<sup>2</sup>, considering also the possibility of **multi-platform solutions**<sup>3</sup>.

To exploit the Moon as Sun occulter means that the observations have to occur inside the lunar eclipse cone, then the maximization of the observation time was translated into the maximization of the time spent by the spacecraft inside the eclipse cone.

Among the solutions involving an orbiting payload (for the moment, let's avoid considering solutions concerning ground observations), it is hard - if not impossible - to imagine an orbital trajectory positioning the spacecraft constantly in eclipse; nevertheless, depending on the solution, extending the number of platforms could theoretically provide continuous observations.

The possibility of **continuous solar corona imaging** was then set as an essential feature of the final solution and it was used to drive the highest-level trade-off.

## 2.1 Solar Corona Observation

### 2.1.1 Scientific input

Together with the high-level mission objectives and requirements, the team also received some indications regarding the **scientifically significant features**<sup>4</sup> that solar corona observations should exhibit according to the experts.

- *Percentage of corona in the field of view*: it is better to have the whole disc in the image, but even the partial disc is acceptable whenever the image is not overlightened by the unshielded part of the Sun.
- *Distance to observe*: a minimum of 3 solar radii up to 30 is of interest.
- *Observation time*: both continuous and discrete observation windows are of interest; long continuous observations are interesting for space weather, but also short intermittent observations are scientifically valuable.

This info was the starting point in the definition of some sort of observation quality parameters (see 2.1.3) useful to evaluate the goodness of an eclipse passage.

### 2.1.2 Observation Model

To evaluate the goodness of an eclipse passage, it is necessary to reconstruct what the **s/c** would "see" during it, i.e. which portion of the solar corona would be possible to image depending on the Field of View (**FOV**) of the payload and the occultation of the Moon circle.

The image reconstruction was modeled assuming the payload constantly pointed at the Sun during the whole eclipse passage, which would guarantee to have always the corona at the center of the picture.

<sup>1</sup> Req. [F-0001]: The system shall obtain mission data by exploiting the Moon as solar occulter

<sup>2</sup> Req. [M-0004]: The mission shall be designed to maximize the observation period.

<sup>3</sup> Req. [F-MA-0002]: The system should have at least TBD observation platforms to increase observation time.

<sup>4</sup> The indications of the experts were translated into the following Mission Requirement:

**Req. [M-MA-0006]**: The operational orbit design shall guarantee observation of the Inner Corona (1-5 Sun Radii) of at least 30 minutes OR observation of the Outer Corona (5-35 Sun Radii) of 360°, during a single observation window

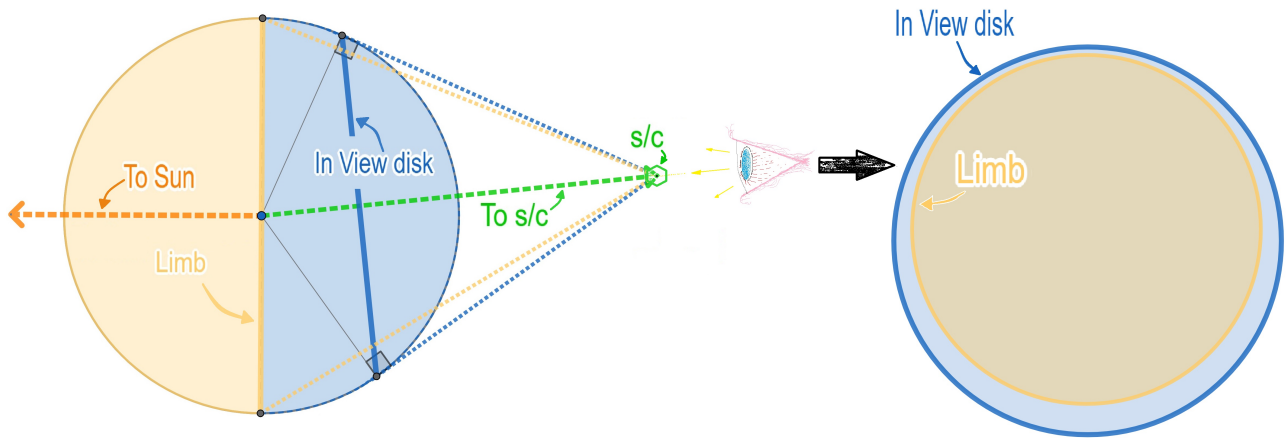


**Figure 2.1:** Sketch of the reconstruction of the Moon disk image

Fig. 2.1 briefly depicts the geometrical framework considered to generate the Moon image as seen from the perspective of the *s/c*: the Moon circle visible from the position of the *s/c* is the locus of points obtained as the intersections of all the straight lines passing from the *s/c* and tangent to the Moon sphere.

The same considerations apply to the generation of the Sun circle image; moreover, to provide some sort of observational coordinates, the Carrington model (1863) was used to approximately identify the direction of the solar North Pole (see [16], Appendix A).

### 2.1.3 Observation Quality parameters

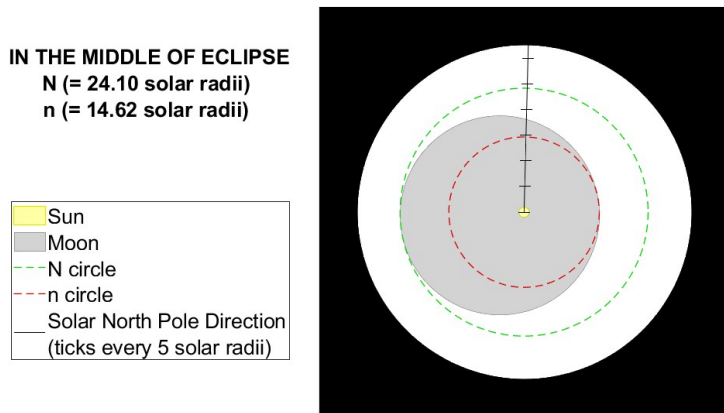


**Figure 2.2:** Example of image reconstruction during an eclipse passage - the Sun disc is visible just for clearness.

Given the scientific input presented in subsection 2.1.1, a couple of parameters to evaluate the scientific value of the images potentially provided by an eclipse passage were defined:

- ***N***: given the Sun center and the Moon circle as seen from the spacecraft perspective, drawing the circumference centered at the Sun center and *externally* tangent to the Moon circle, *N* is then defined as the radius of the obtained circumference expressed in apparent<sup>5</sup> Sun radii; it measures which coronal sectors are visible as a whole, i.e. at  $360^\circ$ .
- ***n***: given the Sun center and the Moon circle as seen from the spacecraft perspective, drawing the circumference centered at the Sun center and *internally* tangent to the Moon circle, *n* is then defined as the radius of the obtained circumference expressed in *apparent* Sun radii; it measures how close to the Sun surface the corona can be imaged, even if at that distance the correspondent coronal sector will be partially occulted by the Moon.

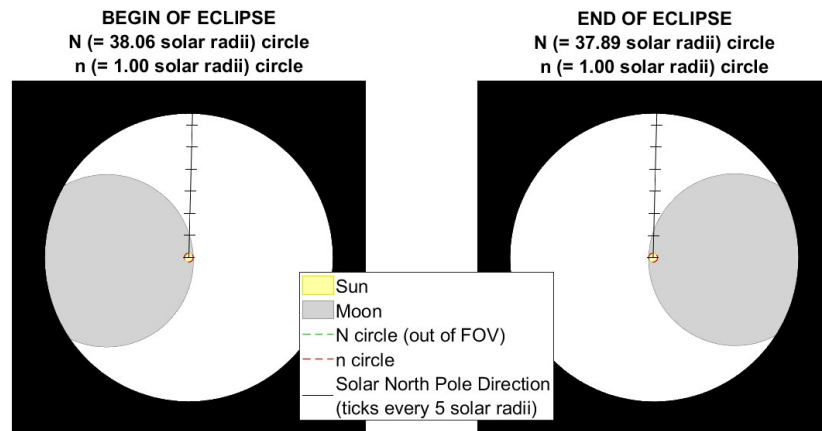


**Figure 2.3:** Example of image reconstruction during eclipse passage - the Sun disc is visible just for clearness.

These parameters are defined at each instant of an eclipse passage; to derive a couple of unique values associative to a whole eclipse passage,  $N$  and  $n$  were used to define:

- $N_{MIN}$ : given an eclipse passage, it is the minimum  $N$  registered; it indicates which is the best observation of the corona disk as a whole offered by a passage, thus it was selected as the estimator of the observation quality of a passage at  $360^\circ$  level, derived from the scientific input concerning the *Percentage of corona in the field of view* - which stated the preference to have the whole disc in the image.
- $T_{n_{MAX}}$ : given an eclipse passage, it is the amount of time during which  $n$  is lower than  $n_{max} = 5R_{Sun}$ ; it was selected as the estimator of the observation quality of a passage concerning the feasibility of imaging the most inner regions of the corona, derived from the scientific input related to the *Distance to observe* - which stated the interest in observing the corona starting from 3 solar radii.

It consists of a time measure since the definition of  $n$  implies that every passage will register twice the minimum possible value of 1 apparent  $R_{Sun}$  (so that the corona will be visible up to the Sun photosphere, even if not at  $360^\circ$ ), but it always occurs at the beginning and the end of an eclipse passage, i.e. when from the perspective of the spacecraft, the Sun and Moon discs are tangent (see Fig. 2.3); however, depending on the orbit, the time spent by the Sun near the border of the Moon, can be so short - in the order of a bunch of minutes - that the chances that the payload captures the inner parts of the corona decrease significantly.

## 2.2 High-level alternatives

This section aims to provide the broadest overview of the investigated mission scenarios. In particular, the team identified some high-level solutions:

- Earth's solutions
- Earth-Moon system solutions
- Moon's solutions

In the next paragraphs, the alternative selection will be presented:

### 2.2.1 Earth solution

Starting from the Earth's environment, an **EARTH ORBIT** solution could guarantee the design of an easy communication window while performing observations. However, the eclipse would occur rarely because for this to happen, a conjunction

<sup>5</sup> apparent: in the reference frame of the camera



between Sun, Moon, and Earth is needed. Furthermore, the presence of the atmosphere increases the background luminosity, degrading the quality of the final image. More importantly, a solution like this could not guarantee a continuous observation of the Solar Corona, and for this reason, it was **DISCARDED**.

### 2.2.2 Earth-Moon system solutions

The team considered also the alternatives coming from the Earth-Moon system which falls into two main alternatives: Distant Retrograde Orbit (**DRO**) and orbits around the Lagrangian points  $L_4/L_5$ .

#### Orbits around Lagrangian Points $L_4/L_5$

The  $L_4/L_5$  Lagrangian points correspond to ideal locations to observe the Solar Corona given their stability and their very high distance from the Moon, which occultates a very small portion of the solar corona if observed from there (Fig. 2.4).

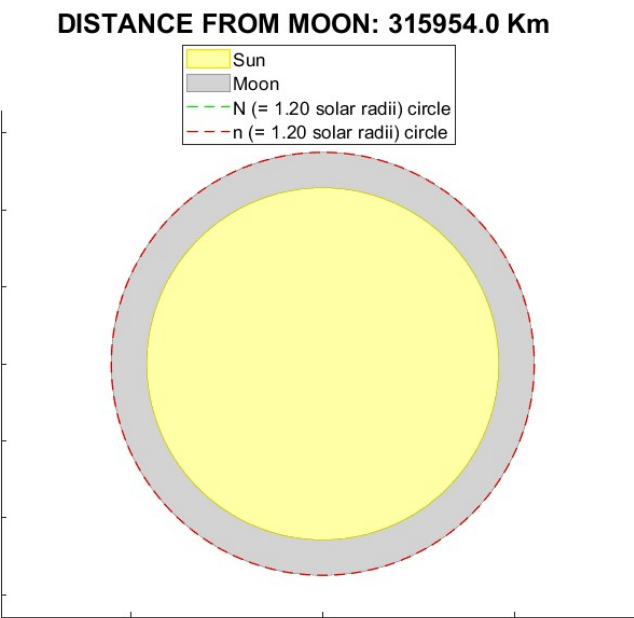
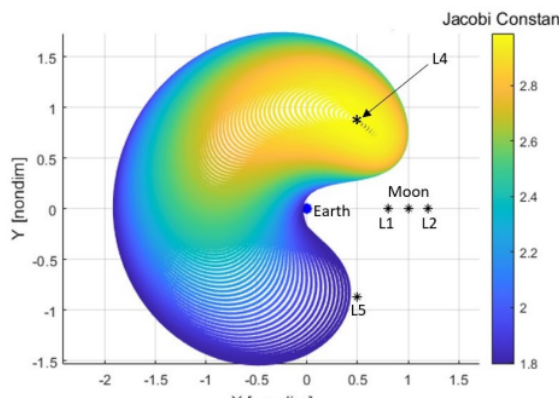
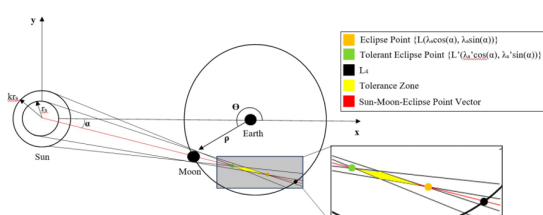


**Figure 2.4:** Example of image reconstruction during eclipse passage from orbits around  $L_4/L_5$  Lagrangian points - the Sun disc is visible just for clearness.

It is possible to reach  $L_4/L_5$  efficiently. Figure 2.5a [17] shows the evolution and shape of the Short Periodic Orbit (SPO) family around  $L_4/L_5$ . The SPO family is plotted within the Earth-Moon barycenter rotating frame, together with the corresponding Jacobi Constant value of each member.



(a) Short Periodic Orbits (SPO) family about  $L_4$



(b) Tolerance zone within the Moon's Umbra to observe the Solar corona



To find the optimal SPO with the longest observational time of the Solar Corona, the entire family of  $L_4/L_5$  orbits are run 38 sidereal months, because it provides enough time to see the true behavior of each SPO [17].

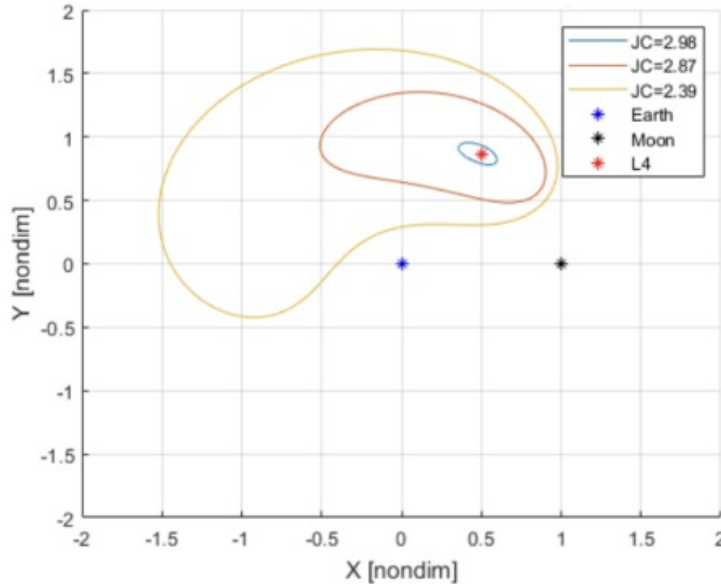


**Figure 2.6:** Three selected SPOs

In the research paper just cited, three SPOs have been selected. As seen in Figure 2.6 selected SPOs, the orbits greatly vary in size and shape, but each of them provides a unique advantage.

Table 2.1 shows the advantages and disadvantages of each SPOs selected, to note is that the observation time is provided over the 38 sidereal months simulation.

Orbits family	Advantages	Disadvantages	Observation Time
$SPO_1$	$L_4$ proximity and consistent observation time	Lack of observation time and low stability	6 hours
$SPO_2$	Stable orbit and high observation time	Far from $L_4$	24 hours
$SPO_3$	Stable orbit and high observation time	Far from $L_4$ and high orbital velocity	29 hours

**Table 2.1:** SPO advantages and disadvantages

Orbits family	Observation time [h/month]
$SPO_1$	0.17
$SPO_2$	0.69
$SPO_3$	0.84

**Table 2.2:** Hours of observation time in terrestrial months for each family

In conclusion Table 2.2 shows the observation time for each SPO family converted in hours per terrestrial month. From this data, an average value of just 0.57 [h/month] is obtained. Furthermore, it is to be noted that even adopting a multi-platform solution, the total observation time per month could not be longer than the time spent by the eclipse cone in the proximity of the stable Lagrangian point, meaning that this kind of solution could not guarantee **continuous solar corona imaging**. For this reason, this solution was **DISCARDED**.

## DRO Solution

DRO is a family of stable orbits in the Circular Restricted Three Bodies Problem (CRTBP). Despite their great stability properties, they lie on the Earth-Moon plane, rarely intersecting the eclipse cone. This means that, even with a multi-platform solution, is not possible to guarantee **continuous solar corona imaging**. For this reason, this solution was **DISCARDED**.



### 2.2.3 Moon solutions

Finally, the team considered the solutions closest to the Moon.

A **MOON GROUND** solution was not discarded a priori: a payload could be positioned on a rover following the lunar limb, potentially continuously imaging (half) of the solar corona, at the same time offering a very close look to the interaction between the lunar dust and the Sun, which is also one of the secondary objectives of the mission. Despite these good points, on one side the lunar dust would degrade the quality of the observations, while on the other side, the team **DISCARDED** this option believing it would be highly challenging to design a sufficiently reliable motion system, capable of avoiding building an enormous number of rovers to provide data for 6 years.

The last and **SELECTED** group of alternatives are the **MOON ORBITS**; in this case, continuous observations could be guaranteed by the adoption of a multi-platform solution: the ratio  $T_{\text{orbit}}/T_{\text{eclipse}}$  - which indicates the minimum number of spacecraft to place in a single orbit to always have one of them in eclipse - is in the order of some dozens, depending on the semi-major axis.

## 2.3 Moon Orbits

Once the family of orbits around the Moon was chosen as the baseline for the design of the final solution, many considerations further restricted the realm of considered possibilities.

The first point was to define the range of **semi-major axis** to explore. A **lower bound** was fixed at **9 Moon radii**: as you can see in Fig. 2.7, at best, from that position  $N_{\text{MIN}}$  would be equal to  $\sim 31$  Moon Radii, which is already over the upper bound of interest according to the experts, which is equal to 30 (see 2.1.1)

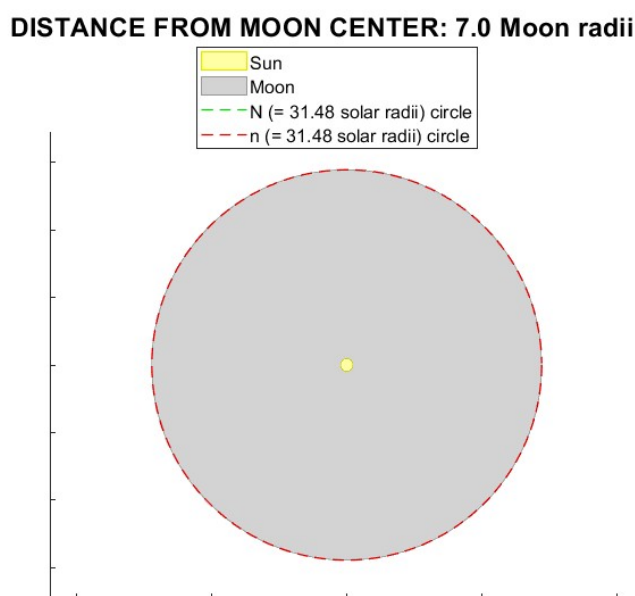


**Figure 2.7:** Example of image reconstruction during eclipse passage from orbits at 9 Moon radii.

An **upper bound** was fixed at **15 Moon radii**, as bigger orbits would on average leave the Moon very fast, as can be appreciated in Fig. 2.8

For simplicity, regarding the **eccentricity**, the analysis was restricted to the case of **circular** orbits: the simplicity relies on the fact that a circular orbit intersects the eclipse cone either if its inclination with respect to the eclipse cone axis - which is practically lying on the ecliptic plane - is lower than a certain value dependent on its radius (see Fig. 2.11), OR its RAAN is sufficiently close to the Right Ascension of the eclipse cone axis such that, regardless the inclination, the orbit intersect in any case the cone see Fig. 2.9).

### 2.3.1 Moon orbit - Final choice

Although the Moon is not perfectly aligned with the ecliptic plane, the eclipse cone axis formed can be assumed to move on it. For this reason, having a final orbit that remains as much as possible inside the ecliptic plane would be for sure a

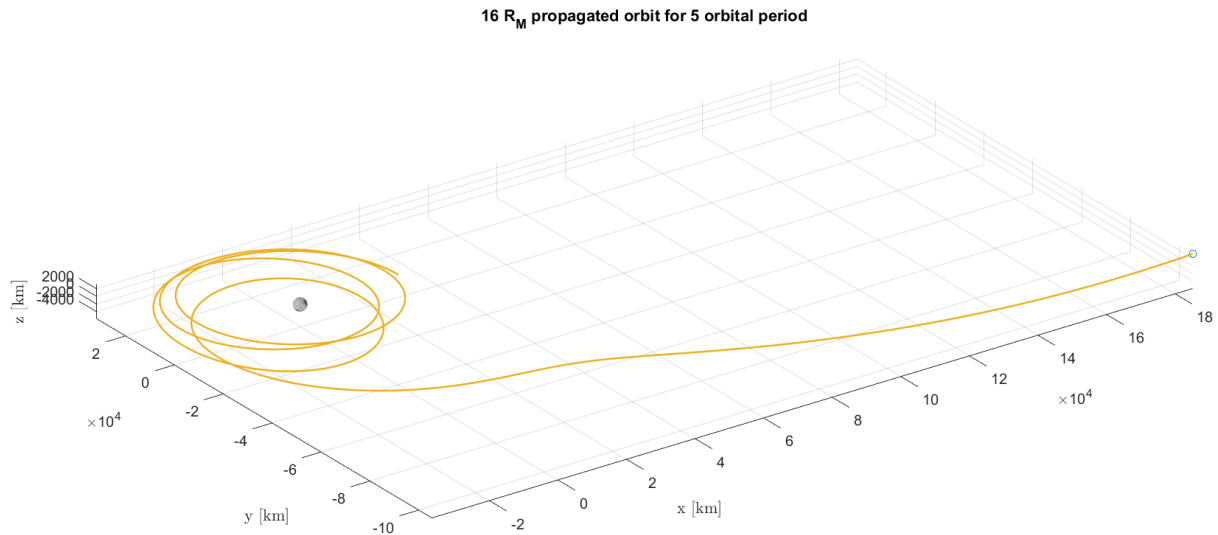


**Figure 2.8:** Initially 16 Moon radii orbit, which leaves the Moon in just 5 revolutions.

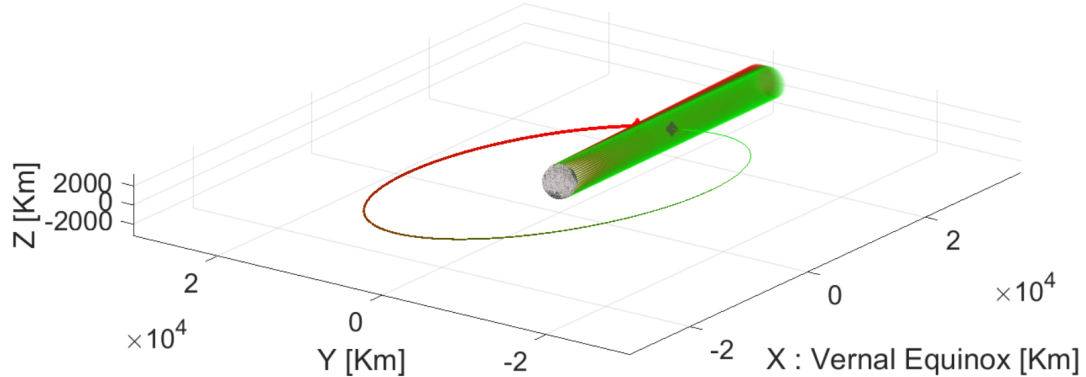


**Figure 2.9:** Example of a circular orbit passing through the eclipse cone. Its inclination alone would not be sufficient to make it intersect the Moon's shadow; its RAAN - aligned with the direction of the Sun - guarantees the eclipse passage.

good candidate for the final solution. This justify the first kind of strategy investigated.

#### Station-keeping strategy - Control of the inclination

A strategy to have valuable observations in every orbit would be to control the inclination such that the orbit remains inside the Moon's shadow.

In [Figure 2.10](#), it is shown the evolution of the inclination of different orbits, varying the altitude. It is visible how the inclination behaves periodically and, starting from zero degrees, grows reaching more than 10 degrees over time,

Now, it's crucial to understand what are the boundaries of the inclination that permit the orbit to remain within the eclipse cone.

[Figure 2.11](#) shows the 2D sketch of the eclipse cone behind the moon. To be noted are the red and the blue line, which represents a 7 and 15-moon radii orbit, and the fact that as the radius of the orbit increases, the inclination of the orbit needed to remain inside the cone decreases, being  $\alpha$  and  $\beta$  the maximum acceptable inclinations.

Considering [Figure 2.10](#), it's visible how the evolution of the inclination of the different orbits exceeds the boundary shown in [Figure 2.11](#). The station-keeping strategy to control the inclination consists of, basically, change-plane maneuvers aiming to reset the value at zero degrees when the inclination reaches the critical angle that leads the orbit to exit the

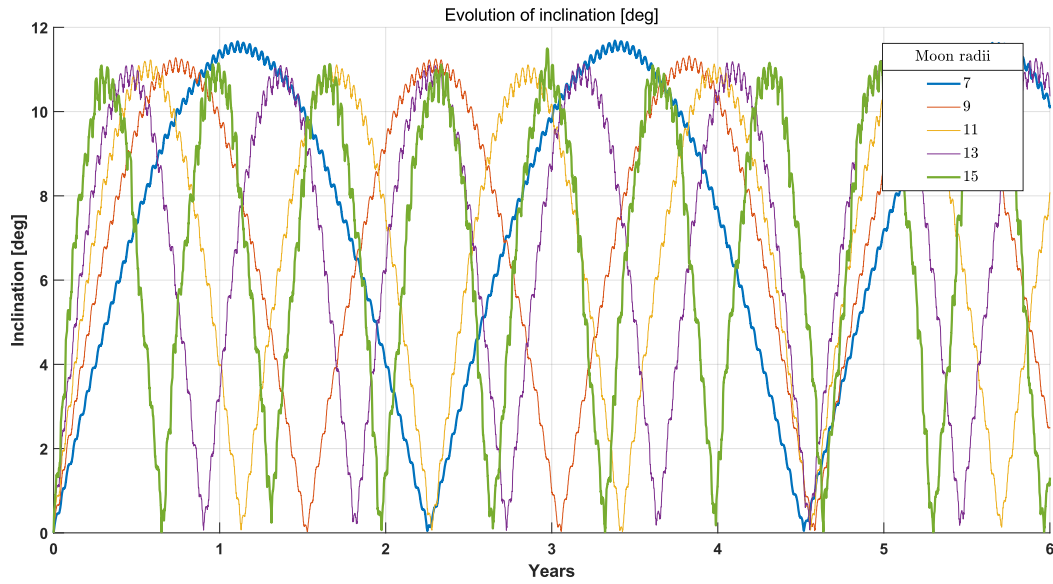


**Figure 2.10:** Evolution of the inclination of different Moon orbits

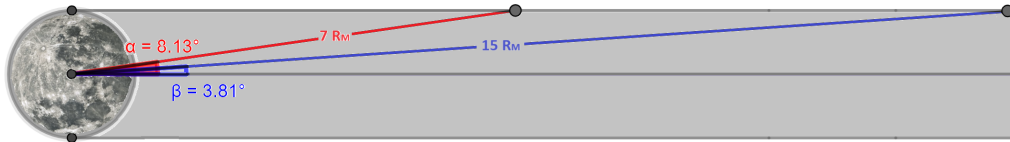


**Figure 2.11:** Front view of the 2D sketch of the eclipse cone

eclipse cone.

The cost of a change plane maneuver can be retrieved as:

$$\Delta V = 2 \cdot v_\theta \cdot \frac{\delta}{2} \quad (2.1)$$

where  $v_\theta$  is the velocity of the circular orbit and  $\delta$  is the gap in inclination that the maneuver has to fulfill.

$r_{orbit}$ [R <sub>M</sub> ]	Critical angle [deg]	$\Delta V$ [km/s]	$N_{MAN}$	$\Delta V_{TOT}$ [km/s]
7	8.13	0.0898	11	0.9877
11	5.19	0.0458	34	1.5578
13	4.40	0.0357	52	1.8587
15	3.82	0.0289	67	1.9361

**Table 2.3:** SK strategy controlling the inclination - costs

Table 2.3 summarize the station-keeping strategy related to the control of the inclination, it shows how increasing the radius of the orbit, the critical angle (the one that leads the orbit to exit the eclipse cone) decreases. Furthermore, using Equation 2.1, the cost of the single maneuvers can be easily retrieved, as well as the total one which is considered a 6-year mission. As the critical angle decreases, a greater effort to maintain the orbit inside the eclipse cone is required, thus the number of maneuvers and the total cost increase.

These high values of the station-keeping costs led the team to consider another strategy, which is to control the Right Ascension of the ascending node (**RAAN**) of the orbit to maintain it aligned with the position of the cone. In this case, the inclination of the orbit would not be of interest because in any case, the orbit would fall within the eclipse.

### Station-keeping strategy - Control the RAAN

As said, an alternative to the previous solution is to control the RAAN to be aligned with the position of the eclipse cone, instead of the inclination. This strategy would allow to disinterest of the inclination behavior, permitting the orbit to pass



through the eclipse cone in any case.

At this point, the goal is to find a way to follow the position of the eclipse cone, lowering the costs concerning the previous strategy. By studying the evolution of the orbital parameters of the previously cited circular orbits, the team found that the RAAN exhibits a particular behavior. In particular, it rotates in the same direction as the sun's apparent movement from the moon for **retrograde orbits**. This behavior makes the orbit a **sun-synchronous** orbit.

Within this strategy, two kinds of approach can be performed:

1. Maintain the perfect alignment between the RAAN of the orbit and the Right Ascension of the axis of the eclipse cone
2. Allow a little misalignment to observe better the inner solar corona

In particular, if the spacecraft is injected in an orbit that has the **RAAN** aligned with the eclipse cone on a specific date, the simulation's results show that this alignment remains almost always close enough to allow valuable observations of the solar corona.

In [Figure 2.12](#) it is shown the evolution of the RAAN of some Moon's orbit with respect to the right ascension of the eclipse cone. It's visible how the **11 Moon radii orbit** is the one that remains more aligned during the 6-year mission, and also in case of **SK** failure, would allow valuable observations; for these reasons, the **11 Moon radii** orbit has been chosen as operational orbit. In this case, the station-keeping strategy consists of maneuvers that aim to reduce this gap. To be noted is that the behavior showed in [Figure 2.12](#) is obtained from an initial inclination of the orbit of 170 degrees, which results in optimizing the closeness to the **RAAN** of the eclipse cone.

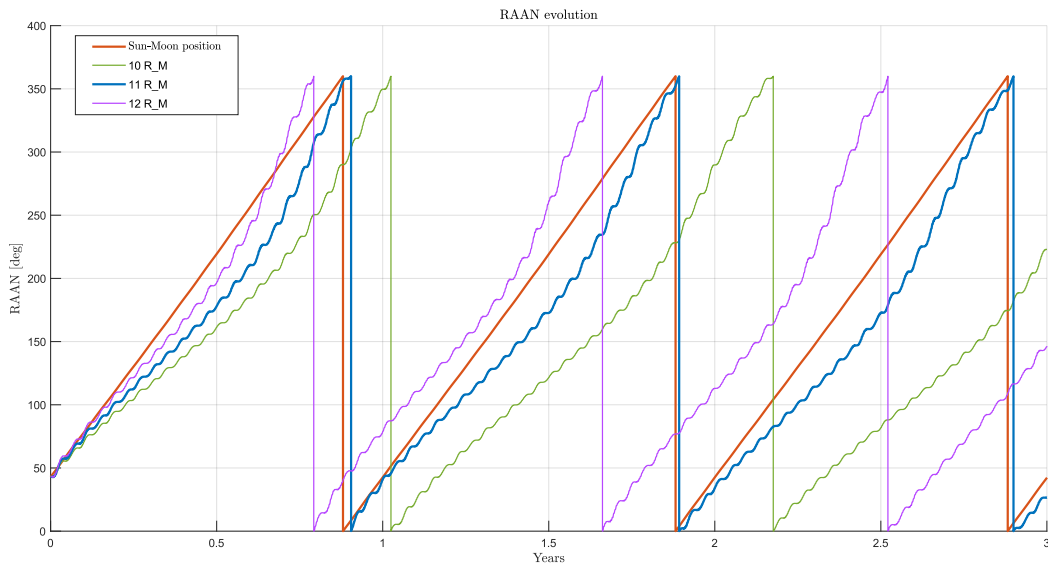


**Figure 2.12:** RAAN's evolution of different moon's orbit vs Sun-Moon movement

With this approach, the s/c would intersect the eclipse cone passing almost through its axis, which corresponds to having a maximum duration of the eclipse and the biggest portion of Corona observable at  $360^\circ$ , regardless of the inclination. Moreover, the SK cost is expected to be much lower than in the previous strategy, due to the natural evolution of the RAAN.

[Figure 2.13](#) shows the orbital parameters' evolution of an **11 Moon radii orbit**, it's visible how the orbit remains stable over a 6-year lifetime,

**Quality of the observation** As previously said, the solar scientists showed their interest in observing the Solar Corona in the range  $3-30 R_{Sun}$ , preferably having the whole disk in the image ( $360^\circ$  corona observation or full-Corona observation). Simulations' results showed how, for the **11 Moon radii** orbit, the full-Corona observation is possible only from  $20 R_{Sun}$  upwards, as seen from [Figure 2.14](#) (due to the closeness to the moon). It is evident that this sort of orbit will eventually offer only partially occulted observations of the inner regions of the Corona, where these observations can occur only at the beginning and at the end of the eclipse passage and they last only some minutes.

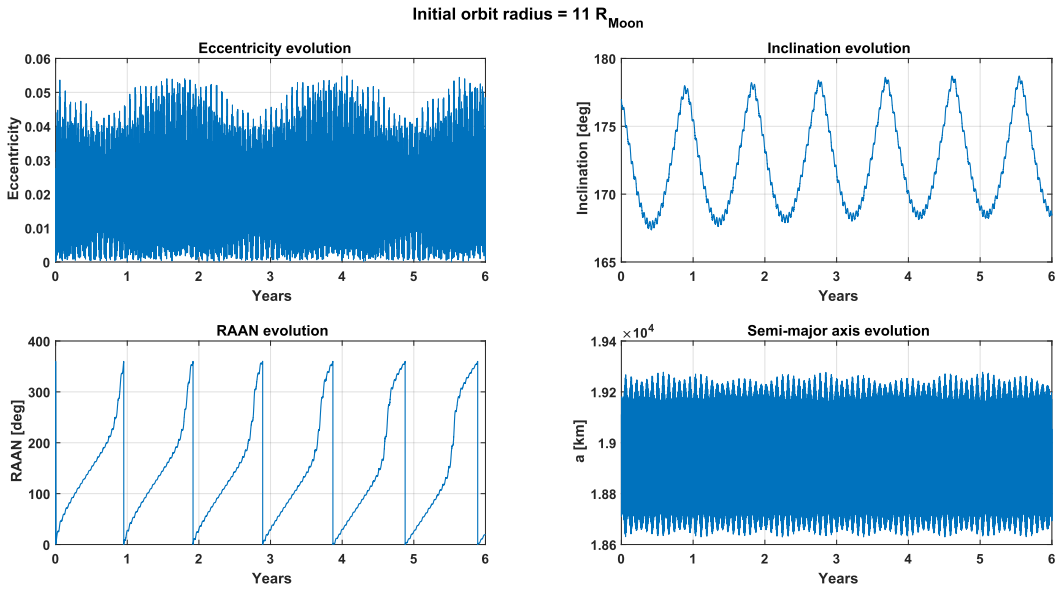


**Figure 2.13:** Parameters' evolution for retrograde 11 Moon radius orbit

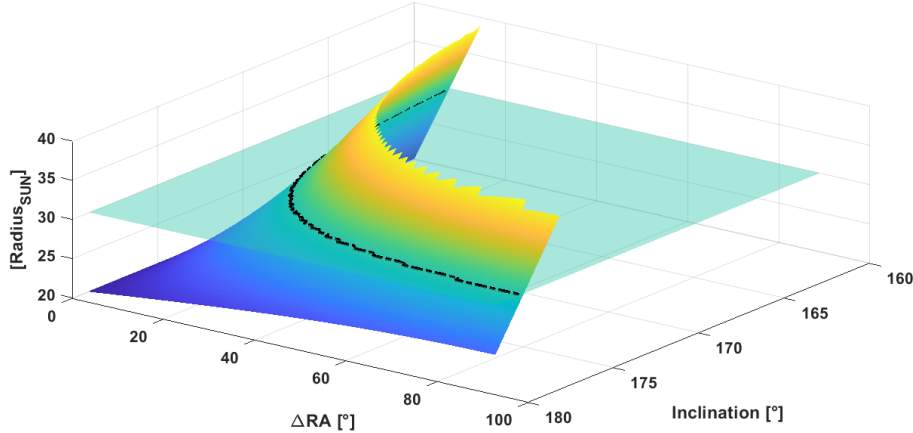


**Figure 2.14:** 360° view of the solar corona as a function of orbital parameters for an  $11R_{\text{MOON}}$  orbit

The inner regions of the Corona become observable for much longer durations when the spacecraft trajectory intersects the eclipse cone near its border. This is the result of a unique combination of both the inclination and the difference between the RAAN of the orbit and the Right Ascension of the cone. Therefore, both the inclination and the difference in Right Ascension are investigated to design the SK strategy

In Figure 2.14 is shown how the inclination and the difference between the RAAN of the orbit and the right ascension one of the eclipse cone affect the full-Corona observations. Each point of the plotted surface corresponds to an eclipse passage of an  $11 R_{\text{MOON}}$  circular retrograde orbit characterized by a certain inclination and  $\Delta \Omega$  and its height corresponds to the best full-Corona observation offered by the eclipse passage: it is the least number of  $R_{\text{Sun}}$  at which during the passage it is possible to observe the Corona at  $360^\circ$ . An upper threshold equal to  $30 R_{\text{Sun}}$  was selected to identify the couples of values  $i - \Delta \Omega$  that offer a scientifically relevant full-Corona observation during the passage, i.e. the values corresponding to the portion of the surface below the threshold.

Similarly, in Figure 2.15 is shown an analogous plot in which now the height of each point corresponds to the amount of time (in minutes) per eclipse passage during which it is possible to observe (only partially) the inner region of the Corona up to  $5 R_{\text{Sun}}$ . As aforementioned, these observations will occur at the beginning and the end of the eclipse passage and they will last approximately the same so that for each passage there will be two distinct periods lasting half of the overall time per eclipse passage shown in the picture.

This is the reason why a lower threshold was fixed at 30 minutes as it can be used to identify the couples of values  $i - \Delta \Omega$  for

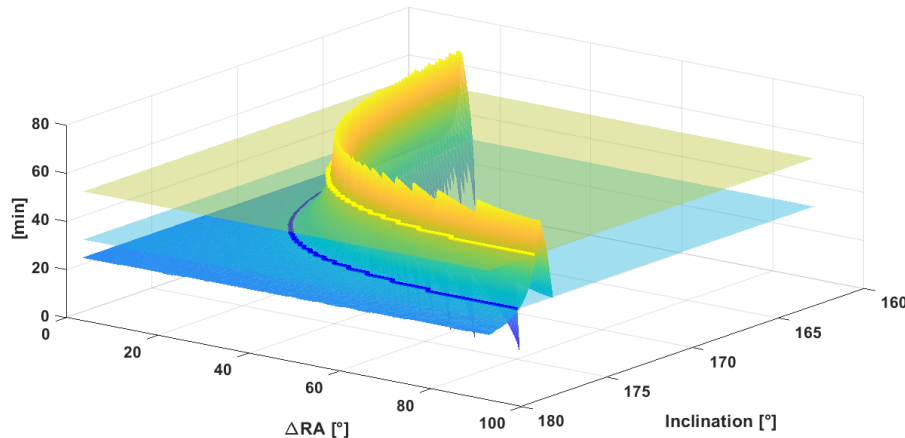


**Figure 2.15:** Duration of the observation of the inner corona up to  $5 R_{\text{sun}}$

which during the eclipse passage the inner Corona will be continuously observable for at least 15 minutes [3] (15 minutes in the beginning and 15 minutes in the end), which corresponds to the refresh rate of the payload, thus corresponds also to the minimum time which has to be available.

To be noted is that also an upper threshold was selected in this case, not because longer observations would not be interesting, but because longer observations mean cutting the eclipse cone very near its border, thus risking not intersecting it at all and losing the chance to do any sort of observation: this means that the upper threshold corresponds to an upper boundary set to avoid exiting the eclipse cone.

The result is that, concerning the observation of the inner regions of the Corona, the interesting couples of values correspond to the portion of the surface comprised between the two thresholds.

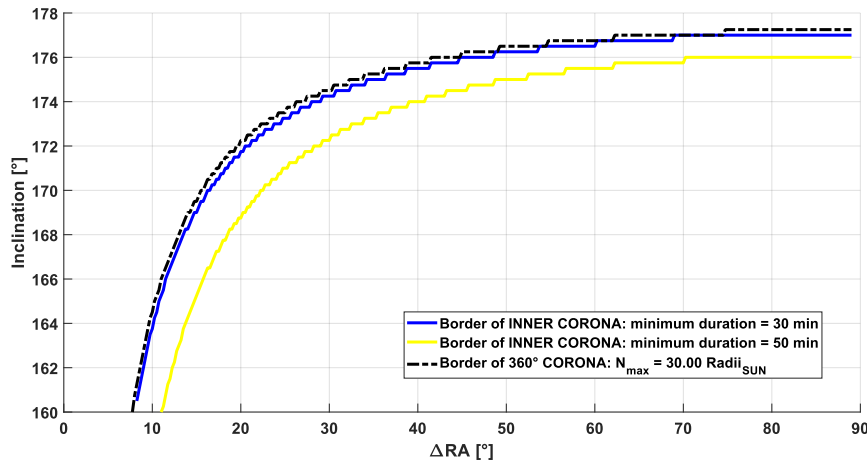


**Figure 2.16:** Observation zones as a function of orbital parameters

Figure 2.16 shows the results directly in the  $i$ - $\Delta\Omega$  plane. As can be easily noticed, when the spacecraft exits the full-Corona safe region, it enters the inner-Corona interesting region; this leads to the strategy that allows a misalignment with respect to the axis of the cone. Thus, rather than only taking care of the full-Corona observation and maneuvering whenever it crosses the 360-Corona border, waiting to apply the maneuver correction till it reaches the out-of-eclipse border would allow the collection of interesting inner-Corona observation, until the proximity of the exit from the eclipse cone.

### 2.3.2 Example of the applied strategy

Figure 2.17 shows the evolution of RAAN and inclination of the s/c over its entire operative lifetime when subjected to the SK strategy described above. The Vertical dotted lines correspond to SK maneuvers: they are all maneuvers intended

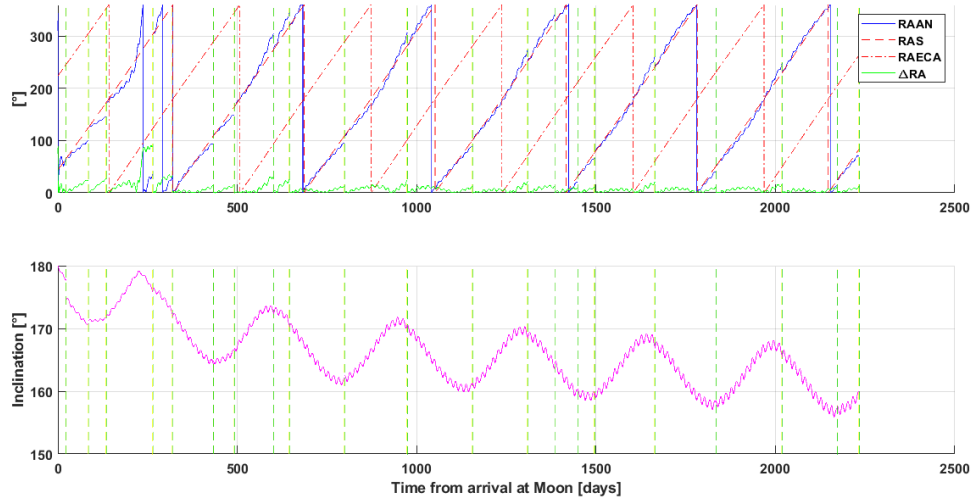


**Figure 2.17:** Applied example of the SK strategy: evolution of RAAN and inclination

to correct the RAAN according to the coupled tracking of  $i - \Delta\Omega$  discussed above, all except the first one.

The first maneuver is a plane change maneuver intended to initially decrease the inclination of the orbit (the transfer puts the s/c on an orbit with inclination equal to  $180^\circ$ ): this is done because the sun-following / de-risking behavior of the retrograde orbits is obtained only if the initial inclination is slightly lower than  $180^\circ$ .

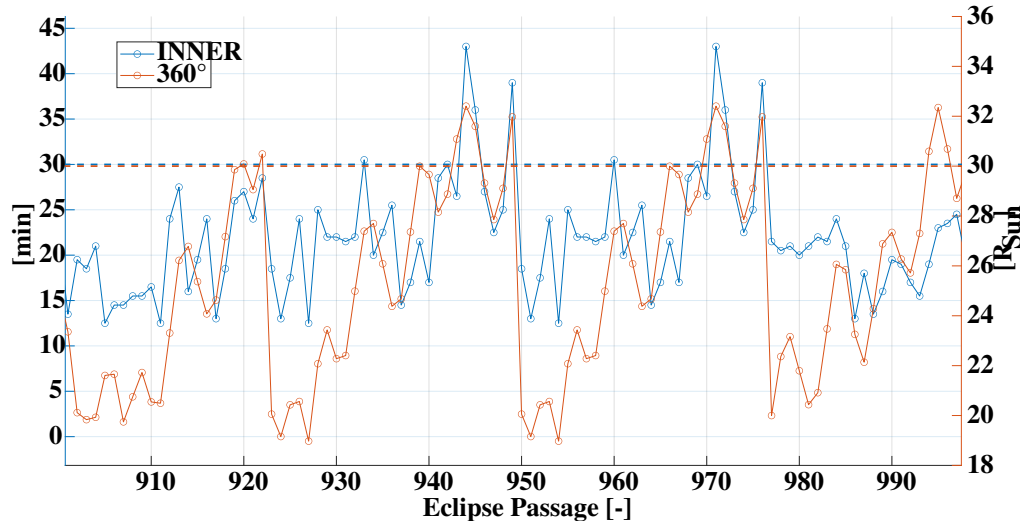


**Figure 2.18:** Applied example of the SK strategy: eclipse passages observational quality

Figure 2.18 shows the observational performances of this strategy. Both the full-Corona and the inner-Corona observation quality parameters are plotted at once to show that actually whenever the  $360^\circ$  observation quality becomes unacceptable, the duration spent observing the inner regions of the Corona becomes interesting, confirming the effectiveness of the designed strategy.

Total $\Delta V$ [m/s]	N. maneuvers	Max $\Delta V$ for single maneuver [km/s]	Total N. of eclipse passages
0.692	21	50.284	1574

**Table 2.4:** SK strategy results

Table 2.4 summarize the effectiveness and improvements on the costs of this orbit.



$R_{Sun}$ at which is visible full-Corona observations	Total N. of eclipse passages
30	1378
25	840
22.5	526
20	122

**Table 2.5:** SK strategy results: full-Corona observation

Duration of the observation	Total N. of eclipse passages up to $5 R_{Sun}$
30	100
25	324
20	122

**Table 2.6:** SK strategy results: Inner corona observations

## 2.4 Transfer to chosen orbit

To achieve the desired lunar orbit, the [s/c](#) must execute a transfer from Earth to the Moon. This transfer follows impulsive guidance theory, and the model employed for propagating the [s/c](#) dynamics involves a 4-body model including the [s/c](#), Earth, Moon, and the Sun. The simulation is based on the concept introduced in reference [18], which involves computing a transfer in the Planar Bicircular Restricted Four-Body Problem ([PBRFBP](#)). For Luminous transfer computation, this idea is extended to a three-dimensional, four-body system incorporating ephemerides. Notably, this preliminary analysis does not factor in drag and [SRP](#). Given that the mission is scheduled to commence no earlier than 2027, various transfer options have been identified for each month of that year. Anyhow, please note that the same launch pattern is endlessly repeating, hence it is possible to identify transfers with similar insertion  $\Delta V$  every month.

In this scientific mission, the transfer duration is not the main driver for transfer selection, although it should remain within a reasonable timeframe, at least less than one year as we want to perform a 6-year mission. Instead, the selection is based on achieving the minimum insertion  $\Delta V$  at the Moon. The emphasis on insertion  $\Delta V$  is due to the fact that the initial  $\Delta V$  required to escape Earth is provided by the launcher. This strategic choice aims to minimize the propellant consumption of the [s/c](#) throughout the mission, a crucial consideration given the demanding nature of [SK](#).

Opting for a Geostationary Transfer Orbit ([GTO](#)) as parking orbit is a strategic choice to minimize the initial  $\Delta V$  required for the transfer. It is worth mentioning that, as this  $\Delta V$  is provided by the launcher, a circular parking orbit is also a feasible alternative. [GTO](#) was kept because it was the initial selection made to minimize the initial  $\Delta V$  (680 m/s) to have the possibility to use a large variety of launchers. As in the end Falcon 9 will be used, a further analysis of the possibility of having a circular parking orbit should be made.

### 2.4.1 Best transfer

In [Figure 2.19](#), the optimal transfer with minimal  $\Delta V$  requirements is presented. It stems from the utilization of a distinct algorithm, leveraging the alignment of the parking orbit within the ecliptic plane. Following the insertion  $\Delta V$ , a plane change is executed to align with the desired final orbit, resulting in a demanding initial [SK](#) maneuver. The [s/c](#) executes an insertion  $\Delta V$  with a magnitude of 377 m/s.

The departure is scheduled for March 1, 2027, with lunar insertion planned for May 4, 2027. The Time of Flight ([TOF](#)) is quite long but as said previously, the primary objective is to minimize propellant consumption as it directly correlates with reducing the size, mass, and ultimately the cost of the [s/c](#). This becomes particularly significant in scenarios involving the realization of multiple vehicles.

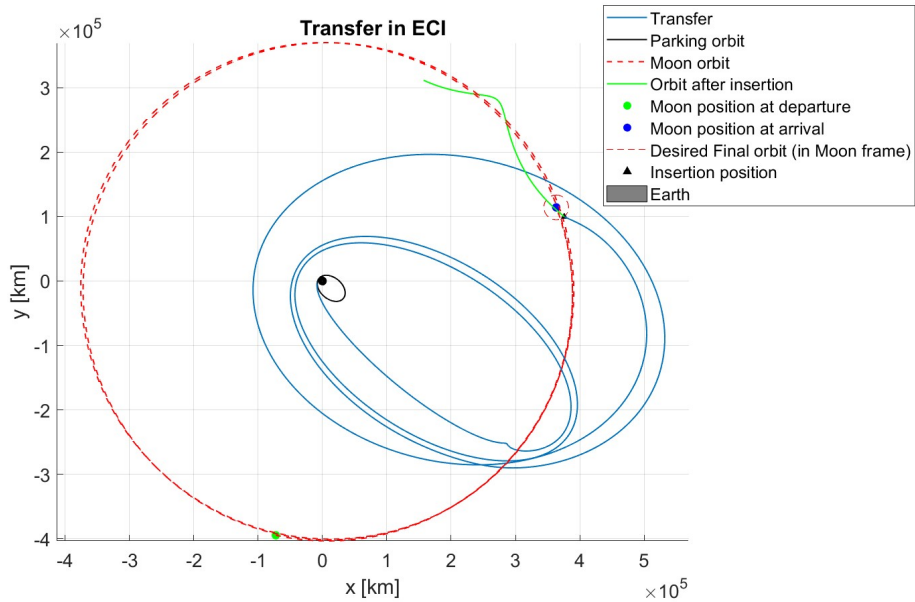


Figure 2.19: Best transfer for 2027

#### 2.4.2 Other transfers

In this simulation, the parking orbit aligns with the Moon's orbital plane, sharing comparable values for both RAAN and inclination. Optimization is achieved by adjusting the time of departure and the argument of perigee, where the initial impulse is applied, aiming to identify the configuration that results in the lowest insertion  $\Delta V$  over the course of the month.

Departure	Arrival	Insertion $\Delta V$ [m/s]
12 Jan 2027	11 Feb 2027	560
14 Feb 2027	23 May 2027	609
30 April 2027	31 May 2027	452
17 May 2027	17 June 2027	463
28 June 2027	28 July 2027	545
18 July 2027	27 Aug 2027	573
31 Aug 2027	11 Oct 2027	604
16 Sept 2027	16 Oct 2027	582
19 Oct 2027	24 Oct 2027	606
7 Nov 2027	23 Nov 2027	575
7 Dec 2027	12 Dec 2027	610

Table 2.7: Available transfers

#### 2.4.3 Trade-offs and margins

The current comparison of transfers to determine the optimal one relies on the insertion  $\Delta V$ . However, it is crucial to consider that the potential need for SK maneuvers to align to the final desired RAAN and inclination targeted in Mission Analysis (MA) play a significant role in the total  $\Delta V$  budget. Thus, it might be the case the optimal overall transfer minimizing the overall budget is not the one with minimum insertion  $\Delta V$ . Given the preliminary nature of this analysis, further optimizations shall be explored later.

Regarding safety margins, a conservative approach has been taken, setting the margin at 20.5% of the highest computed value (610 m/s, for December 2027 transfer, check Table 2.7), resulting in a margin-adjusted  $\Delta V$  of 735 m/s. While this



margin deviates from standard practices of max 5% or 10 m/s for trajectory maneuvers + 10 m/s for the Moon approach, it serves the purpose of accommodating any unforeseen issues. It is worth noting that this margin is subject to reduction in subsequent phases of the mission design.



## 2.5 Future Developments

It is important to highlight a fundamental defect of the analysis which led to the proposed orbital strategies: it never considered the idea of guessing which could be the mechanisms underlying the evolution of the quasi-circular orbits of interest because it is easy to verify how difficult it is to recognise any robust pattern.

Although, this idea came up in the attempt of understanding a surprising fact: propagating for 6 years starting from any of the orbital states at the arrivals of the transfers provided in subsection 2.4.2, the inclination evolves essentially confined to the initial one, approximately equal to  $175^\circ$ , guaranteeing to intersect the eclipse cone  $\sim 80\%$  of the orbits without doing a single maneuver - these arrival states were then inserted as initial guesses into an "optimization" algorithm searching for the 6 years propagation with the best ratio between eclipse passages and orbital periods by perturbing the initial RAAN and inclination; it led to propagations naturally intersecting the eclipse cone up to 90 % of the revolutions around the Moon, as the one in Fig. 2.20.

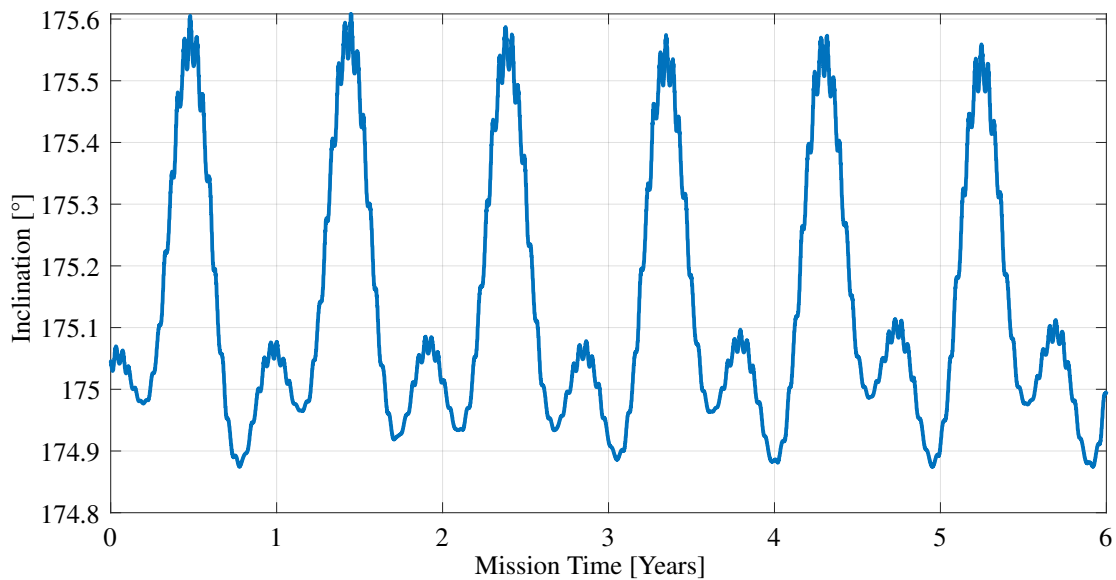


**Figure 2.20:** Example of an "optimized" natural propagation

This was totally unexpected being in open contrast with the results presented in 2.3.1 that brought to neglecting solutions exploiting the natural evolution of the inclination; this simply demonstrated that we did not explore sufficiently the entire spectrum of possibilities offered by such orbits.

To understand why this surprising states propagate in this peculiar way, we firstly decoupled the Sun disturbance from the Earth one searching for some clues and easily discovering that the main role is played by the Earth, which actually overrules the Sun in perturbing these kind of lunar orbits. Given the Earth predominance, the confinement at the suspect inclination of  $175^\circ$  - which clearly reminds of the  $5^\circ$  inclination of the Moon orbit around the Earth - suggests the responsibility of some sort of resonance in the motion of the spacecraft and the Earth as seen from the central perspective of the Moon. Further speculation on this orbit should also consider their origin as the result of the optimization of a transfer between Earth and Moon.

All these aspects lead to the clear evidence that the chosen strategy is far from being the optimal one; anyway a possible future first step could attempt to combine the presented approach - based on the attempt of mapping the orbital parameters into observation quality parameters - with an exhausting research of orbits which naturally offer vast possibility to do science in eclipse.

## 2.6 Disposal

The choice of a lunar impact for the *s/c* disposal is grounded in considerations from past lunar missions and feasibility assessments. Return to Earth was discarded because of the high  $\Delta V$  needed and because no scientific samples were performed by the mission. Heliocentric graveyard orbit was also discarded because of the high  $\Delta V$  and also because it is more of use for missions evolving around Earth-Moon Lagrangian points. Specific impact regions have been identified to ensure the preservation of lunar artifacts [19]. Figure 2.21 highlight four regions that are conducive to impact without compromising the Moon’s historical artifacts.

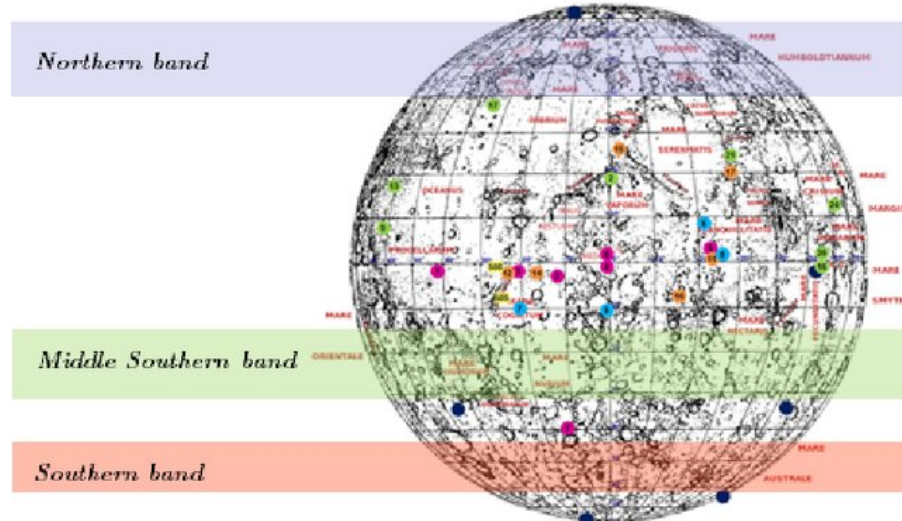


**Figure 2.21:** *Impact regions*

- Northern latitude band: from  $40^{\circ}\text{N}$  to  $73^{\circ}\text{N}$
  - Middle Southern latitude band: from  $15^{\circ}\text{S}$  to  $32^{\circ}\text{S}$
  - Southern latitude band: from  $43^{\circ}\text{S}$  to  $63^{\circ}\text{S}$
  - The entire Moon's far side

Here is an example of a potential disposal within the Middle Southern latitude band ([Figure 2.22](#)). Scheduled for June 17, 2033, six years after launch, the s/c is set to impact at a latitude of 20.6°S. This disposal involves three maneuvers, with a cumulative  $\Delta V$  of 297m/s.

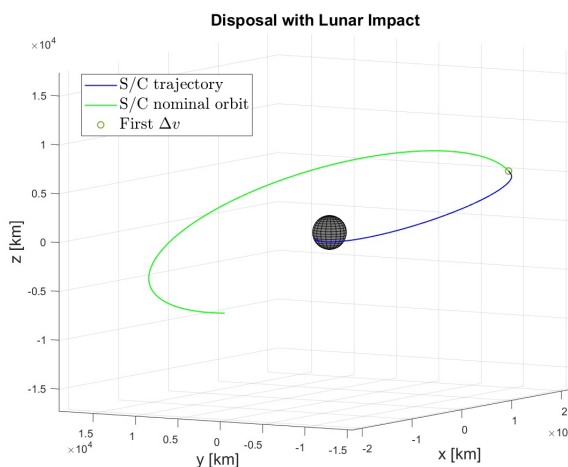


**Figure 2.22:** Impact in Middle Southern region



Next, consider this illustration of a potential disposal in the Northern latitude band (Figure 2.23). The disposal is scheduled for June 16, 2033, after six years from the [s/c](#) launch. The orbiter impacts at a latitude of 50°N, and the disposal involves three maneuvers, resulting in a total  $\Delta V$  of 374m/s.

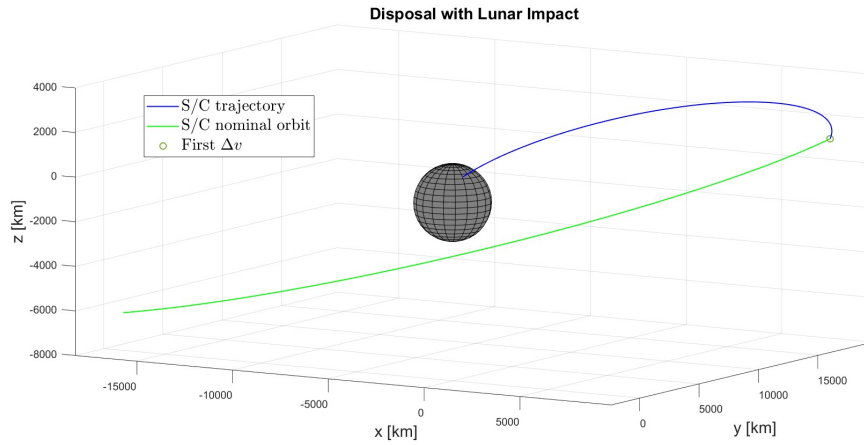


**Figure 2.23:** Impact in Northern region

As the Artemis program advances and more scientific activities are anticipated on the Moon in the years to come, the boundaries of these regions may undergo modifications. To accommodate potential changes and account for any unforeseen issues, a margin of 40.4% is applied to the highest required  $\Delta V$  (374 m/s from Figure 2.23), resulting in a margin-adjusted  $\Delta V$  of 525m/s. This margin was selected to be more conservative than the standard margin of max 5% or 10 m/s for deterministic maneuvers as the regions of impact might change and because as seen in the examples, those maneuvers' costs can change.



## 2.7 Launcher selection

The launcher selection has been driven by a series of trade-offs. The first step consisted of selecting only launchers from Western countries, such as Europe and the US, mainly for geopolitical reasons. Then, only launchers with the capability to bring a payload to the lunar orbit have been considered. In this way, a huge part of the launchers' market, specialized in bringing *s/c* to Low Earth Orbit (**LEO**), among which VEGA/VEGA-C, has been excluded. Also, launchers with a too-high payload capacity were excluded, since they were not useful for this mission. The three remaining selected launchers have been evaluated based on parameters such as reliability, cost, availability of launch opportunities, and the possibility of offering rideshare to other payloads (in order to reduce the mission launch cost). The launchers and the trade-off are discussed in the following [Table 2.8](#):

	Falcon 9 (Block 5)	Vulcan Centaur (with 0 solid boosters)	Ariane 6 (A62 configuration)
<b>Country</b>	US	US	EU
<b>Company</b>	Space-X	ULA	Arianespace
<b>Payload to Lunar Transfer Injection (LTI)</b>	1900 kg [20]	2300 kg[21]	3500 kg[22]
<b>Cost (in million USD)</b>	67 [23]	110 [24]	75 [25]
<b>Reliability</b>	100%	100%	Yet to be launched
<b>(in terms of number of launches/number of failures)</b>	(over 240 launches)[26]	(over 1 launch) [27]	
<b>Launch opportunities</b>	Launches very often	?	?
<b>Rideshare possibility</b>	Yes	Yes	Yes
<b>Payload Fairing</b>	13.1(H)*5.2(D) m [28]	15.55(H)*5.4(D) m [21]	14(H)*5.4(D) m [22]

**Table 2.8:** *Launchers' trade-off*

The Falcon 9 has been chosen both to transport the *s/c* to the parking orbit and to impart the initial  $\Delta V$  for the transfer trajectory because it is designed for such a task and it is the best in all the aspects considered in the above trade-off. The size and mass of LUMINOUS *s/c* align with Falcon 9's requirements, and the launcher can additionally furnish a kick stage, the Helios Kick stage [29] to provide the required initial  $\Delta V$ . Alternative launchers like Vulcan Centaur and Ariane 6 are good options as backup launchers due to their larger allowable mass and size, which make them particularly advantageous in scenarios involving the simultaneous launch of multiple *s/c*.

### 2.7.1 Launch location

The Falcon 9 has regular access to space from 3 launch sites:

- **Launch Complex 39A, Kennedy Space Center:** 28 degrees North of the equator, near the Atlantic Ocean, the launch complex is modified by Space X to support their launch vehicles.
- **Space Launch Complex 4E & Space Launch Complex 6, Vandenberg Air Force Base:** 34 degrees North of the equator.
- **Space Launch Complex 40, Cape Canaveral Air Force Station:** 28 degrees North of the equator.

The location of the launch of the mission will depend on the availability of the launch base, weather conditions, and ease of transport of the *s/c* and its components to the launch base.



## 2.8 Conceptual Operations

In this section a brief overview of the mission conceptual operations is presented, to put into perspective the timeframe of reference. Both a wide mission view and a single orbit view are presented.

### 2.8.1 Mission ConOps

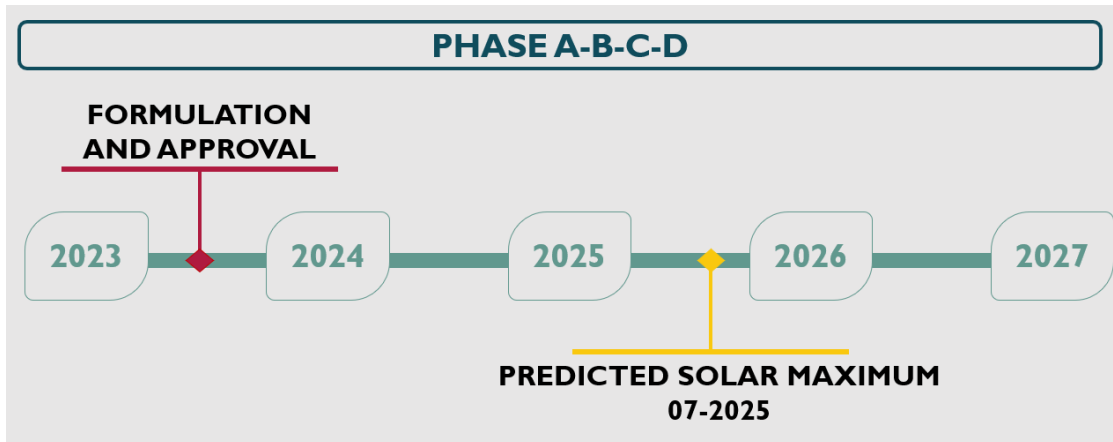


Figure 2.24: Phases A through D

As can be seen in Figure 2.24, the first few years of development overlap with the predicted solar maximum, meaning that a launch in July of 2025 would allow the spacecraft to study almost entirely the decreasing half of the solar cycle. Remember that a launch is not allowed before 2027, therefore the next best opportunity to launch, from a scientific point of view, is at the start of 2027. Of course, this is only true when considering the importance of this particular half of the solar cycle; since the real constraint is that the mission lasts 6 years, any launch after 2026 is allowed and would result in the success of the mission, even if it focuses on studying a different part of the solar cycle.

Considering the best transfer of 2027, the mission proceeds in phase E, as shown in Figure 2.25. After a brief verification period, that takes place in the Low Earth Orbit environment, the transfer to Lunar orbit starts and brings the spacecraft into operational orbit after about 2 months of transfer.

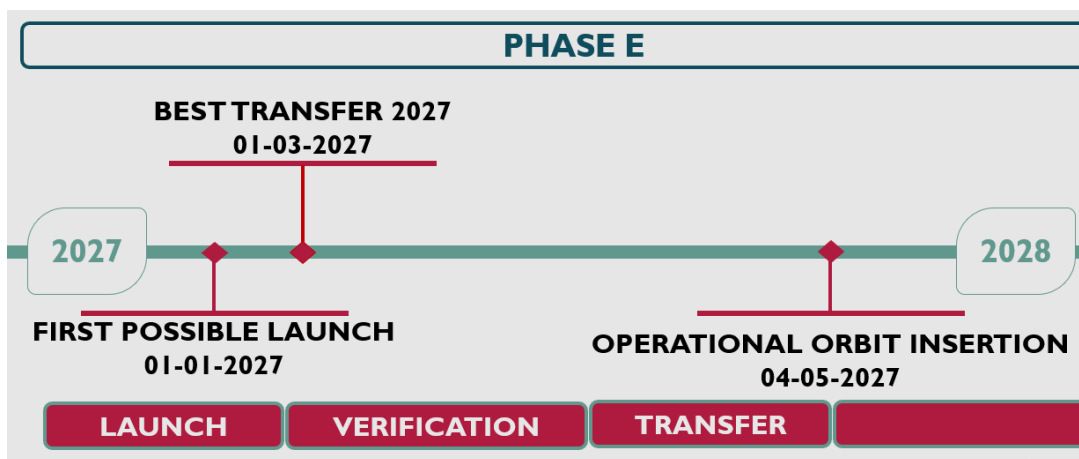


Figure 2.25: Phase E

Finally, as can be seen in Figure 2.26, the mission reaches 6 years of operations just before the further prediction for the solar minimum [7]. From there it is possible to continue with the study of solar corona if the spacecraft is still in operative conditions, otherwise the mission proceeds to disposal.

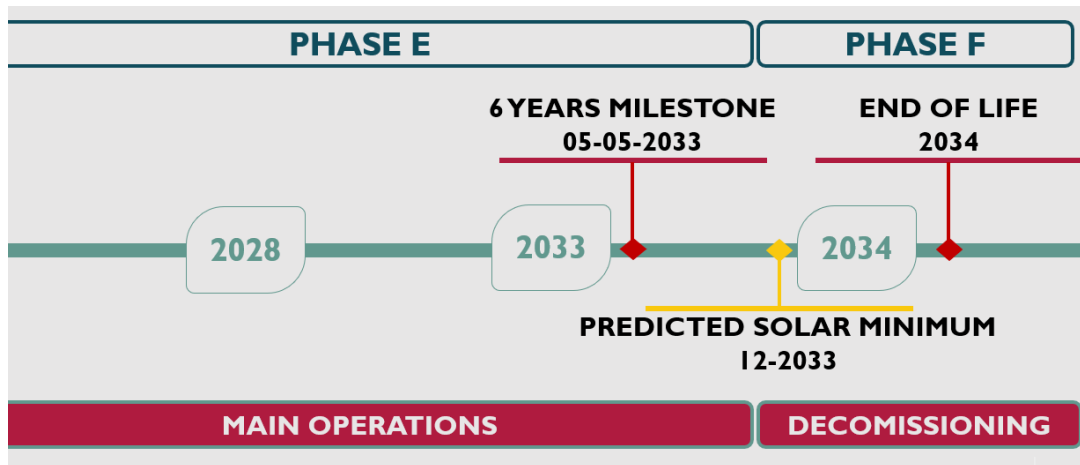


Figure 2.26: Phases E and F

### 2.8.2 Orbit ConOps

Hereafter is shown the ConOps during one typical orbit. These are valid during the entire mission, despite the changes in orbital parameters from the natural orbit degradation.

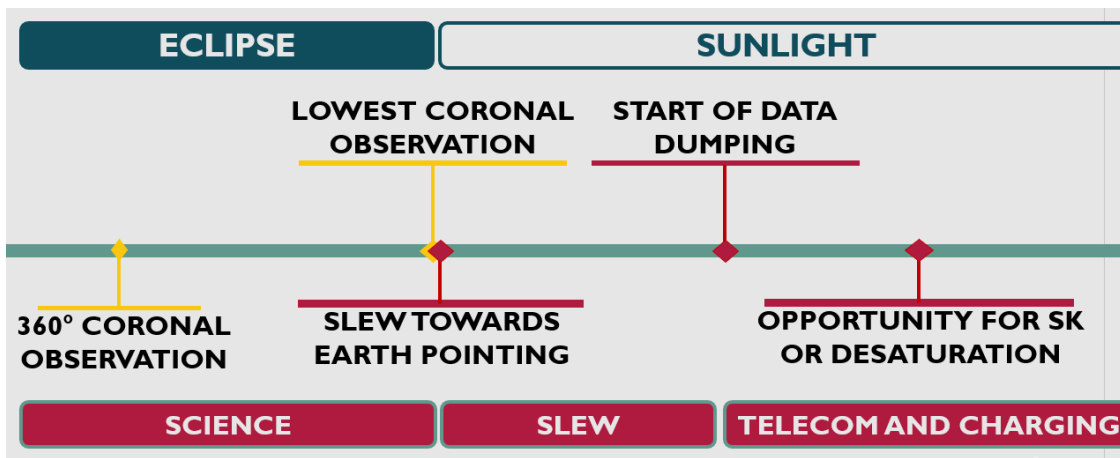
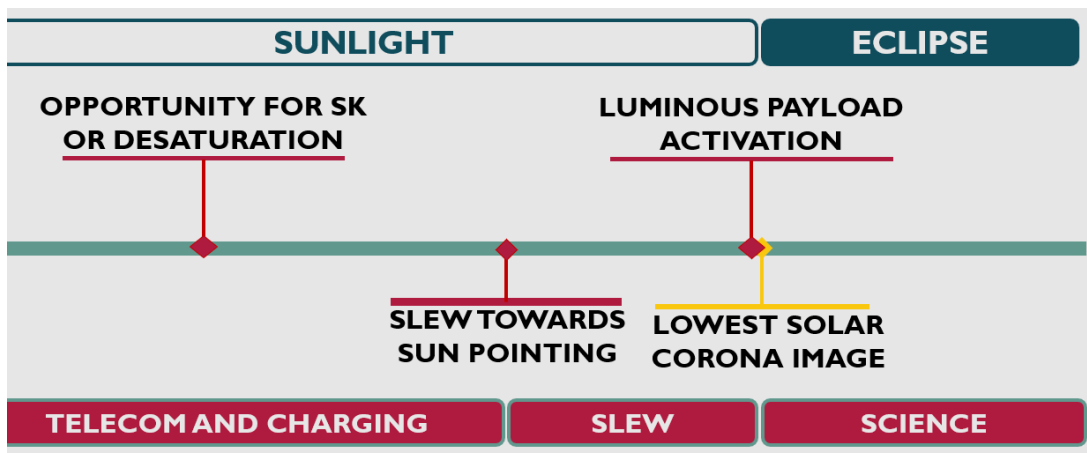


Figure 2.27: First half of typical orbit

As can be seen in Figure 2.27, in the middle of the eclipse there is the availability of 360 degrees observation, while the observation of the lower corona must happen when the spacecraft is close to the limb of the Umbra projected by the Moon. Just after the end of observation, the spacecraft proceeds to a slew maneuver that switches between having the payload in a Sun-pointing condition to the High Gain Antenna (HGA) being in an Earth-pointing condition. This pointing is then kept for the entire sunlit phase to allow for data dumping. The power production is not an issue thanks to the Solar Array Drive Assembly (SADA) that allows for constant turning of the solar arrays and therefore constant power production during this phase.

In Figure 2.28 the second half of the orbit is shown. During the sunlit phase, there is a possibility of performing station-keeping maneuvers or any slew maneuver necessary to desaturate the reaction wheels. Just before entering the Umbra, another slew maneuver is performed, to once again bring the payload in sun-pointing. Here the situation is symmetrical to the first half: at the limb, there is once again the acquisition of lower corona images, while going further into the eclipse allows for the acquisition of 360-degree pictures of the higher corona.



**Figure 2.28:** Second half of typical orbit

# Chapter 3 Attitude Determination and Control Subsystem

The mission design and the system configuration ask the [ADCS](#) to fulfill 3 main functionalities during each revolution around the Moon:

- *To point with the required accuracy and stability at the solar corona while imaging (Primary science mode):* it constrains the axis of the payload ( $-\hat{\mathbf{X}}$  body frame axis) to be pointed at the center of the Sun.
- *To point with the required accuracy<sup>1</sup> at the Earth while telecommunicating (Communication mode):* it constrains the HGA axis to be pointed at the Earth. The HGA is hosted on the spacecraft face whose outer normal is coincident with the  $\hat{\mathbf{Y}}$  body frame axis; if it is fixed on the spacecraft, its axis will coincide with  $\hat{\mathbf{Y}}$ .
- *To ensure a power-positive attitude, pointing the solar panels at the Sun (Charging mode):* the adoption of Solar Array Drive Assemblies [SADA](#) is contemplated; they would allow the solar panels to rotate around the  $\hat{\mathbf{Z}}$  body frame direction.

Let's split a generic operational orbit into its shadowed (*In-Eclipse*) and enlightened (*Out-Of-Eclipse*) phases: while the choice of pointing the payload at the Sun during the whole eclipse passage naturally derived from the objective of maximizing the solar corona imaging opportunities, deciding the attitude profile for the rest of the orbit passed through the comparison of two main proposals, discussed in the following.

## 3.1 Attitude Determination

The most demanding pointing precision and stability (occurring during the *Primary science mode*) were defined by taking as reference the capabilities exhibited by the SOHO spacecraft([30]):

- Pointing accuracy: 10 arcsec
- Pointing stability: 1 arcsec over 1.5 minutes

### 3.1.1 IMU

Given such a demanding pointing budget, the obvious necessity to equip the spacecraft with a high precision Inertial Measurement Unit ([IMU](#)) could be satisfied with the adoption of a sensor package as the *ASTRIX 120*, from Airbus.

ASTRIX 120	Values
Full performance measurement range	$\pm 10^\circ/\text{s}$
Measurement range	up to $\pm 140^\circ/\text{s}$
Scale factor angular resolution	$\sim 0.01 \text{ arcsec/LSB}$
Mass	6.5 Kg

**Table 3.1:** The specifications of the IMU

Further details can be found in Reference [31] which is the datasheet of the product.

### 3.1.2 Star Trackers

The Attitude Determination architecture has to rely on the adoption of the most performing attitude sensors on the market, i.e. the choice of Star Trackers is straightforward. It's well-known good practice to select sensors capable of determining

<sup>1</sup> The accuracy demanded by the HGA is equal to  $1^\circ$



the attitude with precision at least one order of magnitude better than the required pointing accuracy, then the *High Accuracy Star Sensor ASTRO XP* from *jena-optronik* is an example of a possible solution.

ASTRO XP	Values
Field of View	< 3.3° circular
Angular rate	0.5°/s, 10% acquisition tracking
Update Rates	2,4,8 Hz
Mass	6.9 Kg

**Table 3.2:** The specifications of the Star Trackers

The complete datasheet can be downloaded at [32].

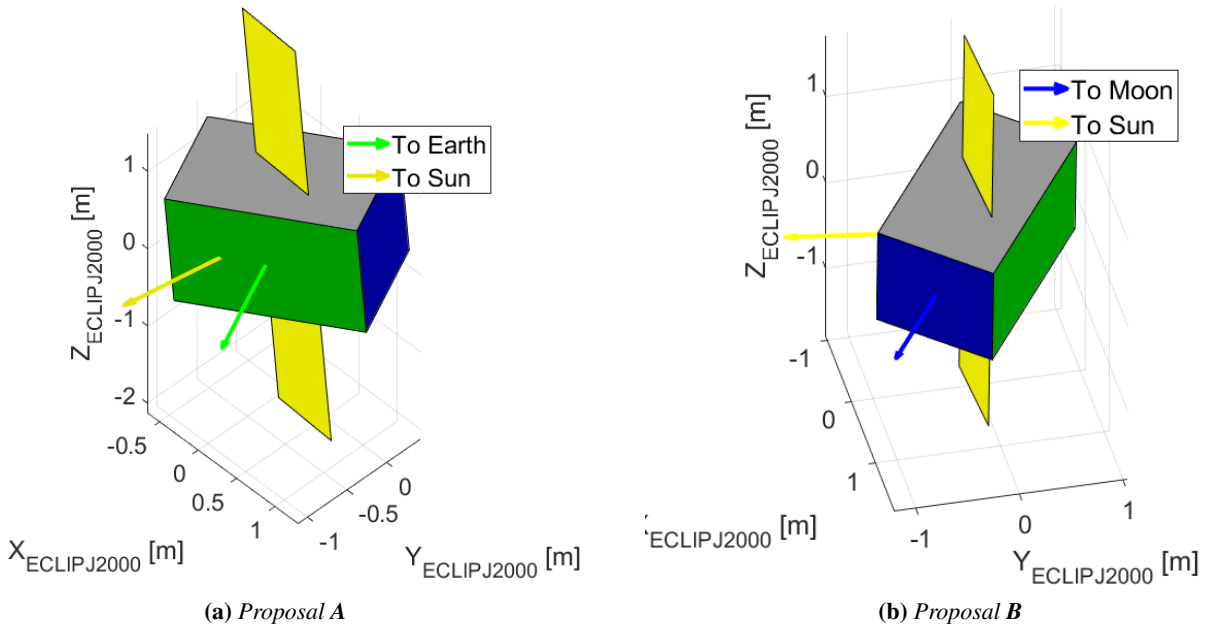
The spacecraft would be equipped with a couple of them for redundancy since each of them can provide full attitude determination autonomously. Whenever the body attitude determination needs to be initialized starting from an unknown initial condition - e.g. during the Verification Phase after the release from the launcher or in case of emergency - a set of star sensors, in combination with the info coming from the **IMU**, is meant to provide the position of the Sun with respect to the body frame to ensure the possibility to initializing the Star Trackers (i.e. the nominal attitude determination algorithm) without risking to expose them to the sunlight.

## 3.2 Out-Of-Eclipse Attitude Strategies

As mentioned in the introduction, the main trade-off concerning the **ADCS** regarded the definition of the target attitude when out of the eclipse cone, i.e. when not doing science; two main solutions were investigated.

The main concept shared between the proposals is to exploit at most the eventual adoption of the **SADA** permanently constraining their axis ( $\hat{Z}$  body frame direction) to be kept orthogonal to the Sun direction, such that the additional degree of freedom allowed by the **SADA** mechanism would allow keeping the Solar Aspect Angle of the solar arrays under a  $1^\circ$  threshold coming from the **EPS** concurrent analysis, such that a positive-power attitude would be constantly ensured.

**Figure 3.1:** Visualization of *Out-Of-Eclipse* target attitudes with respect to the celestial bodies. The green face hosts the **HGA** and its outer normal is  $-\hat{X}$ . The blue face hosts the payload and its outer normal is  $\hat{Y}$ . The yellow panels represent the solar arrays, which can rotate around  $\hat{Z}$  axis.





### 3.2.1 Proposal A: Permanent Earth Visibility

The first proposal (Fig. 3.1a) is to complete the attitude definition, coupling the orthogonality constraint acting on the  $\hat{\mathbf{Z}}$  body frame direction with a constraint on the alignment of the  $\hat{\mathbf{Y}}$  body frame axis (aligned with the HGA axis) with the Earth direction, to keep at the same time also the HGA constantly in the position of establishing a ground-link.

In practice, given the directions of the Sun and Earth, the  $\hat{\mathbf{Y}}$  body frame axis is aligned with the spacecraft-Earth line while the  $\hat{\mathbf{Z}}$  body frame direction is the result of the vectorial product of the two celestial bodies directions - to guarantee its orthogonality with the Sun; then  $\hat{\mathbf{X}}$  closes the triad.

### 3.2.2 Proposal B: Modified Nadir Pointing

The alternative proposal (Fig. 3.1b) is to couple the orthogonality constraint acting on the  $\hat{\mathbf{Z}}$  body frame direction with a constraint on the alignment of the  $-\hat{\mathbf{X}}$  body frame axis with the Moon direction, in a sort of Nadir pointing enriched by the underlying permanent power-positive configuration.

In practice, given the directions of the Sun and Moon, the  $-\hat{\mathbf{X}}$  body frame axis is aligned with the spacecraft to Moon line while the  $\hat{\mathbf{Z}}$  body frame direction is the result of the vectorial product of the two directions - to guarantee its orthogonality with the Sun; then  $\hat{\mathbf{Y}}$  closes the triad.

In this case, the HGA would not be constantly pointed at the Earth, thus a dedicated sequence of slews would be necessary: to avoid this, the proposal encompasses the adoption of a robotic arm providing the HGA with 2 angular degrees of freedom which would allow directing the antenna at the Earth whenever the correspondent spacecraft face is in sight of our planet.

### 3.2.3 Conjunctions

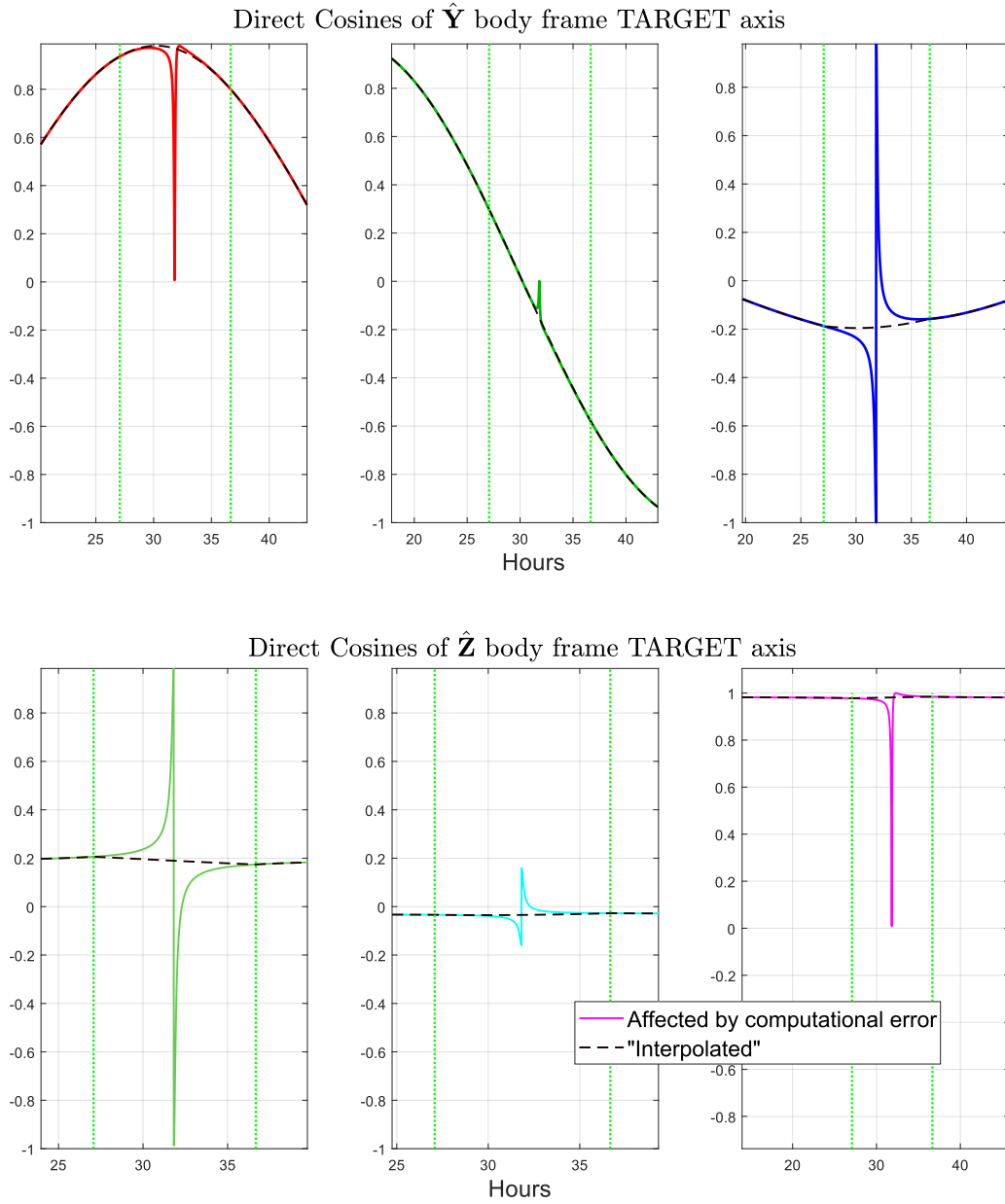
Both solutions define the  $\hat{\mathbf{Z}}$  body frame axis as the result of a vectorial product computation, which is ill-defined when the two vectors are close to being parallel; this occurs whenever the spacecraft finds itself aligned with the two celestial bodies of interest - i.e. in conjunction with them. In this situation, both the target attitude and - as a consequence - the control law are wrongly computed.

Assuming a sufficiently accurate knowledge of the proximal future evolution of the orbital motion employing proper Navigation, the following strategy can be implemented: whenever conjunction is approaching, let's estimate the target attitude in its neighborhood and identify the boundaries of the time interval during which the computational error is considered unacceptable, then interpolate the chosen angular parameters (Direct Cosines Matrix components, in the present case) representing the target attitude in between the problematic time interval.

For simplicity and for guaranteeing the orthonormality of the represented target attitude, the "interpolation" consisted of an Euler Axis rotation between the target attitudes retrieved at the boundaries of the time interval. An example of this method can be appreciated in Fig. 3.2.



**Figure 3.2:** Example of the computational error due to spacecraft conjunction with Moon and Sun during Out-Of-Eclipse phase (Proposal **B**). The vertical dotted green lines show the boundaries of the identified problematic time interval. The  $\hat{X}$  body frame is not plotted since in the Proposal **B** it is the well-defined axis.



### 3.2.4 Trade-off: statement

The trade-off between these two proposals was based on the following discussion.

Proposal **A**:

- it has the advantage of virtually constantly providing opportunities to communicate with the ground, enormously relaxing the design of a robust communication schedule.
- two main potential drawbacks were identified: in this case, our attitude would follow the Earth in its apparent revolution around the Moon which lasts circa 29 days, thus all the lateral surfaces of the spacecraft would be progressively exposed for days to the sunlight, which may have significant repercussions on the **TCS** design; another identified potential hazard concerns the **SADA**, who typically act imposing a constant angular rate to the arrays: in this case, the ideal angular rate profile is not expected to be constant.

Proposal **B**:



- it has the advantage of avoiding any large slew to transit from the out-of-eclipse attitude to the in-eclipse attitude, which is not, in general, true for the other solution, compared to which it is expected to be less critical also from the **TCS** design perspective since now the attitude would complete a revolution on its axis orthogonal to the Sun in one orbital period, equal approximately to 66 hours - to be compared with the 29 days of the alternative.
- one major drawback is the intrinsic risk represented by the adoption of the robotic arm: in principle, it could be avoided by planning dedicated slews for telecom, which could also represent the mitigation of any failure leading to the blockage of the arm. In any case, the telecom scheduling is expected to be much more involved compared to the other proposal.

### 3.2.5 Trade-off: analysis

The team ran simulations in the Simulink® environment to feed the trade-off between the Out-Of-Eclipse strategies, to size the proposed architectures, and to assess their feasibility.

#### Simulations specs

The simulations were conducted trying to include the most significant elements. They were characterized by the following main features:

- they include the modeling of the Solar Radiation Pressure and Gravity Gradient disturbances
- the orbital dynamics (assumed to be reasonably decoupled from the attitude dynamics) comes from the Mission Analysis orbital propagations
- the inertia matrix of the spacecraft is retrieved from the CAD model of the spacecraft, which is not purely diagonal if expressed in the body-frame coordinates; the inertia matrix is not dependent on the tanks filling - which are considered constantly full - nor on the rotation of the solar arrays depending on the **SADA** control law - computation suggested the negligibility of this last dependence.
- the attitude determination error of the Star Tracker is introduced dirtying the ideal output of the attitude determination algorithm with an attitude error rotation matrix coming from an independent simulation of the Star Tracker performances<sup>2</sup>.
- the dynamics of the Reaction Wheels (**RW**) actuation (the coupling with their electrical motors dynamics) is neglected and the provided angular momentum exchange ideally follows the command provided by the control algorithm.
- the simulation replicates the adoption of a pyramidal configuration with 4 **RW**, able to exchange angular momentum in any direction even if one of them fails.

#### Control Algorithms

The following algorithms have been implemented:

- For both the Out-Of-Eclipse and In-Eclipse phases, a Non-Linear Proportional Derivative tracking control algorithm was implemented, tuned by trial and error to satisfy the related accuracies.
- For the slews, a Non-Linear Proportional Derivative slewing control algorithm was implemented, tuned, and d by trial and error.

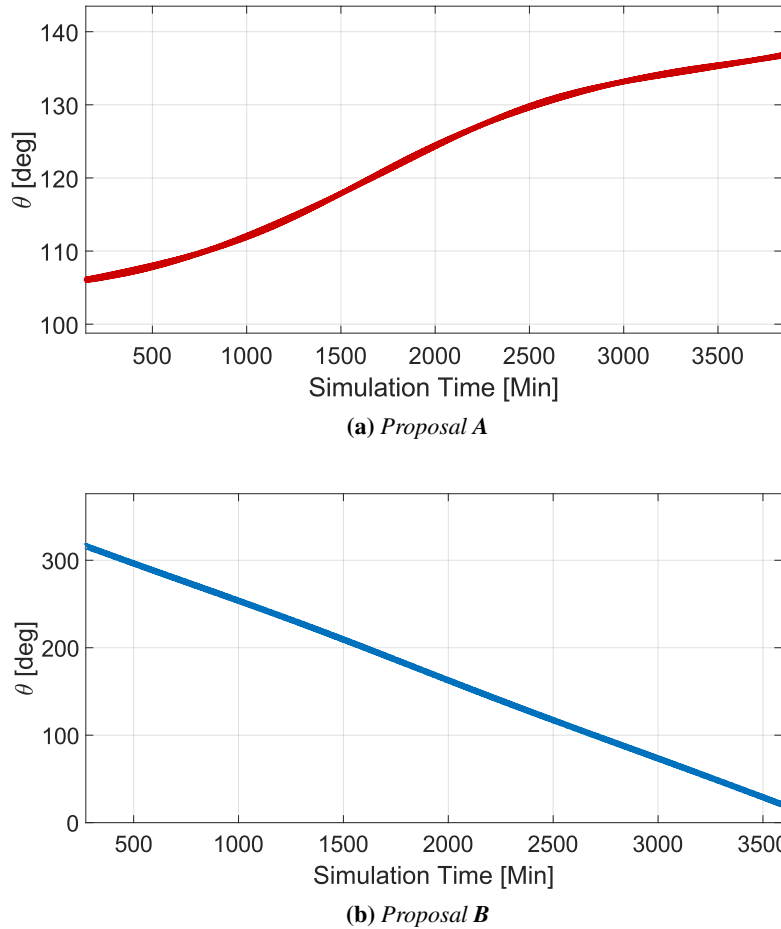
#### The **SADA** issue

The results confirm (Fig. 3.3a) that Proposal A would ideally require a non-constant angular rate to keep an adequate constant solar pointing, which if implemented in reality could lead to a higher risk of failure (compared to the constant rate case) and repercussions on the **ADCS** as a whole due to the introduction of time-varying counter torques derived by the action of the **SADA** mechanisms, whose potential severity would need to be assessed in future Project phases.

<sup>2</sup> To avoid including in the simulation a vast catalog of stars, which would be required in reality since the sensor would scan vast portion of the celestial sphere, a dedicated simulation of a Star Tracker scanning a narrow portion of the sky was separately performed



**Figure 3.3:** Example of the ideal angular profile to be commanded to the SADA



Anyway, if the varying-rate solution resulted being not practicable, the quasi-linearity of the ideal profile suggests that if a constant angular rate were implemented, it would still be possible to follow the Sun, but obviously with an expected increase of the average solar aspect angle at the arrays, which would probably ask for a counterbalance to the [EPS](#) and the scheduling of the Operations.

Regarding **Proposal B**, the results (Fig. 3.3b) show that a constant angular rate would be perfectly suitable in that case.

### RW and thrusters sizing

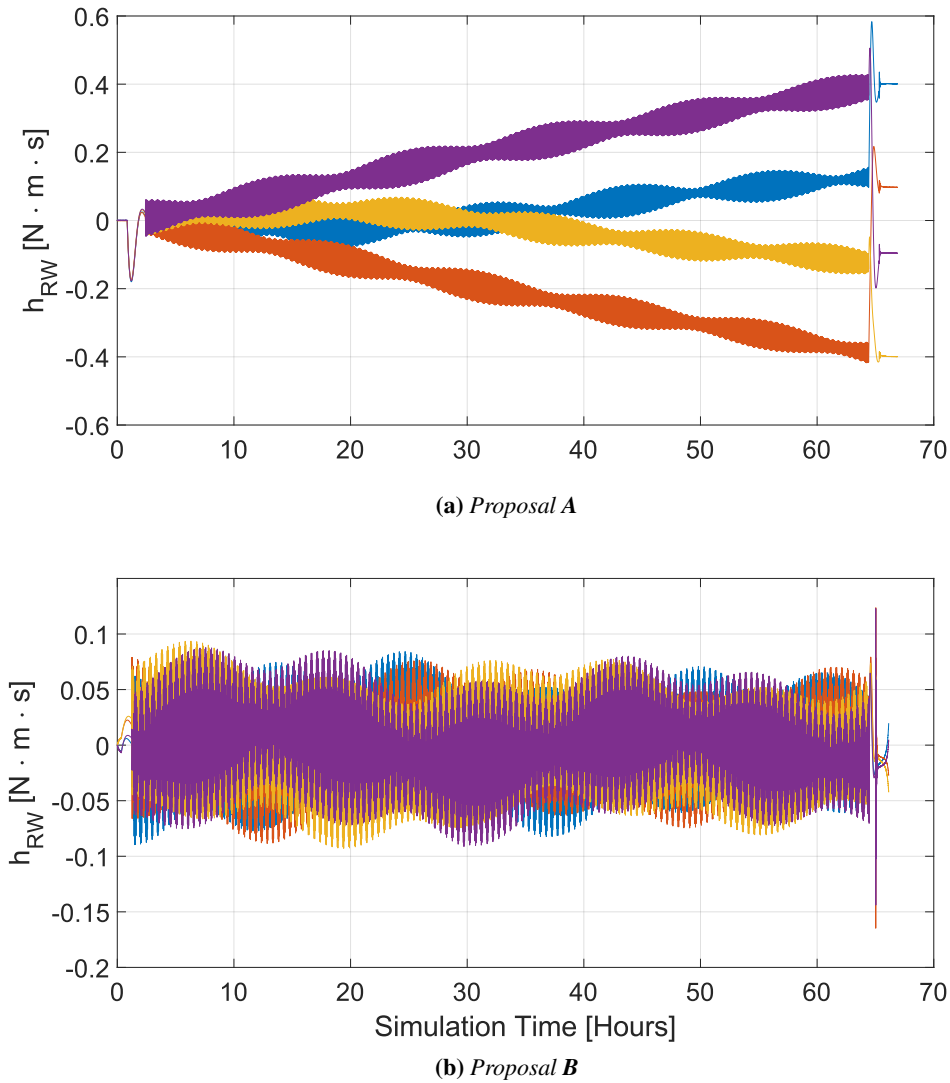
The results (Fig. 3.4) clearly show different trends between the two solutions: the *Modified Nadir Pointing* exhibits an auto-compensation trend of the momentum stored in each wheel, expectable since it is a typical feature of nadir pointing solutions; on the other end, the *Permanent Earth Visibility* approach exhibits a diverging trend (in the timeframe of an orbital period) which is expected to ask for much more frequent desaturation maneuvers.

These kinds of plots were used to reasonably and conservatively estimate the expected frequency of desaturation maneuvers in both cases imagining adopting for both cases the same reasonable class of [RW](#) ( $4N \cdot m \cdot s$  storables angular momentum class) and thrusters ( $5N$  max thrust class):

- **Proposal A:** hundreds of desaturation maneuvers asking for 6 Kg of propellant (100% margined)
- **Proposal B:** dozens of desaturation maneuvers asking for 0.5 Kg of propellant (100% margined)



**Figure 3.4:** Example of the accumulation of angular momentum in the RW



### 3.2.6 Trade-off: conclusions

The analysis primarily aimed at demonstrating the feasibility of the proposed architectures and algorithms. The simulations showed the theoretical possibility of ensuring the desired accuracies, even if much more refined models capable of coupling this kind of analysis with the thermal and structural ones would be fundamental to assess the fulfillment of the highly demanding scientific pointing budget.

Regarding the conclusion of the trade-off, the team chose to adopt the Proposal A: even if the discussion showed this solution to be worse in terms of potential risk regarding the TCS control, in the management of the SADA and to be the most propellant consuming, the possibility to highly relax the telecom scheduling and the avoidance of equipping a robotic arm convinced the team to adopt this strategy.

# Chapter 4 Propulsion Subsystem

This section analyses the [s/c](#) Propulsion Subsystem (**PS**), which is responsible for propelling the [s/c](#) through various mission phases, including orbit insertion, [SK](#), and attitude control. The reliability and efficiency of this system are crucial for optimal performance throughout the mission.

In the subsequent analysis, potential trade-offs among propulsion system options for both primary and secondary propulsion will be examined, considering factors such as performance, efficiency, reliability, and mass constraints. Ultimately, the chosen solution, a dual-mode architecture, will be presented, along with the corresponding sizing considerations tailored specifically for the LUMINOUS mission.

As will be illustrated later, the propulsion system features a dual-mode architecture, incorporating both bipropellant and monopropellant thrusters.

## 4.1 Trade-off analysis

This section will discuss the factors that were considered during the initial design phase of the propulsion subsystem, which ultimately influenced the final decisions regarding the technology selection of primary and secondary propulsion. These choices have been driven by the overall goal of adapting the propulsion system to best suit the mission's objectives, grounded in an examination of the factors that will be explored in detail now.

- **Impulsivity of the maneuvers:** the propulsion system's capacity for high thrust maneuvers is a critical consideration, as it directly influences the agility and responsiveness of the [s/c](#) during various mission phases, and especially during the insertion in the lunar orbit.
- **Power consumption:** evaluating the energy requirements of the propulsion system is essential to ensure that it aligns with the available power resources. Solutions with lower consumption that meet mission objectives should take priority, ensuring efficient power allocation for other mission-critical functions.
- **Storability:** the selection of storable propellants that exhibit long-term durability and stability is crucial. These propellants should maintain their performance and stability over extended periods, ensuring reliability and effectiveness throughout the mission's lifespan.
- **Propellant mass:** analyzing the mass of the propellant carried by [s/c](#) is vital, as it influences overall mass considerations and mission duration. The priority lies in selecting more efficient systems that can minimize the quantity of propellant mass required for the maneuvers.
- **Heritage:** drawing on past experiences and using proven technologies can enhance reliability while reducing risks associated with the propulsion system. By evaluating heritage, a knowledge base can be established, and successful implementations of previous missions can be leveraged effectively.
- **Complexity of the system:** evaluating the complexity of the propulsion system is essential for assessing potential points of failure and the overall robustness of the system in the context of the mission's objectives.
- **Potential for mission extension:** given certain configurations of the propulsion subsystem, there is a possibility to extend the mission duration beyond the nominal 6 years from a propulsion viewpoint. This extension becomes feasible if a portion of the propellant allocated conservatively for specific maneuvers is saved.

The following analysis examines how the factors presented before guided the selection process for primary and secondary propulsion systems. To gain a general understanding of the possible propulsion technologies that meet these criteria, the main features of these systems are presented in [Table 4.1](#). The aim is to provide a clear and rational explanation for these crucial decisions.



Option	Features
Electric Propulsion	<ul style="list-style-type: none"><li>- <b>Efficient use of propellant:</b> utilizes ionized gas for thrust generation, maximizing propellant efficiency</li><li>- <b>Very high specific impulse (Isp):</b> achieves superior efficiency compared to chemical propulsion</li><li>- <b>Limited thrust capability:</b> suitable for gradual maneuvers rather than rapid changes</li><li>- <b>Reduced mass requirements:</b> requires less propellant due to the high specific impulse, leading to decreased launch mass</li><li>- <b>Very high power consumption:</b> requires significant electrical power for operation</li><li>- <b>Complex integration:</b> requires careful integration with <a href="#">s/c</a> systems to ensure optimal performance</li><li>- <b>Low heritage:</b> represents a newer technology compared to traditional chemical propulsion methods</li></ul>
Chemical Bi-propellant	<ul style="list-style-type: none"><li>- <b>High thrust capability:</b> provides higher thrust levels compared to electric propulsion, enabling impulsive maneuvers</li><li>- <b>High specific impulse (Isp):</b> offers a balance between efficiency and thrust, with specific impulse values higher than other chemical solutions</li><li>- <b>Moderate mass requirements:</b> requires a moderate amount of propellant, lower than other chemical solutions</li><li>- <b>Low power consumption:</b> consumes low levels of power compared to electric propulsion, typically for control and ignition systems</li><li>- <b>Simplified integration:</b> generally easy to integrate into <a href="#">s/c</a> systems</li><li>- <b>Established heritage:</b> represents a well-established technology with a proven track record in satellite propulsion, offering reliability and predictability for mission planners</li></ul>
Chemical Monopropellant	<ul style="list-style-type: none"><li>- <b>Single propellant:</b> utilizes only one type of propellant, simplifying storage and handling requirements</li><li>- <b>Moderate thrust capability:</b> provides moderate thrust levels suitable for orbit adjustments and attitude control</li><li>- <b>Moderate specific impulse (Isp):</b> offers a balance between efficiency and simplicity, with specific impulse values typically lower than bipropellant systems</li><li>- <b>High mass requirements:</b> requires more propellant compared to bipropellant systems due to the lower specific impulse</li><li>- <b>Low power consumption:</b> consumes relatively low levels of power, mainly for control and ignition systems</li><li>- <b>Simplified integration:</b> generally easy to integrate into spacecraft systems</li><li>- <b>Established heritage:</b> represents a well-established technology</li></ul>
Chemical Cold Gas	<ul style="list-style-type: none"><li>- <b>Simple propulsion mechanism:</b> utilizes compressed gas, typically nitrogen, as propellant expelled through a nozzle to generate thrust</li><li>- <b>Low thrust capability:</b> provides relatively low thrust levels suitable for attitude control and small orbit adjustments</li><li>- <b>Low specific impulse (Isp):</b> offers lower efficiency compared to other propulsion systems, with specific impulse values lower than monopropellants or bipropellants</li><li>- <b>Very low power consumption:</b> consumes minimal power, mainly for control and valve systems</li><li>- <b>Simple integration:</b> easiest propulsion system to integrate into <a href="#">s/c</a> systems</li><li>- <b>Established heritage:</b> represents one of the earliest and most widely used forms of propulsion for attitude control in satellites, offering reliability and simplicity</li></ul>

**Table 4.1:** Main characteristics of various propulsion system technologies [33]



### 4.1.1 Primary propulsion

In evaluating primary propulsion options, both electric and chemical bi-propellant systems were considered. An electrical solution was initially taken into consideration. Due to the very high specific impulse, this technology is the new frontier, allowing the reduction of propellant mass. However, the greatest limitation of electrical motors for primary propulsion is that, due to the very low level of the maximum achievable thrust, it is not possible to supply impulsive maneuvers, resulting in an extended [TOF](#). Given the choice of the launcher, capable of reaching a Lunar Transfer Orbit ([LTO](#)), a crucial impulsive maneuver is required for the transition to a High Lunar Orbit ([HLO](#)). Only a bi-propellant system can ensure this maneuver, making it the most reasonable choice for the primary propulsion of the mission.

### 4.1.2 Secondary propulsion

For the secondary propulsion, several potential architectures were considered. Among these, the potential solutions included electric propulsion, cold gas systems, monopropellant, and bipropellant thrusters.

Electric propulsion was ruled out also for secondary propulsion due to various reasons. The primary concerns included the potential oversizing of the [EPS](#), introducing unnecessary complexity, and impacting [s/c](#) efficiency and weight. Additionally, challenges related to power management during eclipse periods and frequent eclipses posed significant issues for both primary and secondary energy sources. The need to compensate for primary source issues placed elevated demands on the secondary source during eclipse cycles, risking to compromise of crucial scientific activities. Furthermore, the low heritage observed for a Chemical-Electric hybrid engine raised doubts about its reliability and performance, playing a decisive role in the decision-making process.

Cold gas monopropellant solution for secondary propulsion was also discarded due to its very low specific impulse (Isp), resulting in an excessively high mass of propellant required. The substantial  $\Delta v$  requirements for our specific mission would necessitate an impractical and disproportionately large quantity of propellant. This not only increases logistical challenges but also escalates the mass of the entire propulsion system, adversely affecting overall efficiency and mission feasibility.

From the considerations thus far, the remaining viable options for secondary propulsion are monopropellants and bipropellants. Subsequently, a detailed exploration will determine the specific choice for various phases associated with secondary propulsion.

#### Attitude control

Monopropellant thrusters emerge as the optimal choice for attitude control and desaturation of the reaction wheels due to their simplicity and efficiency in providing controlled bursts of thrust. Their single-component nature simplifies the propulsion system, making them well-suited for precise adjustments in [s/c](#) orientation. The ease of maneuverability and straightforward combustion process of monopropellants make them particularly effective for fine-tuning attitude control during various mission phases.

#### Station keeping

Regarding station keeping, bipropellant thrusters were selected. Even if this decision introduces added complexity to the overall system, the significant advantage of this choice lies in the fact that, given the high  $\Delta V$  requirements for these maneuvers throughout the 6-year mission, utilizing bipropellant thrusters with a specific impulse exceeding 300 seconds allows to substantially reduce the total propellant mass required. Moreover, by using the same propellants as the primary thruster, there is a possibility to extend the mission lifetime beyond the planned 6 years, considering the conservative  $\Delta V$  selected for primary propulsion maneuvers. This can be achieved by using the surplus propellant saved during these maneuvers.

## 4.2 Architecture

The propulsion system features a dual-mode architecture, with bipropellant thrusters for primary propulsion and [SK](#), and monopropellant thrusters dedicated to attitude control. Specifically, the configuration includes 8 monopropellant thrusters (each with a thrust of 4,5 N), 4 bipropellant thrusters (each generating 22 N of thrust), and a primary 450 N bipropellant thruster. In terms of propellant storage, the system incorporates four tanks: four designated for fuel (hydrazine), one



for oxidizer (MON), and one for pressurizing gas (helium). The helium tank adopts a spherical shape, while the others are cylindrical. This design ensures efficient internal space management, contributing to the overall effectiveness of the propulsion system.

The decision to incorporate four hydrazine tanks is driven by the need for better weight distribution and optimization of the space utilization within the *s/c*, with the oxidizer tank positioned at the center and the fuel tanks on the four sides. Each tank and thruster is equipped with temperature sensors for monitoring. The feeding lines feature filters and various types of valves to ensure the opening and closing of lines, incorporating redundancy into the system for enhanced reliability.

In [Figure 4.1](#), it is possible to observe the propulsion system's architecture, providing a clearer depiction of the aforementioned components.

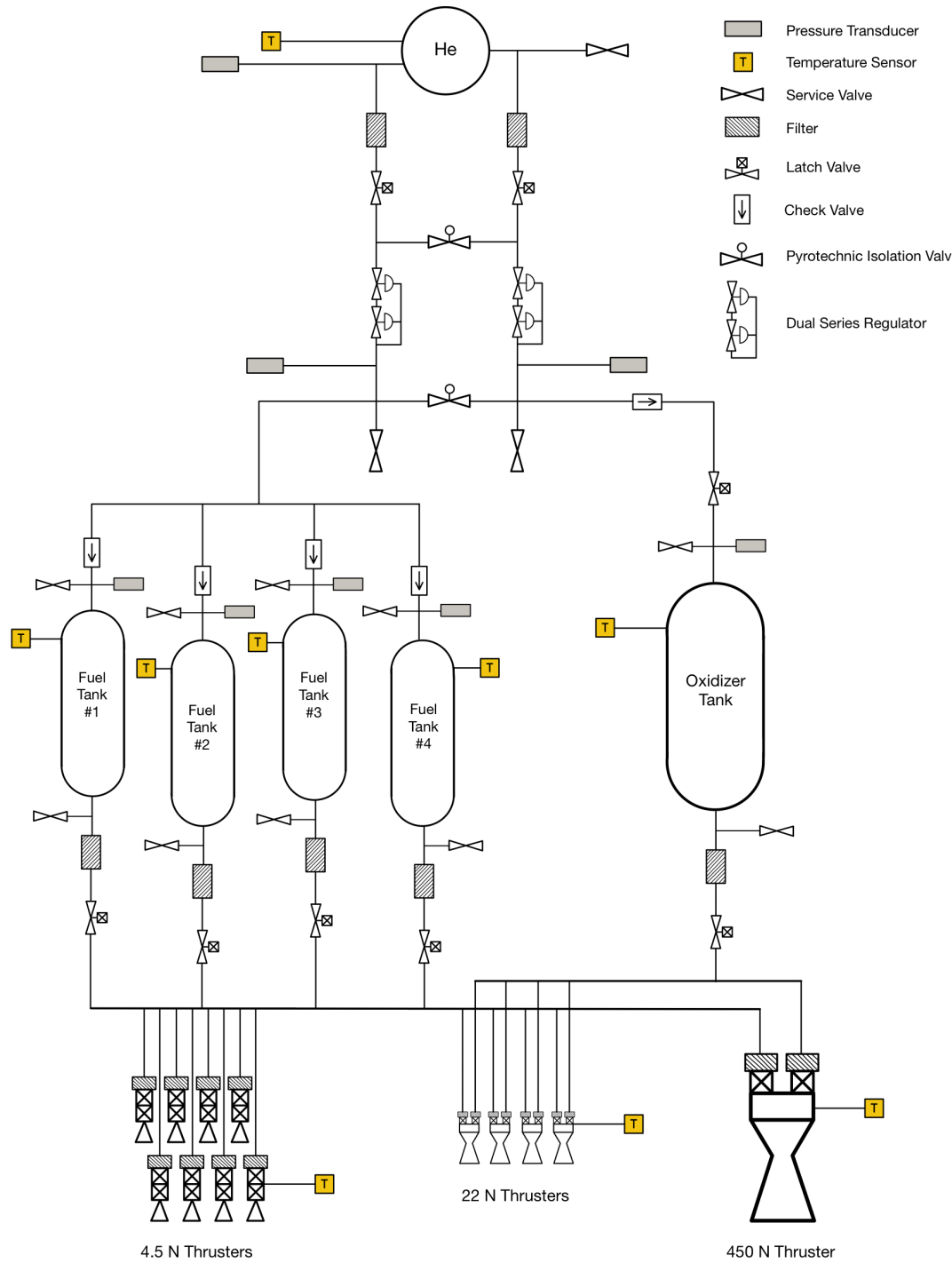


**Figure 4.1:** Propulsion system architecture



Now, a detailed examination is presented for the selected primary and secondary thrusters, tanks, and pressurization system, along with their respective characteristics. This exploration will provide insights into the specific features and capabilities, offering a comprehensive understanding of the propulsion system's functionality.

### 4.2.1 Thrust and engine selection

Given the selection of propulsion technologies for primary and secondary propulsion, it was necessary to propose specific thrusters for each case. The required thrust was determined by calculating the burning time for different maneuvers needed. This calculation aimed to confirm if the time taken for these maneuvers was short enough compared to the orbit period, allowing them to be approximated as impulsive. This was particularly important for station-keeping maneuvers. Considering these factors and the availability of thrusters on the market, specific engines were selected and proposed for each case. These thrusters will be now analyzed in detail.

#### Primary propulsion

The proposed bipropellant thruster for primary propulsion is the Leros 1c, with a list of key features in [Figure F.1](#). One of the main reasons why this thruster was chosen is related to his high heritage, having been successfully employed in various missions such as Jupiter Juno, Mercury Messenger, and Mars Global Surveyor.

#### Secondary propulsion - Station keeping

For [SK](#) maneuvers, the chosen solution involves the DST-11H. The major reason is that it utilizes the same propellants, Hydrazine/MON, as the primary propulsion system. This commonality streamlines logistical considerations making it the most suitable for the mission. Moreover, the DST-11H has a higher specific impulse (310 s) compared to some alternative options shown in [Figure F.2](#), aligning with the mission's goal of minimizing overall propellant mass. It also presents a high heritage, having been successfully utilized in various missions that adds a layer of reliability and proven performance to our choice.

#### Secondary propulsion - Attitude control

For attitude control and the desaturation of the reaction wheels, the chosen solution involves the reliable MONARC-5 monopropellants, fed with Hydrazine. In [Figure F.3](#), the key characteristics of MONARC-5 and other monopropellant solutions within the same family (MONARC) can be observed.

### 4.2.2 Pressurization system

The [s/c](#) utilizes a pressure-regulated system for pressurization. This system maintains a consistent pressure within the propellant tanks to ensure optimal performance. Additionally, an extra dedicated tank is incorporated to store the pressurizing gas, which in this case is helium.

The choice of helium as the pressurizing gas is motivated by several factors. Helium is inert, meaning it does not react with the propellants or other components of the system, minimizing the risk of contamination or chemical reactions. It also has excellent thermal properties, remaining stable across a wide range of temperatures typically encountered in space environments. Moreover, helium's low atomic mass makes it efficient for pressurization, requiring less volume compared to other gases for the same pressure levels [34].

### 4.2.3 Tanks

As previously discussed, the [s/c](#) will feature five cylindrical tanks for propellant storage (4 for fuel and 1 for oxidizer), and one spherical tank dedicated to storing pressurizing helium gas.

The decision to use cylindrical tanks for propellant storage is driven by internal configuration requirements, since their elongated shape allows for optimal placement, maximizing available space while accommodating the required propellant volume.

The choice of a spherical tank for storing helium pressurant is based on the well-established advantages of spherical tanks for pressurization purposes. Spherical tanks are preferred for pressurants because of their superior structural properties,



especially for containing high pressures. In fact, the spherical shape ensures an even distribution of internal pressure across the tank's surface, enhancing structural integrity and minimizing stress concentration [35].

### Propellant management device (PMD)

As a propellant management device for the propellant tanks, the capillary vane tank has been selected. Utilizing capillary action within a network of vanes, this system effectively manages propellant distribution within the tank, ensuring consistent and reliable feed to the spacecraft's propulsion system in the absence of gravity [36].

## 4.3 Propulsion system sizing

In this section, a comprehensive analysis of the sizing requirements for both primary and secondary propulsion systems will be conducted. This analysis encompasses the determination of propellant quantities necessary for maneuvers, the pressurization system with helium mass required, as well as the parameters for fuel, oxidizer, and helium tanks.

### 4.3.1 Primary propulsion sizing

For the calculation of the propellant required for primary propulsion, two distinct maneuvers were considered: orbit insertion and disposal. For both, the calculation was based on the main thruster, the LEROS 1c Engine, which has a specific impulse of 324 seconds and an oxidizer-to-fuel ratio of 0,85. Additionally, following the ESA margin philosophy [37], a 2% margin was added to the calculated mass for propellant residuals and a 10% margin to the propellant volume contained in the tanks. Now, a detailed analysis will be conducted on the fuel and oxidizer quantities, as well as the volumes computed for the two maneuvers, taking into account the applied margins.

#### Orbit insertion

The orbit insertion maneuver is the initial propulsion maneuver performed by the *s/c* during the mission. It is an impulsive maneuver essential for entering the targeted HLO. To execute this maneuver, a highly conservative  $\Delta V$  of 735 m/s was considered. The *s/c* wet mass was taken as the sum of the dry mass and the masses of propellant required for subsequent maneuvers.

	Mass (Kg)	Density (Kg/dm <sup>3</sup> )	Volume (dm <sup>3</sup> )
<b>Fuel (Hydrazine)</b>	87,1 (+1,8)	1,004	88,5 (+8,9)
<b>Oxidizer (MON)</b>	74,1 (+1,5)	1,370	55,1 (+5,6)
<b>Wet mass</b>	620 Kg		

**Table 4.2:** Propellant masses and volumes computed values

#### Disposal

The disposal maneuver, on the other hand, is the final maneuver executed by the *s/c* before concluding the mission. In this case, as well, a highly conservative  $\Delta v$  of 525 m/s was considered to perform the maneuver, while the mass considered is equal to the *s/c* margined dry mass.

	Mass (Kg)	Density (Kg/dm <sup>3</sup> )	Volume (dm <sup>3</sup> )
<b>Fuel (Hydrazine)</b>	39,2 (+0,8)	1,004	39,8 (+4,0)
<b>Oxidizer (MON)</b>	33,3 (+0,7)	1,370	24,8 (+2,5)
<b>Dry mass</b>	404 Kg		

**Table 4.3:** Propellant masses and volumes computed values



### 4.3.2 Secondary propulsion sizing

The central phase of the mission involves [SK](#) and attitude control maneuvers that last for at least 6 years.

For calculating the propellant required for secondary propulsion, it is essential to consider two distinct categories: bipropellant thrusters dedicated to [SK](#) and monopropellants designated for attitude control. In this case, the same margins as those used for the primary propulsion have been applied, following the margin philosophy of ESA. Subsequently, detailed quantities of fuel and oxidizer, along with volumes calculated for the two maneuvers, with the additional margins applied, are presented.

#### Station keeping

The [SK](#) maneuvers represent a series of maneuvers conducted throughout the scientific phase of the mission, spanning at least 6 years. Propellant quantity calculations have been based on the bi-propellant thruster DST-11H. This thruster has an oxidizer-to-fuel ratio of 0,85 and a specific impulse of 310 seconds. Additionally, in this case, following the ESA margin philosophy [37], a 5% margin has been applied to the  $\Delta V$ , as it has been accurately calculated for orbit maintenance maneuvers over 6 years. The wet mass of the [s/c](#) results from the sum of the dry mass and the mass of propellant required for the disposal maneuver.

	Mass (Kg)	Density (Kg/dm <sup>3</sup> )	Volume (dm <sup>3</sup> )
<b>Fuel (Hydrazine)</b>	72,2 (+1,4)	1,004	73,3 (+7,3)
<b>Oxidizer (MON)</b>	61,3 (+1,2)	1,370	45,7 (+4,5)
$\Delta v$			709.8 m/s (+35,5)
<b>Wet mass</b>			481 Kg

**Table 4.4:** Propellant masses and volumes computed values

#### Attitude control

Regarding attitude control, the monopropellant thrusters serve the purpose of desaturating the angular momentum accumulated by the reaction wheels. According to the simulations of the [ADCS](#), the propellant mass required has been calculated using the performance of the MONARC-5 thruster, which has a specific impulse of 226 seconds. The amount of mass required is 6 kg and the volume required is 6.6 dm<sup>3</sup>, considering margins.

### 4.3.3 Total masses and volumes of propellant

In [Table 4.5](#), the total margined values calculated for fuel and oxidizer are presented, taking into account both the primary and secondary propulsion systems. These values will serve as key inputs for the subsequent sizing of the pressurization system and the determination of tank parameters.

	Mass (Kg)	Volume (dm <sup>3</sup> )
<b>Fuel</b>	208,4	228,4
<b>Oxidizer</b>	172,1	138,2
<b>Total</b>	380,5	366,6

**Table 4.5:** Total propellant masses and volumes

### 4.3.4 Pressurization system sizing

Regarding the regulated pressurization system with helium as the gaseous pressurant, the mass and volume of the gas needed can be computed based on the data provided in [Table 4.6](#).

$p_{tank,in}$  is the pressure level of the propellant tank, derived from the evaluation of the pressure cascade in order to guarantee a minimum inlet pressure of 1,3 MPa needed for the Leros 1c Engine ([Figure F.1](#)),  $p_{press,in}$  is the initial pressure level of the gas in its tank, and  $\gamma_{gas}$  is the heat capacity ratio.  $T_{tanks}$  represents the temperature of the propellant tanks, while  $T_{press}$



denotes the temperature at which the helium is stored. The low temperature of the pressurizing gas is due to the helium tank placement outside the spacecraft.

$T_{tanks}$ (K)	$T_{press}$ (K)	$p_{tank,in}$ (MPa)	$p_{press,in}$ (MPa)	$\gamma_{gas}$
293	60	1,76	$10 \cdot p_{tank,in}$	1,667

**Table 4.6:** Parameters for calculations of the pressurization system

Considering the temperature and pressure parameters associated with the pressurization system, the corresponding values for mass and volume are illustrated in Table 4.7. Following the ESA margin philosophy [37], a 20% margin was added to the calculated mass.

	Mass (Kg)	Volume (dm <sup>3</sup> )
<b>Helium</b>	1,96 (+0,39)	16,7

**Table 4.7:** Helium mass and volume computed values

### 4.3.5 Tank sizing

The sizing of the tanks is conducted by considering the previously calculated volumes of propellant and helium, with cylindrical shapes for the propellant tanks and a spherical shape for the helium tank. The tank shell is fabricated from solution-treated and aged 6Al-4V or 6Al-2Sn-2Zr-2Mo titanium alloy. In Table 4.8, the values of density ( $\rho$ ) and yield strength ( $\sigma$ ) of the Titanium alloy used to calculate the main parameters of the tanks are provided.

$\rho$ (Kg/m <sup>3</sup> )	$\sigma$ (MPa)
4507	950

**Table 4.8:** Density and yield strength of the 6Al-4V titanium alloy

Then, computed values of mass, radius, thickness, and height of the tanks for the propellants and the pressurizing gas are presented.

	Mass (Kg)	Radius (mm)	Thickness (mm)	Height (mm)
<b>Fuel</b>	0,55	155	0,29	550
<b>Oxidizer</b>	2,10	250	0,46	370
<b>Helium</b>	2,11	160	1,50	-

**Table 4.9:** Tank parameters computed values

# Chapter 5 TTMTTC

In this Section, the spacecraft's TTMTTC subsystem will be explained in detail. This part will explain all trade-offs between different choices, the regulations that should be satisfied, and the components selection. It should be noted that the process of creating the link budget or the antenna formulation is valid in different references [38] and will not be mentioned in this section.

To begin, the initial data constraints of the various subsystems, with a particular focus on Mission Analysis, influencing the TTMTTC design will be outlined in the first section. Subsequently, a trade-off analysis among different choices will be conducted. In the third step, the system's link budget will be computed. Finally, considering the link budget and the overall system architecture, an analysis will be performed to assess the impact of the TTMTTC subsystem on the other subsystems.

## 5.1 Input data from other subsystems

The most important initial data for the TTMTTC is the Data Volume in different phases of the mission. Based on the Payload data, the satellite shall send a 960 Mbit picture per orbit cycle. In line with the SoHo mission(which is the sample mission), the data volume is equal to 20 kbit for both House Keeping (HK) and Navigation data together. In the context of the SoHo mission's command mode, no specific value is defined. However, referring to [38], the maximum length for one line command data is 64 bits. In this report, 10 lines of command data will be considered. Table 5.1 displays the data volume associated with all links. It's crucial to emphasize that this data volume does not incorporate any encoding processes; it solely represents the raw data volume.

Link Name	Data Volume (bits)
Dump Mode	$960 \times 10^6$ (Maximum observation time is two hours)
HK and Navigation	$20 \times 10^3$
Command	640

**Table 5.1:** Data Volume summarized

Furthermore, aside from transmitting data during the phase around the moon, the satellite should also send data during the earlier stages of the transfer and while in the parking orbit around the Earth to ensure optimal subsystem performance. Additionally, the farthest relay satellite around the moon is the Lunar Gateway space station. This relay satellite would be utilized if considering using the relay satellite to transmit data from the satellite to the ground station in a non-direct manner. The satellite distance concerning the Earth and also the relay satellite in different phases is shown in the table 5.2.

Phase	rough Distance (m)
Parking orbit and phase of the launch	35000
Operation phase (Direct)	405696000
Lunar Gateway	70000000

**Table 5.2:** The distance between Rx and TX in different phases of the mission

## 5.2 Communication operations

As mentioned earlier, there are three types of data: Dump, HK and Navigation, and Command. For Dump data, the Scientific data is sent to the Ground station once in each period, allowing a maximum storage time of one period. To reduce dependence on relay stations, these data are sent directly to the ground. The Dump link is active only during the mission operation phase when the payload is operational. HS and Navigation data will be transmitted to the ground



station once during each period. This data encompasses attitude, orbit, time correlation, and spacecraft modes files. Additionally, during the phase trajectory (at the critical event), in parking orbit, and the disposal phase, this type of data will be transmitted to the ground station. For the same reasons as previously mentioned, the link architecture involves direct communication from space to Earth.

On the other hand, command data from the ground station is transmitted to space at times designated by the ground station. Due to the potential lack of direct access to the ground station, this data must be relayed to the satellite using the relay satellites introduced in the previous phase. The different link types, their communication operations, and their communications architecture are mentioned in the table below.

Link Name	Communication Operations	Communication architecture
Dump Mode	One time per each orbit	Space to Earth
HK and Navigation	One time per each orbit + critical moments	Space to Earth
Command	Real-time link	Earth to Space with Relay

**Table 5.3:** The different link types, their communication operations, and their communications architecture

## 5.3 Visibility windows

The visibility window denotes the time available for the satellite to transmit data to Earth or the relay satellite. For Dump data, assuming the satellite's semi-major axis equals 11 moon radii, the visibility time is estimated at a minimum of 18,000 seconds, which is relatively high. Given the typical data rate of 1 to 2 Mbps, the data duration is capped at a maximum of 8 minutes. The readily accessible data rate (2 Mbps) eliminates the need for high complexity or new technology in the TTMTC system. Regarding the HK data, given its relatively low volume, fixing the data rate to the specified value from the SoHo mission (1.3 kbps) results in a negligible time requirement compared to the Dump mode data.

However, when it comes to sending commands, the relay satellite (or satellites) should always be within reach of the main satellite. In this situation, using the Lunar Gateway seems like the best choice. Given the big collaboration for this project, the chance of it not launching on time is low. Plus, since this station is in Near-Rectilinear Halo Orbit (NRHO), it guarantees full access to the satellite, making it the relay system. The usual data rate for the Command system is somewhere between 1 to 1000 bps for the NASA Deep Space network. For this project, the chosen data rate is 100 bit/sec, aligning with the assumption in reference [38].

## 5.4 Sizing and Justification of the architecture

This section involves selecting or designing the Ground station, Frequencies, and other components of the architecture. These details will be used to calculate the spacecraft's link budget.

### 5.4.1 Groundstation

For this mission, two Ground station options can be considered: NASA's Deep Space Network and European Space Agency (ESA)'s Deep Space Network (known as ESTRACK). Due to the ESA ground station's greater accessibility and political ease, the team prefers using European space stations for this project. These ground stations are equipped for communication in the X-band. The European Space Agency's deep space station network comprises three distinct ground stations located in different parts of the Earth. These stations are strategically positioned to achieve global satellite coverage. The Etrack ground station's location is shown in the figure 5.1.

#### Frequency

The frequency for each link can be determined by taking into account the Ground station frequency and adhering to ITU regulations. According to the reference [39], the ESA deep station ground station network operates in the X-band with Tx frequencies of 7,145 MHz - 7,235 MHz and Rx frequencies of 8,400 MHz - 8,500 MHz. Additionally, in accordance with ITU regulations, the typical earth station receiver frequency in the X-band ranges between 8400 to 8450 MHz.([40] and ITU-R SA.364-6) Also, Based on the same reference, the typical earth station transmitter frequency in the X-band ranges between 7145 to 7190 MHz. In this mission, the downlink frequency is considered as 8450. On the other hand,



**Figure 5.1:** The locations of the Deep space ground station network of the [ESA](#) (Number 4, 5, and 6 of Blue column)

the frequency range of 2025 to 2110 MHz (forward) and 2200 to 2290 MHz (return) is specified for Inter-orbit links and low data rate (less than 6 Mb/s) requirements with wide-beam or omnidirectional antennas for users of Deep Relay Satellites. Additionally, these frequencies can be used for launch, early orbit, and contingency command and telemetry, as per ITU-R SA.1019-1. The point about early orbit and transfer is that the ESTRACK ground station is working at the same frequency in the S-band and it is possible to use the same ground station.

Based on the previous explanation, the frequencies to be used for each link are specified in the table below. As it is not feasible to send Housekeeping and Navigation data using X-band during the parking and transfer phases, alternative antennas and a direct link will be employed for Housekeeping and Navigation data in these phases.

Link	Frequency (MHz)
Dump	8450
<a href="#">HK</a> and Navigation in operation phase	8450
<a href="#">HK</a> and Navigation in Launch and Transfer phases	2245
Command Relay	2050

**Table 5.4:** The Frequency selection for different Links

### Data Modulation

Once again, the [ITU](#) regulations must be taken into consideration when choosing the optimal type of modulation for the links. Based On the [ITU](#) regulation, Near-Earth missions generally use Binary Phase Shift Keying ([BPSK](#)) for a single data channel or Quadrature Phase Shift Keying ([QPSK](#)) for two independent channels, and Gaussian Minimum Shift Keying ([GMSK](#)) or 8PSK for bandwidth-efficient transmissions. Hence, for this mission, [BPSK](#) is the optimal choice for the command link, while [QPSK](#) is the preferred option for the Dump and [HK](#) Navigation modes. Different modulation for each link is mentioned in table 5.5.

Link	Modulation
Dump	<a href="#">QPSK</a>
<a href="#">HK</a> and Navigation in operation phase	<a href="#">QPSK</a>
<a href="#">HK</a> and Navigation in Launch and Transfer phases	<a href="#">BPSK</a>
Command Relay	<a href="#">BPSK</a>

**Table 5.5:** The Modulation selection for different Links



## Coding Selection

Following [ITU](#) regulations, command encoding should be implemented to ensure sufficient false command rejection due to error bursts, fading, or spurious signals. In addition, the basic error correction code used by the space research service is a rate of 1/2.(Convolutional coding)[40] In this project, Convolutional Coding will be implemented solely for the command link because it is suggested by the [ITU](#) and also it is very easy from an implementation point of view. For the other links, it is feasible to transmit data without implementing coding, relying on reducing the Bit Error Rate ([BER](#)) instead.

### 5.4.2 On-Board architecture

This section will identify parameters associated with the amplifier and antenna. These parameters encompass the antenna and amplifier types, their mass and size, as well as their efficiency.

#### Amplifier Selection

As mentioned before, the type of amplifier depends on how much power is coming in. If it's more than 10 W, the Travelling Wave Tube Amplifier ([TWTA](#)) is preferable since more efficient. Instead, if it's less than 10 W, the solid-state amplifier becomes better since lighter. The value of the power depends on the link budget calculation. Because the Dump data rate (which directly affects the power) is significantly higher than that of the [HK](#) and Navigation data, the [TWTA](#) is the preferred choice for this link. Conversely, given the low data volume and data rate for the [HK](#) and Navigation link, the Solid-State amplifier is the optimal option. Certainly, these are preliminary estimates, and the ultimate selection will be determined through the calculation of the link budget.

#### Antenna Selection

Regarding antenna selection, the spacecraft will employ two distinct types: one for Dump, [HK](#), and Navigation during the operation phase, and another one for Command, [HK](#), and Navigation during parking and transfer orbits. For the former, given the considerable distance and high data rate, along with the ability to point towards the ground station, the parabolic reflector and Horn antenna stands out as the optimal choice. On the other hand, following [ITU](#) regulation (ITU-R SA.1414-2), to receive commands from the relay satellite, either an omnidirectional or a parabolic antenna (with a diameter less than 1.5 m) shall be employed.

#### Components Selection Vs Development

Four different components will be used in the communication subsystem for this mission: Antennas, Amplifiers, receivers, and Transmitters. It should be mentioned that, in most cases, the amplifier and the transmitter or receiver will be produced with each other. None of these components have complex technology and there are a lot of missions that use these types of components.

- **Antennas:** As mentioned earlier, two distinct antenna types will be employed, both characterized by straightforward technology and a multitude of TRL 9 products available for use. A highly favorable choice and our suggestion for high-rate antenna links is the Medium Gain antenna from the BepiColombo mission. This Horn Type antenna operates in the X-band at the same frequency as our mission. Notably, it is integrated into a robotic arm, presenting an advantageous option for our mission to utilize both the antenna and the robotic arm in conjunction.[41] For the S-band transceiver, our suggestion is a specific antenna known as the "S-Band [TTMTC](#) Antenna," manufactured by AnyWaves Company. This antenna boasts a 6 dB Gain and holds a TRL of 9. The antennas are shown in the figure 5.2.
- **Transmitter or Receiver:** In examining options for the S-band transmitter and receiver, our suggestion is the "NewSpace S-Band Transceivers." This transceiver fulfills all the requirements, including [BPSK](#) and [QPSK](#) modulation, data rate, etc. Furthermore, it is scheduled for space testing before 2027. Conversely, information about the BepiColombo X-band transmitter is currently unavailable. As there isn't advanced technology for the X-band transmitter, it can be designed and tested before 2027. It's worth noting that existing X-band transmitters on the market have lacked a flight heritage for six years.



**Figure 5.2:** Left: S-band antenna for Low Rate Data, right: X-band Bepicolombo antenna

## 5.5 ITU Regulations

As discussed in earlier sections, compliance to [ITU](#) regulations was ensured in each segment. This same approach will be maintained in subsequent sections. The [ITU](#) document numbers utilized are:

1. ITU-R SA.364-6: Preferred frequencies and bandwidths for manned and unmanned near-Earth satellites of the space research service.
2. ITU-R SA.1019-1: Frequency bands and transmission directions for data relay satellite networks/systems.
3. ITU-R SA.1414-2: Characteristics of data relay satellite systems.

Additionally, reference [40] was consulted to find the [ITU](#) rules for deep space missions. It's important to note that adherence to these rules will be ensured in each section related to the topics, and here, we're simply listing the document numbers.

## 5.6 Link Budget

As mentioned before, all the relations related to the link budget were mentioned in the references and there is no need to mention them again. Based on the trade-off which was done before on the Ground station, frequency, type of antennas and etc, the link budget can be calculated. The link budget is shown in the table below.



LUMINOUS

Item	symbol	Unit	Dump Mode	Parking HK	Parking Command	Lunar HK mode	Lunar Command mode
Antenna type	-	-	Horn	Patch	Partch	Horn	Partch
Frequency	f	Hz	8,45E+09	2,25E+09	2,05E+09	8,45E+09	2,05E+09
Amplifier type	-	-	TWTA	Solid-State	-	Solid-State	-
Amplifier Power	P	P	10,5	0,1	-	0,03	-
Amlifier efficiency	-	-	1,00E-01	3,00E-02	-	3,00E-02	-
Transmitter power	P	Watt	1,05E+00	3,00E-03	-	9,00E-04	-
Transmitter power	P	dBW	0,211892991	-25,22878745	-	-30,45757491	-
Transmitter line , polariz loss	Li	dB	-2	-2	-	-2	-
Transmit antenna Gain	Gt	dB	2,09E+01	6,00E+00	-	2,09E+01	-
aperture efficiency	ea	-	0,55	-	-	0,55	-
Misalignment angle	e	degree	1	40	40	1	40
Diameter	D	m	0,3	-	-	0,35	-
Beam width	-	degree	1,26E+01	4,50E+01	4,50E+01	1,26E+01	4,50E+01
Misalignment losses	Lmis	dB	7,56E-02	9,48E+00	9,48E+00	7,56E-02	9,48E+00
Equiv. Isentropic Radiated power	EIRP	dBW	1,91E+01	-21,22878745	41,9815	-11,55757491	41,9815
Propagation path length	S	m	405696000	41126000	41500000	405696000	70000000
Space loss	Ls	dB	-2,23E+02	-1,92E+02	-1,91E+02	-2,23E+02	-1,96E+02
Propagation and Polarization Loss	La	dB	-0,04	0	0	-0,04	0
Receive antenna Gain	Gr	dB	-	-	6	-	6
System Noise Temp	Ts	K	-	-	287	-	287
Gr-10 log Ts	-	G/T	50,1	37,5	-18,57881897	50,1	-18,57881897
Symbol Rate	R	Sym/s	1,00E+06	6,50E+02	1,00E+02	6,50E+02	1,00E+02
Eb/N0	Eb/N0	dB	1,46E+01	1,55E+01	3,15E+01	1,57E+01	2,69E+01
Carrier-to-noise Density Ratio	C/N0	dB-Hz	7,46E+01	4,36E+01	5,15E+01	4,39E+01	4,69E+01
Bit Error Rate	BER	-	1,00E-05	1,00E-06	1,00E-06	1,00E-06	1,00E-06
Required Eb/N0	Req Eb/N0	dB-Hz	9,5	10,5	10,5	10,5	10,5
Implement Loss	-	dB	-2	-2	-2	-2	-2
Margin	-	dB	3,06E+00	3,00E+00	1,90E+01	3,25E+00	1,44E+01

Table 5.6: The link budget calculation for different links



### 5.6.1 Results of the link margin

As seen in the link budget, the link margin is over 3 dB, which satisfies the safety standards per ITU regulations [42]. The ample link margin for the downlinks is due to the high Effective Isotropic Radiated Power (E.i.r.p) of the ground station and relay satellite. The choice of the BER value follows ITU regulations [40]. The effects of the power and pointing will be discussed in the next sections.

## 5.7 Effects of the TTMTTC Subsystem on the other Subsystems

In this section, the impact, input, and constraints of the TTMTTC on the other subsystems will be elucidated. Compliance with these conditions is essential in the other subsystems to ensure a robust link budget.

### 5.7.1 TTMTTC Mass budget

When considering the Mass budget for TTMTTC, three main components need attention: Antennas, amplifiers, and transmitter/receiver. The Mass of the amplifier is calculated in the Mass of the Transmitter/Transceiver. As for the antenna and transmitter, the Mass information for the Bepicolombo antenna isn't available in any documents. However, a similar spacecraft (Solar Orbiter) utilizes the same antenna gain and type. The total Mass of the Solar Orbiter's medium gain antenna with Antenna Pointing Mechanism Electronic (APME) is 25 kg.[43] Considering the limited data available, it is recommended to include a 20% margin for this antenna, as indicated in the slides. Regarding the S-band antenna and S-band Transceiver, their Mass is specified in the data sheets, and a modest 5% margin will be applied for off-the-shelf products without modifications. The summary of the Mass budget related to the TTMTTC subsystem is shown in Table 5.7.

Component	Mass Without Margin (kg)	Margin	Mass With Margin (kg)
S-band Transciver	0,3	5%	0,315
S-band antenna	0,136	5%	0,1428
X-band transmitter and antenna	25	20%	30
Total Mass	<b>25.436</b>	-	<b>30.4578</b>

Table 5.7: Mass Budget for the System

### 5.7.2 TTMTTC Thermal Budget

As discussed earlier, the thermal effects on the telecommunication subsystem involve two main factors. Firstly, there's the designated temperature range for the subsystem's operation, and secondly, the internally produced heat. The heat generated by the TTMTTC subsystem is computed using the amplifier efficiency and is presented in the Table 5.8.

Mode	Unit	Dump Mode	Parking HK	Lunar HK
Energy	W.hr	1,4	0,00042735	0,000128205
Efficiency of the amplifier	-	0,1	0,03	0,03
Heat energy	W.hr	<b>12,6</b>	<b>0,013817664</b>	<b>0,004145299</b>

Table 5.8: TTMTTC Thermal Budget

On the contrary, each component comes with its specific thermal operational limits. The S-band transceiver and antenna boundaries can be easily obtained from the datasheet. However, in the case of the x-band transmitter, deriving its boundaries can be achieved by referencing other components operating at the same frequency, considering its current development phase. The EnduroSat X-band Transmitter serves as a similar component, and its data can be found in reference [44]. As for the X-band antenna, the temperature limits can be located in [41]. The components' thermal boundaries and their TRL were mentioned in the Table 5.9. It's important to note that these numbers are without margins and in the Thermal Control Subsystem, the margins shall be applied based on the Margin type.



Component	Min Temp (C)	Max Temp (C)	Margin Type
S-band Transceiver	-20	60	COTS
S-band antenna	-120	120	COTS
X-band transmitter	-30	70	COTS with Modification
X-band antenna	-30	150	COTS with Modification
Final Temp	<b>-20</b>	<b>60</b>	-

Table 5.9: TTMTTC Thermal Boundaries

### 5.7.3 TTMTTC power Budget

The required power for the TTMTTC subsystem was computed using the link budget. Additionally, the time needed to transmit the data is derived from the visibility data volume and the data rate. With this information and taking into account the efficiency of the TTMTTC explained in the previous phase, one can calculate the energy and total power for each communication mode. This data is shown in Table 5.7.3.

### 5.7.4 TTMTTC's effect on the OBDH

The On-Board Data Handling (OBDH) system must have sufficient storage capacity to store data before transmitting it to Earth. Given that the data transmission occurs within one orbit, the OBDH should store data for a single observation mode. The payload data volume for each operational orbit is fixed at 960 Mbit for the maximum observation time (2 hours). Therefore, the storage capacity must be at least 960 Mbit dedicated solely to payload data. As the data volume for Command, HK, and Navigation data is significantly lower, this figure can be disregarded.

### 5.7.5 TTMTTC Pointing budget

Two antenna types are under consideration for this mission: HGA designated for the dump and HK in the mission operation mode and a Low Gain Antenna (LGA) intended for command and HK data in the parking orbit. The pointing accuracy for the dump mode must be less than 1 degree, as per the link budget calculation. Regarding the S-band antenna (or antennas), as discussed in the preceding section, the pointing requirement is below 40 degrees. To enhance efficiency and avoid pointing issues, it is advisable to use more than one antenna for transmitting this data type. Details regarding pointing, duration, and direction can be found in Table 5.11.

Mode	Unit	Dump Mode	Parking HK	Lunar HK	Command
Duration	Sec	480	15,38461538	15,38461538	13,6
Pointing Direction	-	Ground station	Ground station	Ground station	Relay Satellite
Accuracy	Degree	1	1	40	40

Table 5.11: TTMTTC Pointing Budget

# Chapter 6 Electric Power Subsystem

The aim of the [EPS](#) is to provide the required power to all loads on the [s/c](#) in every phase and mode of the mission, primarily. Nevertheless, it is up to the aforementioned subsystem to deal also with energy storage if needed, and power distribution chain efficiency, in particular when transient bus voltages appear. Remarkably, the [EPS](#) shall be capable of detecting failures within itself and actuate to prevent any subsystem ([s/s](#)) being damaged [45].

In this chapter, the preliminary sizing of the [EPS](#) for the LUMINOUS mission will be presented, with particular emphasis on the solutions trade-off and the rationale behind the final choices.

## 6.1 Power source

Granting the fulfillment of the instantaneous power request is the principal burden of the [EPS](#). Several solutions are readily available, but the number keeps growing, due to the push for the creation of high power- and energy-dense components for [s/c](#) miniaturization and CubeSats exploitation in the space domain, and for carbon-net transition in on-ground energy harvesting [46]. Such an effort is strongly multi-disciplinary since the evolution in employed materials, distribution networks, and [s/s](#) interfaces must be carried out at the same time and in a coherent way. Not surprisingly, [EPS](#) is in general regarded as the principal bottleneck for space technology advancement [47]. The figures of merit that shall be taken into account to perform a proper selection of the power source are the following:

- **Average and peak power request:** the [EPS](#) shall be capable of producing, store, and transmitting the proper amount of power at every moment of the mission. Critical (maximum expected power consumption), non-nominal (fault occurrence, safety mode), and End Of Life ([EOL](#)) conditions shall be considered and addressed as well for robust sizing, even at this level of mission design.
- **Orbit type, altitude, and inclination:** these figures are strongly driving the power source selection trade-off. Being LUMINOUS a Moon-orbiting mission, the exploitation of a nuclear power source is not as critical as it would be for an Earth-orbiting solution (nevertheless, it is affected by other problems that will be presented later on). Altitude and inclination play a significant role in eclipse duration and frequency, thus in the design of the secondary energy source if the system relies on Sun energy harvesting; moreover, solar array technology opens the trade-off consideration for the Sun-tracking strategy, which impacts basically any other [s/s](#).
- **Mission lifetime:** being the LUMINOUS mission required to have a minimum lifetime of 6 years - being a part of it spent in the solar maximum activity timespan-, degradation of the power source with respect to time becomes critical. An oversizing at Begin Of Life ([BOL](#)) might be necessary to grant the target performance at [EOL](#).

That said, previous experience and development risk strategy are fundamental to evaluating the relation between such figures of merit and the power source selection.

Expected lifetime [y]	Expected peak power request [kW]
>1	<1

**Table 6.1:** Power-timespan requirements for LUMINOUS mission

[Table 6.1](#) and [Figure 6.1](#) (taken from [45]) rule out the possibility of employing primary batteries and fuel cells, being such solutions tailored to launch vehicles and small, short-living Cubesats [45]. The trade-off analysis between photovoltaic power production and a Radioisotope Thermonuclear Generator ([RTG](#))-based solution is suggested to be carried out for the mission at hand.

Solar cells are the most obvious candidate as the power source, due to flight heritage, reliability, and the location of the mission, which enables efficient energy harvesting, being the Sun really close at 1 AU ca [45]. The photovoltaic power source is a fast-growing family. Being the LUMINOUS mission meant to be launched later than 2027, developments in the current state-of-the-art technologies shall be taken into account, such that technologies with an actual low Technology Readiness Level ([TRL](#)) can be expected to be flight-qualified by that date.

Nevertheless, all solar cell solutions are affected by common problems:

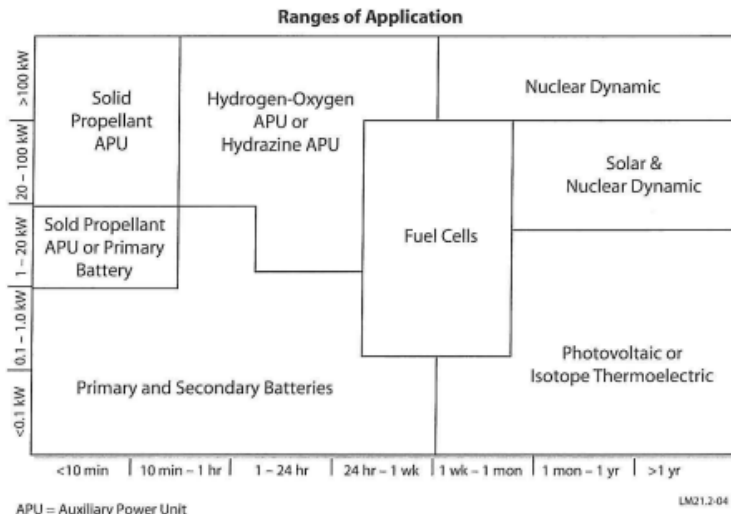


Figure 6.1: Power source vs lifetime

- **Inherent degradation:** when solar cells are manufactured into solar arrays to grant the required voltage and current output, the total efficiency comes out to be less than the one of the single cell, due to assembly, temperature, and shadowing effects. Inherent degradation can be mitigated via clever mounting and configuration of the solar array in the system, but it cannot be totally canceled out [45].
- **Cell degradation:** harsh environmental conditions result in the lowering of the power transformation efficiency of the single cell. This is directly related to the lifetime and the orbit of the system. A careful radiation hardness assessment shall be carried out to give an estimate of the predicted evolution of the performance.
- **Secondary power source:** solar arrays cannot produce power if sunlight is not hitting. Thus, for the entire eclipse duration, the system shall rely on another power source, typically a battery package. Obviously, this adds complexity, cost, and weight to the mission.

Additionally, solar power production is definitely affected by the other subsystems' requirements. In order to produce the maximum power output, the solar arrays (which are meant to be mounted on slender panels) should be constantly pointed to the Sun. This might not be always possible, since such pointing requirements might clash with other ones, e.g. payload or TTMTTC pointing. A solution to such criticality might come from having a cumbersome configuration or by employing a SADA, i.e. decoupling spacecraft rotation from arrays orientation, or enhancing power production for low Sun Aspect Angle (SAA) with solar concentrators, for instance.

SADA is considered a well-established technology. They have been employed in a wide range of missions, including Bepi-Colombo and the Parker Solar Probe (PSP). Solar concentrators have been investigated massively in recent years; remarkably, the Flexible Array Concentrator Technology (FACT), flown on the DART mission, represents the most interesting application of such technology [48]. Several other solutions have been proposed; an exhaustive resume is given in [33].

### 6.1.1 Solar cells: Si-based

The oldest kind of space-oriented cell type is the Si-based cell. Nowadays, they represent the cheapest and most reliable solution; however, they are affected by several drawbacks. First, most Si-based cells have a BOL efficiency of around 17%, which is the lowest available on the market of solar cells; then, the low specific power (0.38 W/g) basically eliminates their economical advantage, since a greater number of cells, with respect to competitors, is needed to meet the same power requirements [49]. Radiation resistance is also lower, and flexibility is comparable to the one of Multi-Junction (MJ) cells [45]. Production is extremely time-consuming [49].

### 6.1.2 Solar cells: multi-junction

Currently, the top-performance cells are MJ cells, which are typically made of an InGaP top layer, an InGaAs middle layer, and a Ge bottom layer (Triple-Junction (TJ) cells). The number of layers is variable; MJ cells with 5 layers (usually



referred to as Ultra-MJ cells) are expected to reach a top performance of 35% efficiency at **BOL** in the next 30 years [46]. MJ cells are more efficient than traditional Si-based cells due to their better exploitation of sunlight at all wavelengths; they are predicted to reach a hypothetical efficiency of 47% in laboratory conditions, compared to the estimated maximum efficiency of around 30% of Si-based ones [46] [49] [50]. Their superior temperature resistance can also be exploited via solar concentrators, which basically boosts the intensity of the striking light, with benefits from the efficiency viewpoint [46]. Careful production can lead to a maximum specific power of 3.8 W/g [49]. Moreover, they show superior resistance to radiation showers, which is definitely interesting for the mission at hand [45]. Many companies are producing MJ cells for spaceborne applications; in Europe AzurSpace and CESI are the most important actors in the market. It is no surprise this kind of cell has been employed extensively in the last 15 years for a very wide range of *s/c*.

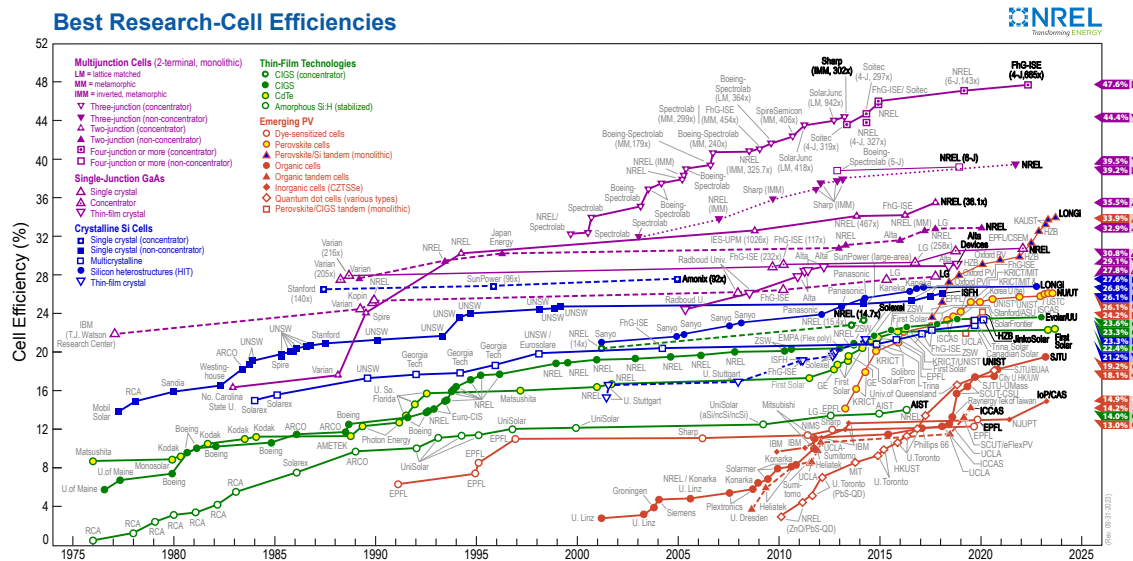


Figure 6.2: Overview of solar cells efficiency evolution

The principal drawback in the use of MJ solar cells is their low flexibility, which requires them to be mounted on a specific rigid surface such as one or multiple wings (if the *s/c* is not a spinner). Wings are not only expensive from the fabrication and installation viewpoint, but they also introduce several constraints from the configuration (they shall not be reached by thrusters plume and they shall not interfere with telecommunications, for instance), the **ADCS** (they are often imposing the maximum spin rate) and the **TCS** (cells are getting hot when illuminated, moreover this is a source of inefficiency for the cell performance) viewpoint; furthermore, wings need to be folded to fit in the launcher fairings almost always. Hence, a deployment mechanism (whose failure is not affordable) shall be designed to actuate once the *s/c* is stabilized after orbit insertion.

	Multijunction	Silicon	Cu(In,Ga)Se <sub>2</sub>	Perovskite
Efficiency	High	Medium	Medium	Medium
Lab-scale record	47.1%	26.1%	23.4%	25.5%
Commercially available for space	Up to 32%	~17%	Not available	Not available
Radiation hardness	High	High	Excellent	High
Specific power	Low – Medium 0.4–3.8 W g <sup>-1</sup>	Low 0.38 W g <sup>-1</sup>	Medium 3 W g <sup>-1</sup>	High 23 W g <sup>-1</sup>
Flexibility	Low	Low	High	High
Fabrication cost	High	High	Low	Low

Figure 6.3: Overview of principal solar cells technologies

### 6.1.3 Solar cells: thin cells

Another interesting technology belonging to the solar cells family is thin-film cell technology. Such cells are lighter, cheaper, and more flexible (they can be folded in a much more compact way than competitors, reducing mass, volume, and mechanical risk for the deployment of the wings) and reach 23 W/g in specific power (one order of magnitude greater



than **MJ** cells). They employ CIGS ( $Cu(In,Ga)Se_2$ ) or Perovskite [49]. Radiation hardness is comparable to the one of **MJ** cells.

The principal drawbacks of thin-film cells are the lower **BOL** efficiency (around 25%) and their current **TRL**, which is estimated to be around 4.

A comprehensive overview of the figures of merit of the different technologies is addressed in [Figure 6.3](#), taken from [49].

### 6.1.4 Nuclear power

**RTG** are employing the natural decay of a nuclear source to produce energy via the Seebeck effect, acting as a thermo-couple, or via the Stirling cycle. They have some advantages with respect to solar array technology, the most important being they do not need any secondary energy source since their power production is totally independent from the **SAA**. This, in turn, relaxes the requirements for other **s/s**, such as **ADCS** pointing, and cancels the risks linked to folding and deploying wings. They are also not affected by the radiation environment.

However, **RTG** faces several implementation problems. Such units require nuclear sources whose production process is complex, slow, and extremely expensive [51]. In the European space environment **RTG** are still not available. Remarkably, the development of in-house americium-241 power sources has been a priority in ESA agenda since 2009, and the current maturity of the technology allows the incorporation in mission studies from the mid-2020s onwards [52]. However, the projects embed 4 W and 10 W electric systems, with a recent interest in a 50 W power output unit. Such power levels are not compatible with the ones that are expected for the LUMINOUS mission; multiple units would be needed to meet the requirements both at **BOL** and **EOL**. Moreover, from a practical point of view, the few produced units per year (due to the complexity and length of the industrial assembly process) would be employed in applications for which photovoltaic power is unfeasible or too requiring, such as deep space exploration and landers. Another concern for nuclear power comes from the launcher selection: at the moment, European launchers do not offer the possibility to launch a nuclear-powered spacecraft; this is expected to change in the near future thanks to the development of the technology, but, as for now, that would translate in the forced choice of an American, Russian, Chinese or Indian launcher. Deploying a **RTG** mission in lunar orbit could be met with public skepticism due to lingering concerns surrounding nuclear technology itself.

## 6.2 Energy storage

Any mission relying on photovoltaic power production shall ensure the power requirements are met in eclipse conditions as well; in such cases, the employment of a secondary energy source is essential.

The most used technologies to cope with such tasks are secondary batteries, consisting of a series of connected cells. Secondary batteries are rechargeable: they can convert chemical energy into electric energy (discharge mode) and vice versa (charging mode). The voltage and current output depend on the configuration of the battery package. Many figures, such as power request, lifetime, number of cycles and Depth of Discharge (**DOD**) are driving the choice of the secondary battery [45]. An exhaustive comparison of the principal classes of secondary batteries is depicted in [Figure 6.4](#) [45].

The solution selection shall be addressed in the early phase of the project. The figures of merit driving the choice are:

- **Physical bulk:** battery packs are usually heavy and voluminous, and they must be packed inside the **s/c**. It is of paramount importance to select cells with high specific energy and energy density so that mass penalty at launch is minimized.
- **Mission profile:** altitude and eccentricity are driving the time the **s/c** is spending in eclipse, thus the duration of power request from secondary batteries. The nominal **DOD** shall be designed according to this, with a direct consequence on cell selection as well, since only a few types can tolerate high or total discharge. In general, higher **DOD** means a shorter lifespan [45]. Since batteries shall be charged as well, daylight time is also influencing the trade-off, as well as the choice for the charging strategy (Constant Voltage (**CV**), Constant Current (**CC**), sequential, etc.).
- **Usage:** secondary batteries can be employed also when the **s/c** is not in eclipse, for instance in the so-called trickle charging, or to relax power request from the primary source in peak power request moments.

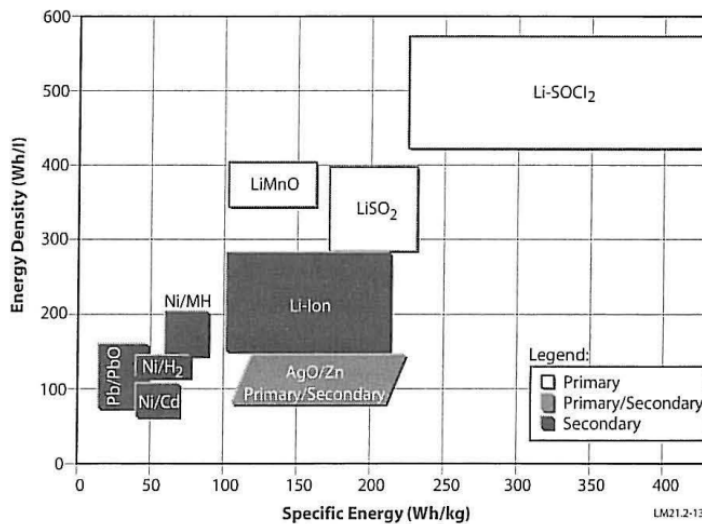


**Figure 6.4:** Specific energy vs specific density for batteries

### 6.2.1 Ni-Cd batteries

Ni-Cd batteries are one of the oldest kinds of secondary batteries employed in space [53]. They have a long heritage and reliability, but also low specific energy (30 Wh/kg) and energy density. Indeed, they were used before the 1980s, before the creation of Ni-H<sub>2</sub> batteries. Their typical temperature range is between 0 and 40°C; they do need reconditioning, but they can sustain trickle charge mode. Their self-discharge is 1%/day ca.

### 6.2.2 Ni-H<sub>2</sub> batteries

Ni-H<sub>2</sub> batteries double the energy density of Ni-Cd cells. The operative temperature range is increased to about -20°C to 30°C. As their predecessors, these cells need reconditioning and can tolerate trickle charging. They suffer from strong self-discharging (up to 10%/day) [45]. However, they can handle a high number of cycles at high DOD [53].

### 6.2.3 Li-ion batteries

The state-of-the-art technology for secondary batteries is represented by Li-ion batteries. They offer a 65% volume- and 50% mass-saving with respect to Ni-Cd or Ni-H<sub>2</sub> batteries, due to higher operating voltage, no reconditioning need, and lower self-discharge (0.3%/day) [45]. They can reach energy densities of 125 Wh/kg [45]. Li-ion cells are also less disturbing from the thermal viewpoint. The principal drawbacks linked to such technology are the limited operative temperature and the impossibility of sustaining trickle charging.

### 6.2.4 Li-S batteries

In the family of batteries, Li-S batteries are for sure the most promising technology, being theoretically capable of 5-time-bigger energy density with respect to current Li-ions. The biggest obstacles are high internal resistance, self-discharge, and rapid capacity fading on cycling. The actual TRL level of such technology is between 4 and 5 [54].

### 6.2.5 Supercapacitors

Supercapacitors are regarded as one of the most promising technologies for energy storage in space [55]. They provide less stringent thermal requirements (-40°C to 60°C), higher power density, higher lifetime, higher instantaneous discharge capability and faster recharging with respect to Li-ion batteries, at the cost of lower energy density [56]. The usage of Commercial off-the-shelf (COTS) components has been successfully tested; this could result in a fast market insertion for these components [56]. A Li-ion/supercapacitor hybrid system might grant the power requirements in conditions of peak power request with an overall lighter mass budget (Li-ion batteries are often oversized in power for high energy request cases, and vice versa [55]) and lower risk since the probability of one electrode to react unexpectedly would lower. How-



ever, the [TRL](#) of such technology is fairly low, having only just one demonstrator has been flown in a [LEO](#) [56].

## 6.3 Power Regulation and Control

The [EPS](#) shall grant any load meeting the required power (voltage and current intensity) at any time, thus it requires a strategy to deal with power storage and distribution effectively. Power conditioning is operated both on the source and on the distribution bus. Nominal steady-state voltage range, normal transients voltage, and voltage ripple are typically listed in each load's datasheet [45].

Direct Energy Transfer ([DET](#)) is the simplest power regulation strategy for the power source. It acts on the current output of the power source, keeping the voltage fixed, meaning it requires active power conditioning at load level. A major issue linked to [DET](#) is power lock-up, which is a run-out condition for which voltage keeps on decreasing leading to the ultimate failure of the system. Such a condition might onset at the exit of eclipse time, for instance, [45]. Moreover, [DET](#) makes the solar arrays work below the peak power point level when the driving voltage (typically one of the batteries) is low (like at the beginning of the recharge phase).

Peak Power Tracking ([PPT](#)) adds complexity to the system, with consequential efficiency reduction, although it decouples power source voltage and load voltage, acting on the output voltage [45].

The distribution bus can be fully regulated, semi-regulated, or unregulated [45]. The fully regulated one keeps the voltage of the bus constant, regardless of the [s/c](#) condition, and it is particularly suited for missions with a high number of cycles, since it optimizes the process of charge and discharge of batteries, at the expense of complexity. The unregulated bus, on the contrary, is suited for missions with a low number of cycles, such as geostationary satellites, and it is the simplest possible solution. The semi-regulated bus mixes the former strategies, by applying regulation during daylight and no regulation in eclipse.

## 6.4 Design rationale

[Table 6.2](#) resumes pros and cons for each solution, including the actual [TRL](#) (2024) and the expected one for the earliest mission departure (2027). Concerning this table, the following design choices have been made:

- **Primary power source:** the LUMINOUS mission is intended to use solar arrays for power harvesting. Nuclear power is discarded due to the low [TRL](#) in Europe. The kind of cells to be employed are [MJ](#) cells: it makes no sense to employ Si cells due to their low energy density, while thin cells are still in a too-premature development phase. The sizing is performed with currently available and flight-qualified units. The addition of solar concentrators is not investigated in the current work. The cells are intended to be mounted on two equal solar arrays in the pitch direction. This configuration is selected since it minimizes the risk of all instruments [FOV](#)'s obstruction and of plume impingement from thrusters, and contributes to locating the Center of Gravity ([CoG](#)) near the geometrical barycentre of the [s/c](#).
- **Solar arrays pointing:** each wing is equipped with a [SADA](#) to track the Sun along the minor inertia axis. This is driven by the choice to decouple solar arrays pointing and [s/c](#) attitude control. Indeed, the unit vector normal to the arrays lies in the same plane as the unit vectors normal to the payload and most instruments, thus different pointing requirements would clash. The [SADA](#) shall be capable of performing a complete rotation.
- **Energy storage:** since solar cells are employed, a secondary energy source is required to cope with eclipses and with all the phases of the mission in which solar power harvesting can not be granted. LUMINOUS mission is designed to employ Li-ion cells for this purpose. Ni-Cd and Ni-H<sub>2</sub> are discarded since their energy density is inferior to Li-ion and reconditioning is needed to preserve capacity. Li-S batteries are still a too premature technology to be selected. The inclusion of supercapacitors has been exhaustively investigated during the project study, but ultimately their usage has been discarded in the final design due to low flight heritage and the lack of isolated high power phases which would justify the presence of a power-dense component - Li-ion batteries are reasonably capable to deal with all mission requirements.



Problem	Solution	Pros	Cons	TRL (now)	TRL (2027)
Primary energy source	Solar arrays (Si cells)	Heritage Reliability	Weight Low flexibility Low energy density Low efficiency Pointing requirements	9	9
	Solar arrays (TJ cells)	Heritage Reliability High energy density High efficiency Radiation hardness	Low flexibility Pointing requirements	9	9
	Solar arrays (Ultra MJ cells)	High energy density Radiation hardness Superior efficiency	No heritage Pointing requirements	6	9
	Solar arrays (thin cells)	Superior energy density Radiation hardness Flexibility	Low efficiency No heritage Pointing requirements	4	7
	Solar arrays (MJ cells) + concentrators	High energy density Superior efficiency Reduced area	High temperature Low heritage Pointing requirements No European heritage	8	9
	Nuclear power	No pointing requirements No secondary source Radiation hardness	High temperatures Radiation shielding No possibility to use European launchers	5	6
	ADCS pointing	Easy control law Three axis pointing Minimal oversizing	Wheels saturation Fuel allocation Competition with other needs	9	9
Solar arrays pointing	Solar Array Drive Assembly	Decoupling from ADCS along principal axis Easy control law Fine pointing	Increased complexity Oversizing	9	9
Energy storage	Ni-Cd batteries	Heritage Reliability Moderate self-discharge	Low specific energy Narrow temperature range Reconditioning	9	9
	Ni-H <sub>2</sub> batteries	Good specific energy High number of cycles High DOD	Reconditioning High self-discharge	9	9
	Li-ion batteries	Superior specific energy Low self-discharge High number of cycles High DOD No reconditioning	No trickle mode	9	9
	Li-S batteries	Extremely high specific energy	No heritage New technology	4	6
	Supercapacitors	Wide temperature range High power density High lifetime Fast charging	Low heritage Low specific energy	7	8
	Direct Energy Transfer	Lighter Low complexity Long-lasting missions Efficiency	Sub-optimal power production Larger cables Lock-up prone Thermal control Dependence on power source	9	9
Power regulation	Peak Power Tracking	Optimal power production No lock-ups Independent from power source	Lower efficiency High complexity Noise production	9	9
Bus regulation	Fully regulated	Flexible No lock-up Battery independent from bus voltage Applicable to large satellites	Heavier More complex Losses	9	9
	Unregulated	Simple architecture High efficiency	Potential lock-up Complex load converters Direct dependence of distributed voltage on energy source	9	9



Problem	Solution	Pros	Cons	TRL (now)	TRL (2027)
Power distribution	Centralized	Easy to scale up/down Safety	Prone to single-point failures	9	9
	Distributed	Efficiency Flexible	Typical for unregulated bus Difficult to scale up	9	9
Battery charging	Parallel	Simple architecture Optimal charging No battery coupling Reliability	Higher degradation Short-lasting missions Low safety	9	9
	Individual	Simple Optimal for Li-ion	Longer charging Added complexity	9	9
	Constant voltage	Simple Optimal for Li-ion	Overcharging risk High current at low SOC Battery degradation Slow	9	9
Battery charging	Constant current	Simple Easy to retrieve SOC Optimal for Ni-Cd Fast	High current Problematic end-of-charge Overcharging risk	9	9
	Trickle charging	Simple Low current	Suited only for low DOD	9	9
	Constant current - constant voltage	Widely used for Li-ion Battery-model-independent Optimal charging	Complex Degradation if current is too high	9	9

Table 6.2: EPS trade-off

- **Power source regulation:** for the LUMINOUS mission DET technique for power source control is preferred, due to the high lifetime of the mission. Increase in the number of strings of the solar arrays is sufficient to counteract lock-up onset [45].
- **Bus regulation and power distribution:** the power bus voltage is taken to be 28 V, which is a standard value for low power s/c [45]. A fully regulated bus is intended to be employed. Such regulation grants flexibility, reduces the lock-up risk, and decouples battery design from power bus voltage. The power distribution chain is intended to be de-centralized, to reduce the risk of single-point failures.
- **Battery charging:** batteries will be charged individually. Such strategy is very well-suited for long-lasting missions and it is generally considered safer, since batteries are decoupled one from each other from the voltage and current viewpoint. The drawback is represented by augmented recharge time and complexity. The charging strategy is Constant Current Constant Voltage (CCCV), which is optimal and easy to implement for Li-ion batteries. This logic will be implemented in a Power Control & Distribution Unit (PCDU).

## 6.5 Results

Power budgets presented in Table 12.6 are employed in the sizing and selection of critical EPS components. The solar cells proposed in the final design are AzurSpace 3G30C Advanced cells. They are TJ cells characterized by BOL efficiency of 29.5% and surface of 30.18 cm<sup>2</sup> (which is aligned with the actual dimension trend for solar cells). The rationale behind their choice is their high radiation hardness (3% efficiency loss after 1e15 equivalent 1 Mev electron fluence), which translates into high efficiency at EOL, and their low thickness ( $80 \pm 20 \mu\text{m}$ ), which enables major mass saving (most equivalent cells are above 120  $\mu\text{m}$ ).

Cells in series	Cells in parallel	Total area [m <sup>2</sup> ]	Cells mass [kg]
13	70+2	2.82	1.41

Table 6.3: Solar arrays data

Please note in Table 6.3 that each wing has a redundant string to be compliant with ESA margins philosophy. Solar arrays are rotated thanks to Moog Type 1 SADA, one for each panel. The selected battery cells are EaglePicher LP32975. They are flight-proven components, employed in harsh applications

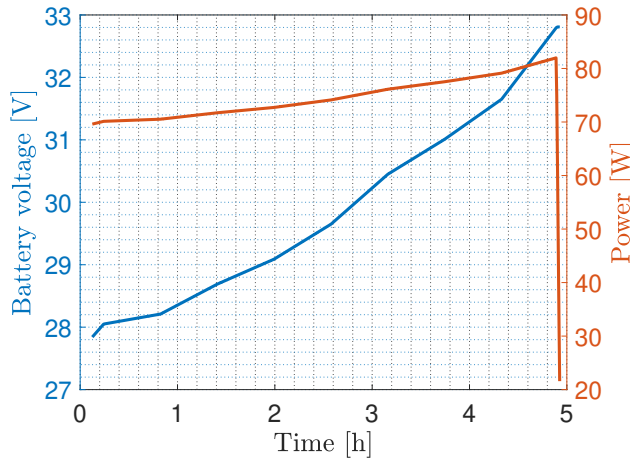


**Figure 6.5:** Voltage and power evolution during charging

such as Martian landers. They can sustain a great number of cycles at high DOD. Ultimately their selection is due to the fact their employment allows them to minimize the delta between the needed capacity (computed in the worst-case scenario, i.e. observation mode) and the actual capacity of the battery pack. They also offer the possibility of having single-string batteries, which is helpful from the cabling and overall complexity viewpoint. They can perfectly sustain mission needs, being capable of sustaining 100% DOD for more than 2000 cycles, which is more than twice the expected cycles for the LUMINOUS mission. Each one of the 4 batteries (the last being redundant) has 9 cells (being one cell redundant) and a maximum nominal DOD in observation mode of 82%.

Cells in series	Cells in parallel	Number of batteries	Maximum DOD [%]	Cells mass [kg]
8+1	1	3+1	82	16.74

**Table 6.4:** Batteries data

Each battery is charged individually with CCCV strategy in 4.80 h ca, for the battery at BOL and with a combined internal and assembly resistance of  $30\text{ m}\Omega$ . The charging simulation is performed in Simscape. The maximum power for a battery is fixed at 82 W, which is obtained for a constant current of 2.5 A during the first CC phase. Degradation of the battery can be modeled through a simple variable resistance, but no computation has been performed in this sense.

Magellan Aerospace PCDU is selected to manage power distribution between power source and loads. Two units, one being fully redundant, are mounted on the s/c.

Technical datasheets for the aforementioned components are reported in Appendix D.

# Chapter 7 Thermal Control Subsystem

The goal of the **TCS** is to keep all the **s/c** components and **s/s** within their temperature limits in each phase of the mission. The cold and hot temperature limits define a range in which each component, and more in general, the **s/c** shall operate. This chapter will present the preliminary sizing of **TCS** for the LUMINOUS mission, with an emphasis on the trade-off and choices made.

## 7.1 Problem Definition

The first step of the **TCS** sizing is the definition and identification of the temperature ranges and the heating environments in which the mission shall operate.

### 7.1.1 Temperature ranges

Two kinds of temperature limits can be distinguished: operational and survival. Operational limits are considered when the thermal environment with the component in operating conditions has to be evaluated, while survival limits refer to the temperatures the item shall withstand in non-operative phases. Only the operational limits have been considered to perform this preliminary sizing since they are the most stringent ones. The following **Table 7.1** shows the temperature required by the on-board components selected for this mission:

Subsystem	Component	Minimum Temperature [°C]	Maximum Temperature [°C]
<b>TMTC</b>	S-band Transceiver	-20	60
	X-band Transmitter	-30	70
<b>PL</b>	Coronograph	/	/
	Reaction wheel	-15	60
<b>ADCS</b>	Sun Sensor	-40	85
	Star Tracker	-55	30
<b>OBDH</b>	IMU	-10	60
	OBC	-28	70
<b>STR</b>	titanium	-100	1668
	aluminium	-100	660
<b>EPS</b>	SADA	/	/
	Battery	-20	60
<b>PS</b>	PCDU	-20	40
	MON Tanks and Lines	-10	50
<b>OVERALL</b>	Hydrazine Tanks and Lines	0	65
		0	30

**Table 7.1:** Overall temperature range

Note that the Star Trackers constraint the maximum temperature to 30°C, which is 10° lower than other **s/c** components. Considering that the star trackers are placed outside the structure and how critical they are, it is assumed that they are decoupled from the rest of the **s/c** and equipped with their own thermal control. As a consequence, the temperature range that the **TCS** shall guarantee is presented in the following **Table 7.2**:

Minimum Temperature	Maximum Temperature
0 °C	40 °C

**Table 7.2:** Overall temperature range

Note also that the Payload (**PL**) temperature range is not known but, for the purpose of this sizing, it is assumed as a sort of black box. For this reason, it has been considered that the **PL** temperatures shall be granted by an autonomous **TCS** specifically designed just for the **PL** by the instrument providers.



### 7.1.2 Heating environments

The [s/c](#) will encounter a series of different thermal environments. The most critical ones are collected in the following Figure 7.1:

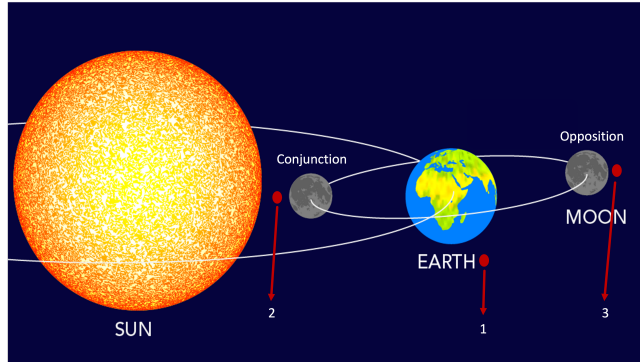


**Figure 7.1: Heating environments**

1. the [s/c](#)'s departure from Earth.
2. the [s/c](#) in between the Moon and the Sun, when the Moon is in conjunction.
3. the [s/c](#) in the ecliptic cone, when the Moon is in opposition.

## 7.2 Preliminary analysis: single-node approximation

Identifying the heat fluxes and the temperatures of the [s/c](#) in the three cases shown above is the second step needed to move on with the design of the [TCS](#). To do so, some assumptions and data collection concerning the [s/c](#) surface properties and the planets' ones are needed:

- The [s/c](#) is assumed to be covered entirely by a Multi-Layer Insulation ([MLI](#)) made with 20 layers of Single-Sided Aluminised Kapton ([SSAK](#)). [SSAK](#), so an Aluminised Kapton film, is selected due to its good absorvivity/emissivivity ratio and since it is a good first guess, due to its high flight heritage as [MLI](#) component. Other possible choices that were evaluated were Mylar and Beta Cloth, characterized respectively by a smaller temperature range and a lower resistance to Ultra Violet ([UV](#)) radiation [57]. 20 layers of [MLI](#) are used since this is in the standard 15-20 layers range, which is often used for reflectors films [57]. The emissivity is computed as:

$$\epsilon_{MLI} = \frac{1}{\frac{1}{\epsilon_{SSAK}} + \frac{1}{\epsilon_{SSAK}} - 1} \frac{1}{N+1} = 0.0012 \quad (7.1)$$

The emissivity of the [SSAK](#) is reported in section B.1

- The [s/c](#) is approximated as a sphere. The cross-sectional area is the one relevant to compute the heat received by the Sun, while the entire [s/c](#) area is used for albedo and IR heat.
- The internal power dissipation is retrieved by the power budgets (section 12.2), considering the power required by 3 particular modes:
  1. Deployment Mode for the Earth Departure
  2. Charging Mode for the conjunction
  3. Principal Science Mode for opposition

These three modes are selected following a conservative approach, since they are the most demanding, power-wise, in the three thermal environments described before in subsection 7.1.2. The dissipated power is given only for certain components (like the [PCDU](#)). For the other [s/c](#) components, the power required by each item in each considered mode has been multiplied by a thermal conversion efficiency to obtain the internal power dissipation. This efficiency is considered equal to 50%, which is a conservative assumption, for almost all the components, apart from Reaction Wheel Unit ([RWU](#)), for which a 30% efficiency has been used [58].



Exploiting the data collected in [section B.1](#) and the equations in [section B.2](#), it is possible to identify the two most critical conditions for the TCS design, which happen respectively at the Earth Departure and in the Moon Eclipse, as shown in the following [Table 7.3](#).

	Earth departure	Conjunction	Opposition
$Q_{\text{sun}}[W]$	482.45	484.94	0
$Q_{\text{albedo}}[W]$	227.58	0.0043	0
$Q_{\text{IR}}[W]$	1472	0.4176	0.0071
$Q_{\text{internal}}[W]$	218.19	160.1	229.65
$Q_{\text{tot}}[W]$	2400	645.47	229.66

**Table 7.3:** Most critical conditions for TCS

Exploiting the formulas collected in [section B.4](#) for the Earth Departure and the Moon eclipse cases it results that radiators and louvers are needed, while heaters can be avoided. The area for radiators and louvers is shown in the following [Table 7.4](#):

Radiators	Louvers
$4.83m^2$	$3.86m^2$

**Table 7.4:** Single-node analysis results

Please note the standard  $15^\circ\text{C}$  margin is applied to the computed temperatures.

### 7.3 Refined analysis: multi-node analysis and thermal network

Verifying, checking, and improving the design proposed before is a must and has been done by developing a thermal network, shown in the following [Figure 7.2](#):

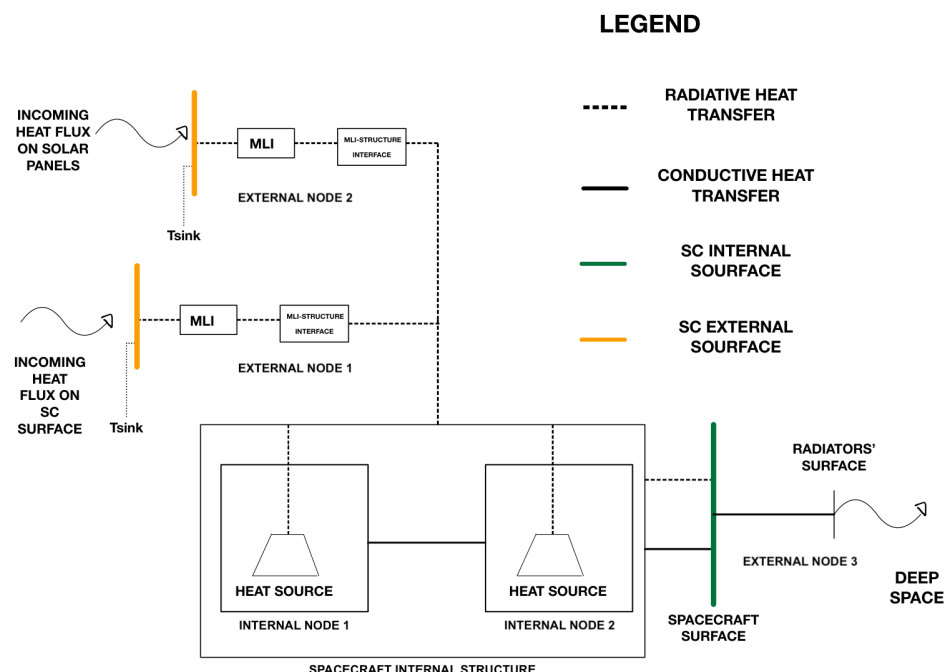


**Figure 7.2:** Thermal Network



### 7.3.1 Thermal Network Description

The network is made of four external nodes, which allow to couple the space environment with the inside of the [s/c](#), and two internal nodes, which resemble the layout of components inside the [s/c](#):

- The external node 1 receives all the heat incoming on the [s/c](#) external surface and transfers it through the [MLI](#) to the internal aluminum surface. It has been assumed the node surface is the cross-sectional area of the [s/c](#).
- The solar panel nodes receive only the incoming solar heat flux and, due to the temperature the panels have, radiate heat towards the external node 2 surface. This node's area is equal to the surface of solar panels and its temperature range is -100°C - +100°C.
- The external node 2 receives the heat flux radiated by the solar panels towards the [s/c](#) surface. The node area has been considered equal to the total surface of the [s/c](#) minus the external nodes 1 and 3 area.
- The external node 3 is the interface between the [s/c](#) and the deep space. The excess power is radiated away through this node, whose surface is considered equal to the sum of radiators' and louvers' surfaces.
- The internal node 1 contains the batteries, the [PCDUs](#) and both oxidizer and fuel tanks'. In both Earth departure and Moon eclipse cases, the power dissipated by this node is 50.89 W, and its temperature range is 0°C - 40.
- The internal node 2 contains all the other equipment mentioned in the [Table 7.2](#). The dissipated power at Earth's departure and in the Moon Eclipse are respectively 167.3 W and 178.8 W. The temperature range for this node is -10°C - 40°C.

Both radiative and conductive heat transfer are considered in the thermal network. The [MLI](#) design has been improved with respect to the single-node analysis, to better model the radiative heat transfer across the various layers. In particular, the outer and inner covers were added to the reflectors/spacers layers, which were already considered. The possibility of using a Kevlar layer for Micro-Meteoroid Orbital Debris ([MMOD](#)) protection was considered but discarded at this stage since these objects should not be a big threat to the LUMINOUS operative life [59].

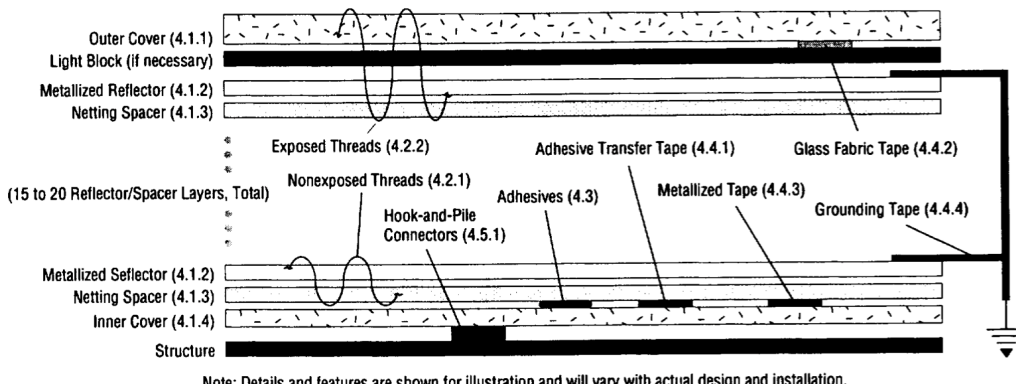


**Figure 7.3:** Typical [MLI](#) stacking arrangement. The schematic cross-section depicts the key elements of an [MLI](#) blanket. Not all elements need to be present in every design. [57]

The thermal network analysis has been performed considering a steady state in the two most critical conditions.

The sink temperature method has been used to deal with the external heat fluxes on the external node 1. The sink temperature has been computed with the [Equation B.12](#) that can be found in [section B.5](#). The solar panels' temperature has been assumed equal to the maximum and minimum one allowed by the Solar Arrays ([SA](#)) respectively for the Earth departure and Moon eclipse conditions.

### 7.3.2 Heat transfer assumptions

Radiative heat transfer is involved in most heat exchanges, but mainly from outside and from the internal nodes towards the [s/c](#) internal structure and from radiators towards deep space. Evaluating view factors is essential to understand how the surfaces of the different nodes' are linked. For this model a few assumptions have been made:



- The external node surfaces are considered perpendicular, so the view factor among them is zero.
- The external nodes and the internal ones are considered flat parallel surfaces, so with a view factor equal to one.
- The view factor between the solar panels' node and the external node 2 has been computed exploiting the [Equation B.13](#) available in section B.5

The following [Table 7.5](#) is the result of the assumptions above:

	EXTERNAL NODE 1	EXTERNAL NODE 2	SOLAR PANELS	EXTERNAL NODE 3	INTERNAL NODE 1	INTERNAL NODE 2
EXTERNAL NODE 1	/	0	0	0	1	1
EXTERNAL NODE 2	0	/	0.2071	0	1	1
SOLAR PANELS	0	0.7929	/	0	1	1
EXTERNAL NODE 3	0	0	0	/	1	1
INTERNAL NODE 1	1	1	0	1	/	0
INTERNAL NODE 2	1	1	0	1	0	/

**Table 7.5: View Factors**

Also, conduction is considered in the thermal network, mainly between the two internal nodes and from them towards the radiators. The two internal nodes are separated by a metal sheet, with structural functions, which conduct heat. The internal node is then coupled directly via conduction to the [s/c](#) radiators to better dissipate heat. Conduction is not considered in the [MLI](#) since that layer has the precise goal of insulating, hence minimizing radiation. The solar panels are considered to be decoupled, so there is no conduction between them and the [s/c](#) structure.

### 7.3.3 Results and comments

The final design of the [TCS](#) is summarised in the following [Table 7.6](#)

	Surfaces	Temperatures	
Radiators	5.31 m <sup>2</sup>	Temperature range with 15°C margin	15°C - 25°C
MLI	6.45 m <sup>2</sup>	Earth Departure Case	24°C
Louvers	0	Moon Eclipse Case	26°C

**Table 7.6: TCS results**

The multinodal analysis shows that no louvers are needed, and confirms that also heaters are not necessary. This allows to design of a passive thermal, eliminating moving parts and power requested to the [EPS](#) and reducing the mass of the subsystem. The number of layers (twenty) and the material ([SSAK](#)) are then confirmed from the single-node analysis, with an addition of other two [SSAK](#) layers as outer and inner covers as components of the [MLI](#), to insulate the internal environment from the deep space. [SSAK](#) is a good choice since can be used both for inner and outer covers but also as reflector material, allowing to use of a single material, allowing to avoid studying the compatibility between this and other materials. Moreover, this film can minimize the heat flow transfer to and from a spacecraft and can withstand the extreme temperatures of space while offering superior radiation resistance with minimal physical changes and with a proven spaceflight heritage [60]. Aluminum radiators covered with AZ-93 with paint are selected due to the high emittance and great resistance to radiation [61]. The proposed design can grant the margined temperature range at the Earth Departure case, while for the Moon eclipse condition the [s/c](#) internal temperature is hotter than what is allowed of 1°C. This can be a criticality in the long-term and shall surely refined in further iterations of this design. A possible explanation for the fact that the temperature in eclipse is similar but higher than the one at the Earth departure could be that the [MLI](#) effectively isolates the [s/c](#) from the external environment, but since the power dissipation is higher in eclipse, as all systems are active during the observation phase, the internal temperature could be higher.

## 7.4 Mass and Power computations

In order to conclude the design, the mass and power needed by the [TCS s/s](#) must be computed.



### 7.4.1 Mass budget for the TCS

The masses required by the [TCS](#) are the ones related to radiators and [MLI](#) and are dependent on the surface of these components.

#### MLI

For what concerns the [MLI](#), the mass can be computed as in the following [Equation 7.2](#):

$$m_{MLI} = N_{layers} * A_{MLI} * \rho_{kapton} = 1.561\text{kg} \quad (7.2)$$

where the area is reported in [Table 7.6](#), while the other material properties are reported in [Table B.3](#). Please note that the density of the kapton layer is associate with the thickness of the layer itself. Here a thickness of 0.0076 mm (0.3 mil)[\[57\]](#) has been assumed. Since the thickness of one single layer is known, it can also be computed the thickness of the overall MLI assembly as in [Equation 7.3](#):

$$th_{MLI} = N_{layers} * th_{1layer} = 0.1672\text{mm} \quad (7.3)$$

#### Radiators

The mass of the radiators can be computed knowing the area ([Table 7.6](#)) and the density (see [Table B.3](#) and assuming a thickness of the radiators equal to 0.1 m:

$$m_{rad} = A_{rad} * th_{rad} * \rho_{rad} = 1.4373\text{kg} \quad (7.4)$$

#### White Paint

The mass of the white paint which covers the radiators can be computed knowing the area (which is equal to the area of the radiators, stored in [Table 7.6](#)) and the density (see [Table B.3](#)):

$$m_{paint} = A_{rad} * \rho_{paint} = 1.2743\text{kg} \quad (7.5)$$

The results above are reported also in the following [Table 7.7](#)

Mass	
<b>MLI</b>	1.561 kg
<b>Radiators</b>	1.4373 kg
<b>White Paint</b>	1.2743

**Table 7.7:** Mass budget for the TCS

### 7.4.2 Power budget for the TCS

Since no heaters or other active thermal control components are required according to this preliminary design, the power required by the [TCS](#) subsystem in null.

## 7.5 Future Developments

The overall design is for now considered acceptable, with the feasibility of the mission under the thermal point of view which is demonstrated but there is obviously room for improvements. In particular, some steps to enhance the design could be:

- **improve the thermal network**, with at least one node for each external surface and one node for each internal component, as well as reviewing the view factors computations and assumptions.



- **move from a steady-state analysis to a dynamical simulation.** The first goal could be to simulate an entire operative orbit around the moon. The departure and transfer orbit could follow. In the end, the entire 6 years mission could be studied.
- **improve and verify the correctness of the internally dissipated heat.** Dissipated heat is very high and drives a lot of the design, especially in the Moon eclipse case.
- **further improve the MLI design,** increasing its complexity adding more characteristic elements.

# Chapter 8 On-Board Data Handling Subsystem

In this section, an insight into the on-board data handling subsystem is provided.

The **OBDH** system plays a crucial role in handling the processing of commands and the management of data for the spacecraft. This includes tasks such as timekeeping, overseeing both scientific and engineering data, and autonomously activating recovery and safe mode functions. Essentially, it serves as the spacecraft's central processing unit or "brain", intricately connected to every other component and subsystem through a bus system.

The first step towards the definition of this **s/s** consisted of deriving the implications that our mission requirements had on this specific system (these can be found in the requirements document in the OBDH section).

As far as concerns the architecture, the starting point is the ESA reference architecture, which can be found in [Figure 8.1](#)

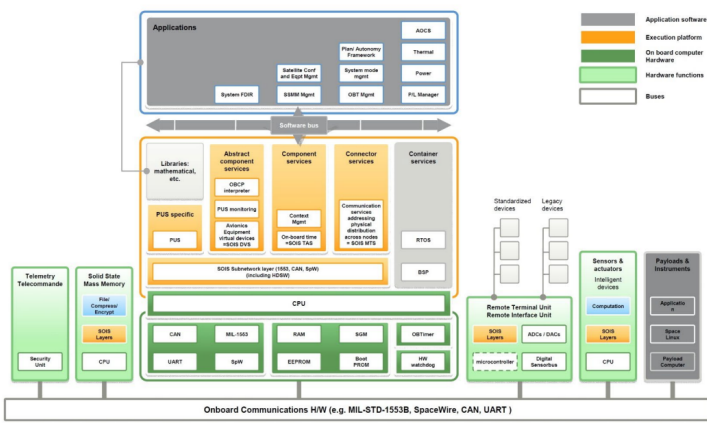


**Figure 8.1:** Reference ESA architecture

## 8.0.1 Partitioning of functionalities and preliminary trade-offs

Now as far as concern the partitioning of functionalities to be processed in space or on ground, given the autonomous nature of the **s/c** and the fact that the selected primary payload already takes care of its own data processing, the decision was in favor of performing the processing of data in space.

Hardware processing was selected in spite of the Software alternative since high performance was required and it's assumed that no changes will be made after the acquisition of the chosen hardware.

The next trade-off to be made regarding the choice of the data flow architecture.

Given the long lifetime of our mission, high importance was given to redundancy and reliability, hence the choice of adopting a distributed bus architecture since it enables running SW on multiple processing units. Let's note that SW in this case has to be stored in non-volatile memories.

Following the flow of the last trade-off, having selected a distributed bus data flow architecture, it makes sense to opt for redundancy on HW over one on SW, since in this way we can fully exploit the presence of multiple hardware on board. A triple modular HW redundancy making use of a voting logic (which assesses the three versions of each output and selects the version that is transmitted by two or all three sources.) will grant the processing high reliability

## 8.0.2 Resource needs estimation

The aim of this section is to initially gauge the sizing requirements of the OBDH software, encompassing RAM, Read-Only Memory (ROM), and throughput (measured in Thousands of Instructions Per Second (kIPS)), using the "similarity method. Upon identifying functions and components, memory needs (in memory word units) and Central Processing Unit (**CPU**) requirements (including typical throughput and execution frequency) are determined by leveraging similar



functions with known size and processing characteristics. It is important to note that for components already selected from off-the-shelf sources, inputs were extracted from their respective datasheets, such as in the case of sensors and actuators.

Acknowledging the preliminary nature of this estimation, a suggested margin of 400% will be applied. By maintaining a consistent ratio of throughput to execution frequency, the required throughputs for this mission can be calculated as follows:

$$KIPS = \frac{KIPS_{typ} \times f}{f_{typ}} \quad (8.1)$$

In the table below are displayed the data generated from each function or component present on board. The reason behind this table was to iteratively select each mode, considering the active functions for each, to identify the most demanding one from a data stream point of view.

Subsystem	Function / Component	N. of components	Code [words]	Data [words]	Typical throughput [kIPS]	Typical frequency [Hz]	Acquisition frequency [Hz]	kIPS	Total By Subsystem [kIPS]	Total [kIPS]	WORST CASE SCENARIO* [kIPS]
TTMTC	Signal acquisition	1	1000	4000	7	10	4	2,8	7,9	5373,4	3176,9
	Command preparation	1	800	1500	30	0,1	0,017	5,1			
EPS	Power management	1	1200	500	5	1	1	5	5	4391,6	3176,9
	Thrusters firing	12	600	400	1,2	2	1	0,6			
PS	Main thruster	1	300	375	5,0	0,1	1	50	53,6	4391,6	3176,9
	Latch valves	6	800	1500	3,0	0,1	0,1	3			
ADCS	Reaction wheel control	4	1200	300	5	2	2	5	4391,6	4391,6	3176,9
	Coarse Sun Sensor	4	2000	400	4	1	10	40			
	Fine Sun Sensor	2	2000	400	5	2	20	50			
	Star Tracker	2	4000	30000	4	0,01	10	4000			
	IMU	2	800	500	9	10	100	90			
	Error determination	1	1000	100	12	10	8	9,6			
	Kinematic integration	1	2000	200	15	10	8	12			
	Attitude determination	1	15000	3500	150	10	1	15			
	Attitude control	1	24000	4200	60	10	25	150			
	Orbit propagation	1	13000	4000	20	1	1	20			
OBDH	Fault detection	1	4000	1000	15	5	5	15	15,3	4391,6	3176,9
	Telemetry processing	1	1000	2500	3	10	1	0,3			
PAYOUT	Coronograph	1	36000	80000	90	0,3	3	900	900	900	3176,9

Figure 8.2: Preliminary data budget

\*note that in the scientific mode (hence also in the computations made), only one star tracker is active, as well as only one IMU

To obtain a reasonable estimate of the data processing workload, the total Instructions Per Second (IPS) was calculated, taking into account the worst-case scenario for the data budget. This scenario was identified in the scientific mode, where the **ADCS** expends significant effort, the payload is actively generating images, and background tasks are being handled by subsystems like the **EPS**. Components and functions active during the scientific mode are visually highlighted in yellow.

With this information, calculating the Read Only Memory (**ROM**) and Random Access Memory (**RAM**) requirements becomes straightforward using the following equations (assuming a 16-bit processor for the present analysis):

$$\text{ROM}[kB] = \frac{16}{8000} \text{code} \quad (8.2)$$

$$\text{RAM}[kB] = \frac{16}{8000} (\text{code} + \text{data}) \quad (8.3)$$

By adding the recommended 400% margin the results collected in Table 8.1 are found.



ROM [Mbyte]	RAM [Mbyte]	Throughput [MIPS]
1.08	2.12	15.884

**Table 8.1:** Results of the sizing

### 8.0.3 Selection of components

In order to select the microprocessor, it is possible to take into account also the partitioning of processing between **ADCS** and **OBDH** displayed in [Table 8.2](#). Now from the Asmad Book [45] it can be found that a **CPU** really close to the above processing partitioning is the RAD750, the radiation-hardened version of IBM PowerPC 750 microprocessor (all datasheets of the mentioned components can be found in [Appendix G](#)). The choice of this processor is highly recommended also because of its rich heritage and past success in 31 missions, including LRO which operated in a similar radiation environment and a long lifetime.

Ratio ADCS/TOT	58.13%
Ratio OBDH/TOT	4,96%

**Table 8.2:** Processing partition between **ADCS** and **OBDH**

Considering the limited timeframe, as the earliest feasible launch is set for 2027, this microprocessor choice makes it possible to save a significant amount of time since documentation (like the ISA, which is the PowerPC v.1.1), the benchmark program, the virtual platform to test the software, are already provided for this kind of processor.

Finally, the proposed architecture for the **OBDH** is to adopt the RAD750 6U CompactPCI single-board computer which is characterized by the usage of the RAD750 processor, integrated into a computer featuring:

- a Static **RAM** of 4 MB possessing Error Correction Code (**ECC**)
- a EEP ROM of 4 MB possessing **ECC**
- a Start Up Read Only Memory (**SUROM**) of 64 kB to store essential bootstrap code
- PowerPC RAD750® microprocessor

In addition to this, there is the possibility to transfer really easily the Operating systems for PowerPC 750-based computers into RAD750 computers and for the development of the software, Wind River Simics is furnished with a virtual platform in support.

As far as concerns the Data Storage Boards (**DSB**), it was considered that in each orbit the data stored from the main payload will be of approximately 6 to 8 images, each consisting of 48 Mbits. Since not much information is available on the amount of data produced by the secondary payload, to be conservative it is estimated that the data are as much as the ones coming from the coronograph. From these computations, and accounting for a possible missed communication window (due to which the memory would have to be able to store double the amount of data), the minimum value of memory found was 200 MB. Since this value is quite low, even adding the avionics housekeeping data, with the current technology of **DSB** it will not pose a problem to find a suitable **COTS** component.

Of course, since the S/C will be using S-band and X-band to communicate, it will be necessary to have the dedicated respective communication cards on board.

# Chapter 9 Configuration Subsystem Overview

## 9.1 Introduction to Configuration Subsystem

The spacecraft's configuration subsystem is vital for ensuring optimal performance throughout its operational lifespan. It was carefully designed from the outset to meet evolving mission requirements, with a lunar orbiter chosen over alternatives like Lagrangian points. As mission needs evolved, the subsystem was adjusted to optimize functionality and prevent unwanted interactions between subsystems.

A primary goal of the configuration subsystem is to harmonize all subsystem functionalities, ensuring smooth operation. For example, when selecting a near-equatorial orbit around the Moon, meticulous planning was required to integrate this trajectory with the spacecraft's design, considering factors like thermal management and power distribution during all the mission modes.

This chapter will explore the design process of the configuration subsystem, discussing key decisions and their integration within the mission framework. Also, the specific challenges encountered during configuration will be examined, highlighting their critical role in achieving mission success.

## 9.2 Spacecraft Shape Trade-off

Determining the preliminary shape of the spacecraft is a critical early step in the design process. Initially, the cubic architecture was considered, but it quickly became apparent that this shape was unsuitable due to the dimensions of the [LASCO](#) coronagraph payload. The longitudinal direction of the [LASCO](#) payload [2] was significantly greater than the other two dimensions, as clearly visible in [Figure 9.1](#) necessitating a reevaluation of the spacecraft's shape.

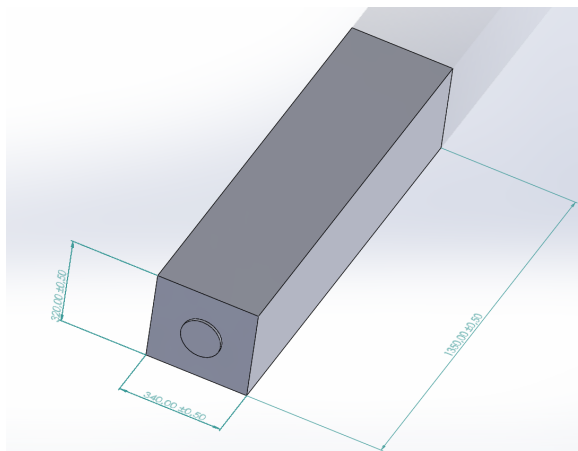


**Figure 9.1:** [LASCO](#) Payload's dimensions (300x340x1350 mm)

In response to this challenge, the prismatic configuration was explored. This configuration aligned the optical direction of the payload with the longer axis of the spacecraft, providing a more suitable arrangement for accommodating the [LASCO](#) payload.

However, during the design phase, the possibility of adopting a hexagonal shape emerged as an intriguing option. This shape offered potential advantages, including increased flexibility in sensor, actuator, and solar array placement. The hexagonal configuration also presented intriguing possibilities for the architecture of the propellant tank module.

Despite these benefits, the hexagonal shape was ultimately discarded for several reasons. Chief among these were concerns related to the [ADCS](#) and a desire to maintain simplicity in the spacecraft design. While the hexagonal shape offered advantages in terms of flexibility and potential compactness, these considerations were outweighed by the need for a robust [ADCS](#) and a straightforward design approach.

In conclusion, the trade-off analysis of spacecraft shapes involved careful consideration of various factors, including



payload requirements, design flexibility, system complexity, and operational robustness. Ultimately, the decision to adopt the prismatic configuration over the hexagonal shape was driven by a balance of these factors, ensuring a spacecraft design that meets mission objectives effectively and reliably.

### 9.2.1 Initial Dimension for Inertia Matrix Calculation Methodology and Assumptions

To establish preliminary values for the spacecraft's inertia matrix, a comprehensive analysis was conducted, accounting primarily for the propellant tanks' volume. Additionally, initially we considered statistical considerations[38] for other components such as cabling, internal computers, and structures. While developing these dimensions, we initially assumed a uniform density for the spacecraft to ensure alignment with the continuously evolving mission mass budgets, which underwent continuous adjustments throughout the design process. Subsequently, we progressed to study the internal configuration, leveraging the computed dimensions and inertia matrix as foundational parameters. This integrated approach allowed us to iteratively refine the spacecraft design while ensuring adherence to mission requirements and constraints.

## 9.3 Final System Architecture

The final proposed solution for the orbiter's architecture is depicted in Figure Figure 9.2.

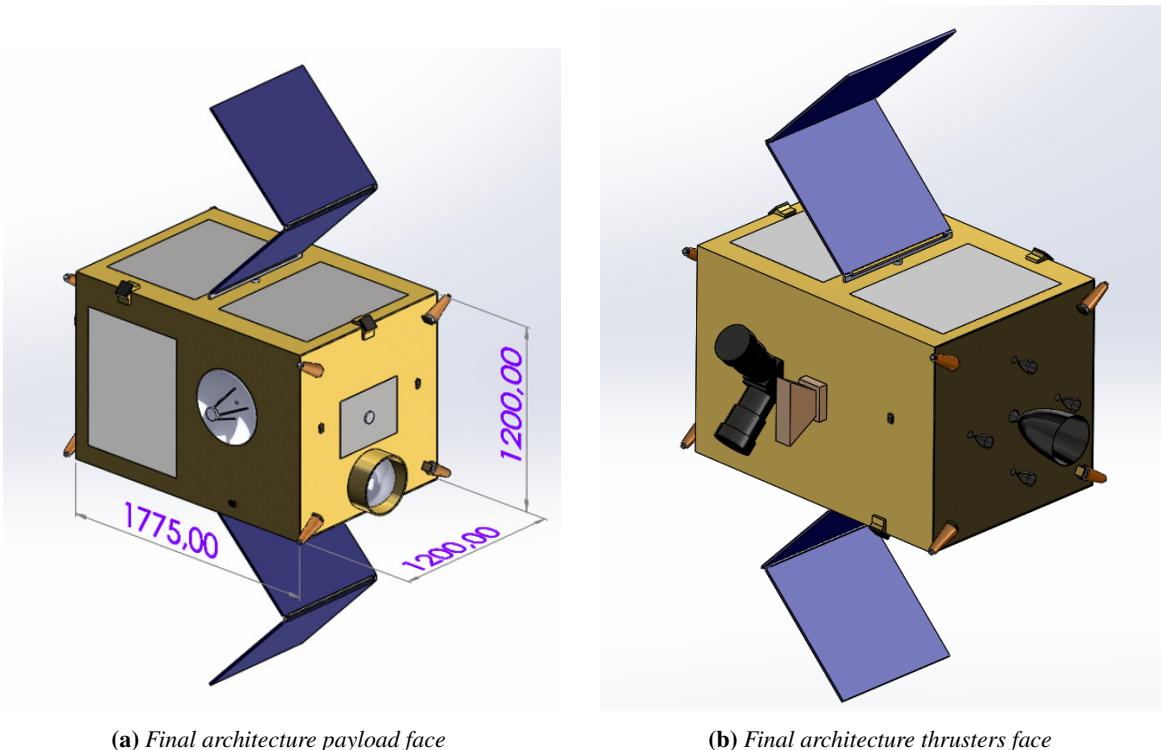


**Figure 9.2:** Final spacecraft configuration

In Figure 9.10a, the payload is depicted at the center of the squared face, positioned directly above the pressurizing gas tank. Additionally, the HGA is visible, mounted on one of the two lateral faces.

In Figure 9.2b, the squared face accommodates the thrusters, situated opposite to the payload face. Meanwhile, on the lateral face opposite to the HGA, Star Trackers (depicted in black) and the Secondary Payload are visible.

Solar panels are affixed to both the upper and lower surfaces of the spacecraft. Additionally, desaturation thrusters are positioned at the four corners of both the payload and thruster faces.

In the subsequent sections, we will analyze the main trade-offs that influenced the final design decisions, providing insights into the decision-making process and rationale behind the chosen architecture.



## 9.4 Payload

For the Luminous mission, two payloads were adopted:

- 1 Coronagrapher (taken as reference the CCOR [3])
- 1 Secondary payload SMEI [4]

For the Coronagraphic, no particular configuration constraints are found, apart from leaving its boresight free from all kinds of disturbances. It was placed on the face opposite the principal thruster, which is the one that will have to be pointed to the Moon during the operational phase.

Regarding the secondary payload instead, it has to be placed on a face orthogonal to the axis of rotation of the spacecraft (and again, far from disturbances on its FOV), since it has to "scan" the sky during the rotation. For this reason, it was placed on one of the two lateral faces of the spacecraft. In figure Figure 9.3 the two payloads are visible.

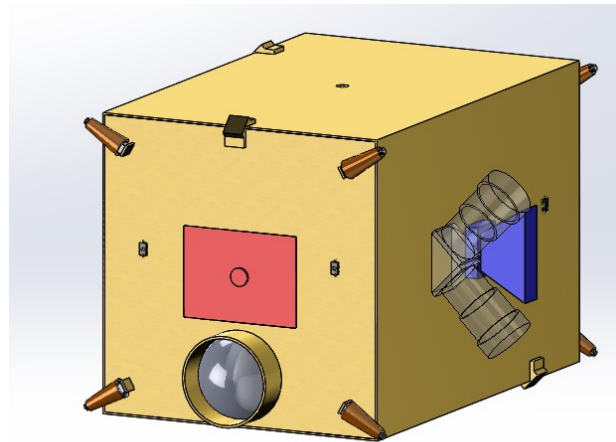


**Figure 9.3:** In Red: Primary Payload [3] in Blue: Secondary Payload [4]

## 9.5 Propulsion Module

The Propulsion Module consists of all the components that contribute to supply thrust to the spacecraft, whose main components are listed here:

- Thrusters (primary and secondary)
- Propellant tanks (Fuel and Oxidizer)
- Pressurizing gas tank
- Propellant feed system
- Structural components

In the following Figure 9.4 the propulsion module is highlighted. In black the primary thruster (Leros-1C) and the 4 station keeping thrusters, are mounted on the face opposite to the payload. In blue is the Oxidizer tank, and in red are the four Hydrazine tanks.

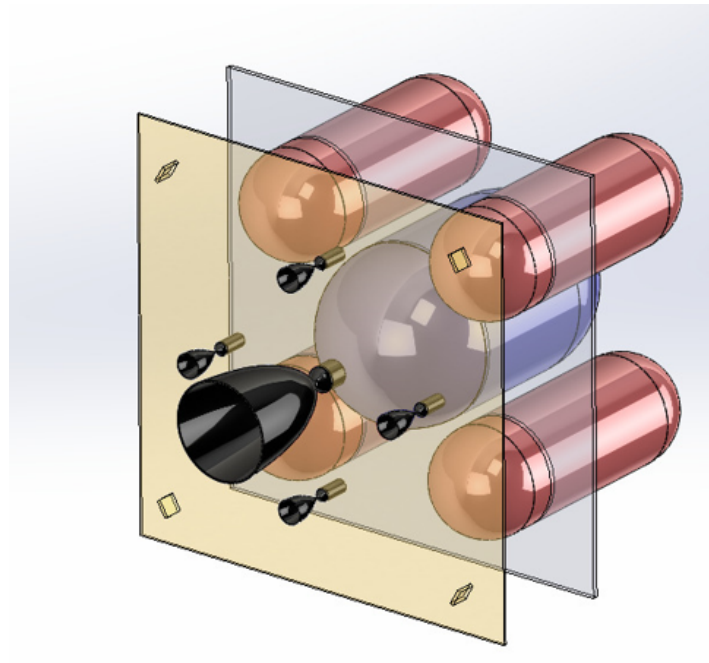


**Figure 9.4:** Propulsion module

### 9.5.1 Thrusters

The primary consideration guiding the positioning of each adopted engine is to avoid interference with other surfaces, optical sensors, or antennae FOV. This is crucial and was probably the main challenge regarding the thruster configuration. Beginning with the primary thruster, careful attention was paid to ensure alignment with the CoG of the spacecraft throughout its operational life. Positioned along the payload's direction, this orientation was chosen to align with the axis designed to withstand higher axial stresses, particularly during launch accelerations. This strategic placement not only optimizes functionality but also minimizes potential structural strain over the spacecraft's lifespan.

Next, the four stationkeeping thrusters are positioned on the same face as the primary thruster, equidistant from it. This arrangement offers increased flexibility and precision during stationkeeping maneuvers, where the high thrust of the Leros-1C might prove excessive and inaccurate.

As for the Attitude Control Thrusters, their placement allows for the desaturation of all reaction wheels while ensuring no interference with other spacecraft components. This configuration optimizes the spacecraft's maneuverability and stability during attitude control operations.

### 9.5.2 Propellant tanks (Fuel and Oxidizer)

Starting from the total needed volume of both fuel and oxidizer, the goal in this case was to find the optimal disposition of the tanks to be placed inside the spacecraft. The main followed in tradeoffs are shown here:

- Center of Gravity close to the geometrical center of s/c.
- Symmetrical configuration to reduce CoG shift during fuel consumption.
- Tanks placed in an optimal position to reduce thrusters feed system length.
- Minimization of the total mass of the tanks (2 spherical tanks would have been optimal for this).
- Keep the system as compact as possible.

Initially, a design with only two spherical tanks was considered but proved unfeasible due to volume constraints. Any attempt to use only two tanks, one for fuel and one for oxidizer, would have been overly complex and difficult to meet CoG requirements. While two cylindrical tanks stacked vertically could potentially meet CoG requirements, they would



necessitate an elongated spacecraft. Consequently, the focus shifted to considering multiple tanks for either fuel or oxidizer (cylindrical for compactness).

The most logical option, given the absence of other constraints, is to place the smaller tank (oxidizer) singularly in the middle, with the fuel tank divided and arranged symmetrically around it.

At this stage, three alternatives were considered: configurations with 2, 3, or 4 fuel tanks. While the 2-tank configuration minimizes system mass, it results in significant asymmetry constraining one dimension much bigger than the other (visible in [Figure 9.5c](#) and was quickly dismissed).

The main trade-off then lay between the 3 or 4-tank options, as depicted in [Figure 9.5](#).

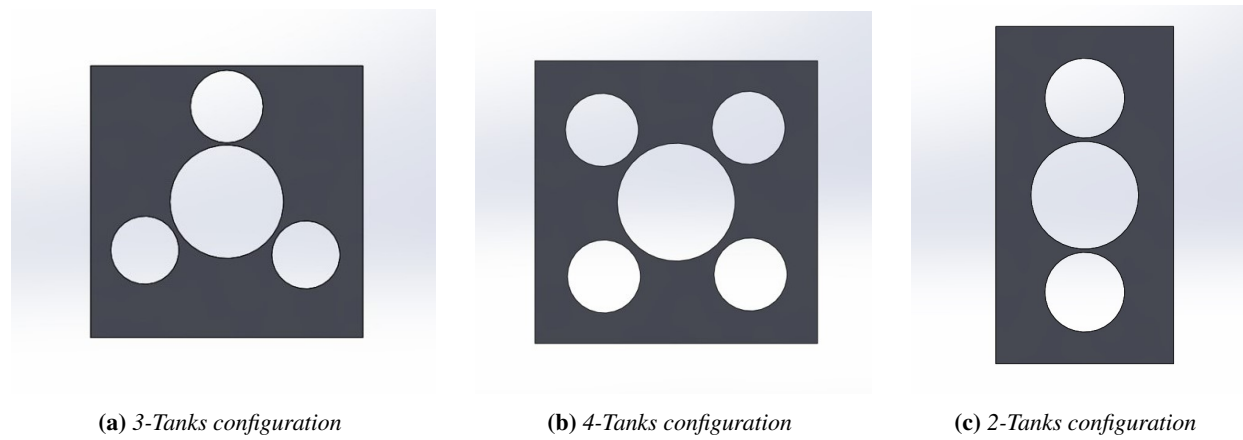


**Figure 9.5:** Comparison between 2, 3 and 4 tanks configuration

Although the 3-tank option ([Figure 9.5a](#)) has a lower overall mass, the 4-tank option ([Figure 9.5b](#)) is more compact and better meets the [CoG](#) requirements. Therefore, the 4-tank configuration was ultimately preferred for the final design.

### 9.5.3 Pressurizing gas tank

To mitigate the dry mass of the pressurization system, a strategy involves storing the pressurizer (Helium) at low temperature and high pressure, thereby augmenting its mass within a specified volume. Consequently, the tank was positioned externally to capitalize on reduced storage temperature, visible in [Figure 9.3](#) as the white sphere below the primary payload, leading to diminished size and mass. Additionally, external placement minimizes internal bulk, enhancing spacecraft compactness. However, implementing this approach necessitates careful consideration to prevent critical pressure increases during solar exposure, which could potentially damage the tank material through repeated cycles. Thus, the tank was designed to endure pressures corresponding to a 15°Celsius increase in gas temperature. Computational analysis determined the continuous sun exposure required to trigger such an increase, ensuring it remains within safe limits. Subsequent verification confirmed that the tank never faces prolonged sun exposure to reach critical temperatures. Consequently, a dedicated slew maneuver was incorporated to adjust spacecraft orientation when facing the sun. For the above reasons, the tank was placed in the payload's face, which appears to be the least exposed to the sun (except the Solar Panels faces, which were preferred to be left dedicated to the panels). However, their adoption as faces to host the cryogenic tank might be favored by subsequent studies. Moreover, the tank was placed inside a reflective cylinder, which further reduced the tank's exposure to the Sun.

## 9.6 Solar Array

The placement of the solar arrays was a primary consideration in the early phases of mission planning. This section focuses on the rationale behind their configuration. The main objective was to minimize the [SAA](#) to enhance solar power generation efficiency. To achieve this, the solar arrays were designed to rotate around their axis using a mechanism, strategically adjusting their orientation to optimize energy capture. Given our orbit's proximity to the ecliptic plane, the solar panels were primarily placed in the out-of-plane direction, ensuring optimal exposure to sunlight throughout the mission.

Ensuring that the folded configuration of the solar panels did not interfere with other spacecraft components was also a pri-



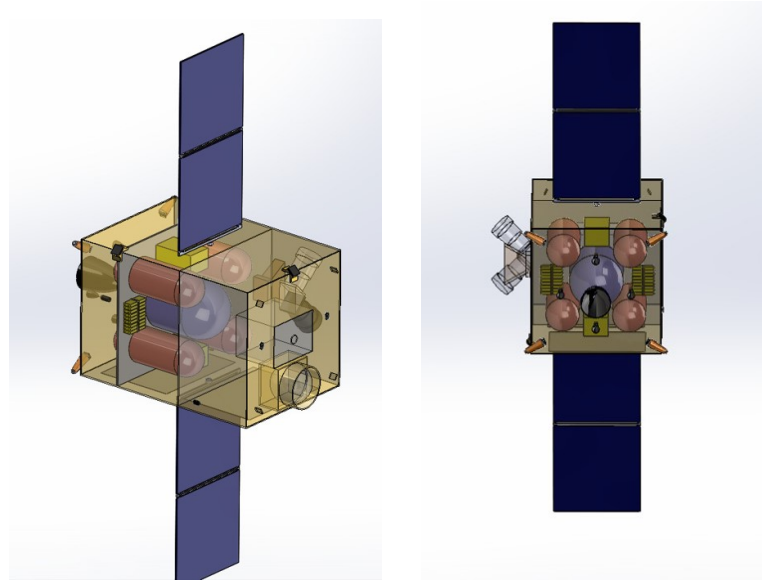
ority, with careful attention paid to prevent potential interactions. This decision had broad implications for the spacecraft's overall design, deeply influencing the positioning of other components and shaping subsequent design choices.

## 9.7 Electrical power management module

This module is comprehensive of the following components:

- Solar Array
- 2 PCDUs (Power Conditioning & Distribution Unit)
- 2 Battery packs

The disposition of the Solar Array was detailed in the preceding section. The **PCDU**, acting as the power management unit, has been positioned near both the Solar Array and batteries to reduce cable lengths. Additionally, due to the considerable heat produced by this module, it has been placed close to the Propellant Tanks, which experience one of the highest temperature ranges. In Figure 9.6, **PCDUs** are visible as the two yellow boxes right below the **SA**, while the batteries are the 2 yellow in adjacent positions.

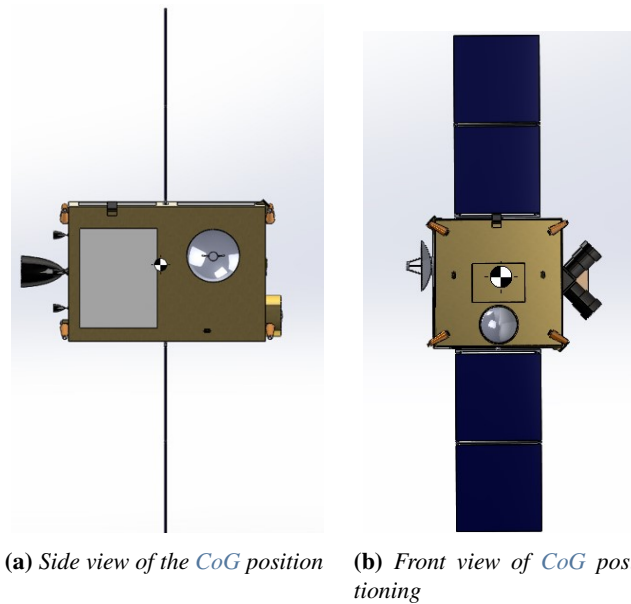


(a) View on the internal positioning of batteries and PCDUs    (b) Backview of S/C highlighting batteries and PCDUs

**Figure 9.6:** Electrical components internal disposition

Particular attention will be given to the placement of radiators in this area, as it may require increased power dissipation during certain phases of the mission.

Furthermore, due to the substantial mass of these components, their placement near the geometric center of the spacecraft contributes to the positioning and stability of the **CoG**, as shown in Figure 9.7a, Figure 9.7b which could be beneficial.



(a) Side view of the *CoG* position      (b) Front view of *CoG* positioning

Figure 9.7: *CoG* position

## 9.8 Antennae and OBDH

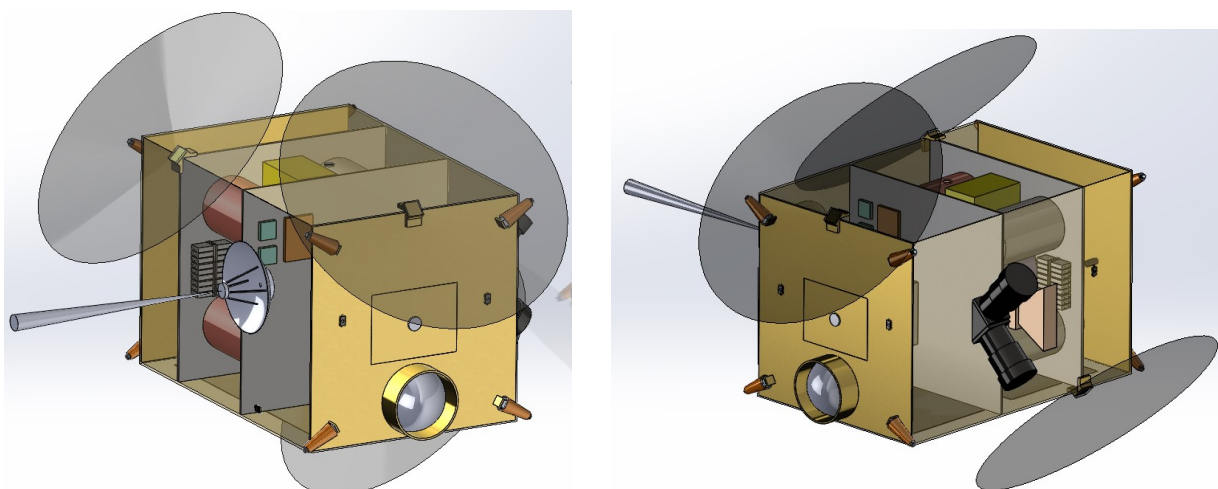
The antennae positioning is critical, to ensure safe communication (both operational and in emergency cases). The main driver for the antennae positioning (apart from their **FOV** that must of course be free) is that they must be free from interference sources like the thruster's plumes.

The secondary driver is to minimize internal cabling lengths and to maximize the overall coverage of the **LGA**s.

The list of components for this module is listed here:

- One parabolic **HGA** (Diameter : 0.4 m, **FOV** =  $2^\circ$ )
- Three **LGA**s (**FOV**= $80^\circ$ (half cone))
- Two X-Band transmitters [44]

In Figure 9.8a, the **HGA** is visible with its narrow **FOV**, in orange right behind the **HGA** instead is the On Board Computer, while the two green boxes close to it are the two X-Band transceivers. The 3 **LGA** are visible with their **FOV** of  $160^\circ$  in Figure 9.9.



(a) View 1 highlighting the antennae

(b) View 2 highlighting the antennae

Figure 9.8: *Antennas and OBDH*



### 9.8.1 High Gain Antenna

Initially, the mission modes didn't include a specific maneuver for the communication phase, leading to consideration of a robotic arm with 2 Degree of Freedom (DoF) starting from the [HGA](#). However, this solution was later replaced by a dedicated communication mode involving a slew maneuver, pointing directly to Earth. Consequently, the robotic arm was eliminated, and the [HGA](#) was fixed to one of the two lateral faces.

This adjustment significantly simplified the system by removing mobile parts like the robotic arm. Placing the [HGA](#) close to the payload's face further streamlined operations by reducing cabling lengths. Additionally, this positioning brought the [HGA](#) in proximity to both payloads, most sensors, and the On-Board Computer, facilitating efficient data processing before downlink.

### 9.8.2 Low Gain Antennas

The chosen [LGAs](#) are highly compact and possess a wide [FOV](#), covering a cone 160 degrees wide. Their primary function is during the initial phases of the mission, particularly when the [HGA](#) pointing is imprecise or in case of emergencies.

Additionally, in the event of [HGA](#) malfunction, these antennas could potentially transmit scientific data to the Lunar Gateway, which could then relay the data back to Earth. However, this possibility requires further investigation.

The decision to configure three [LGAs](#) positioned in different directions, as illustrated in Figure 9.9b, was driven by the aim to maximize overall coverage. This configuration not only enhances redundancy but also ensures comprehensive coverage across various directions.

### 9.8.3 On Board Computer and Transceivers

Both the On Board Computer (orange box in Figures 9.9a 9.8a) and the two X-band transceivers (blue boxes close to the On Board computer, visible in Figures 9.8a 9.9a) have been situated in close proximity to the [HGA](#) within the same region as the payloads and sensors. Their placement was meticulously selected not only to minimize cable lengths but also to leverage the thermal properties of these components, which benefit from being in a cooler environment.

## 9.9 Actuators and Sensors

The list of sensors and actuators employed in the spacecraft, is listed here:

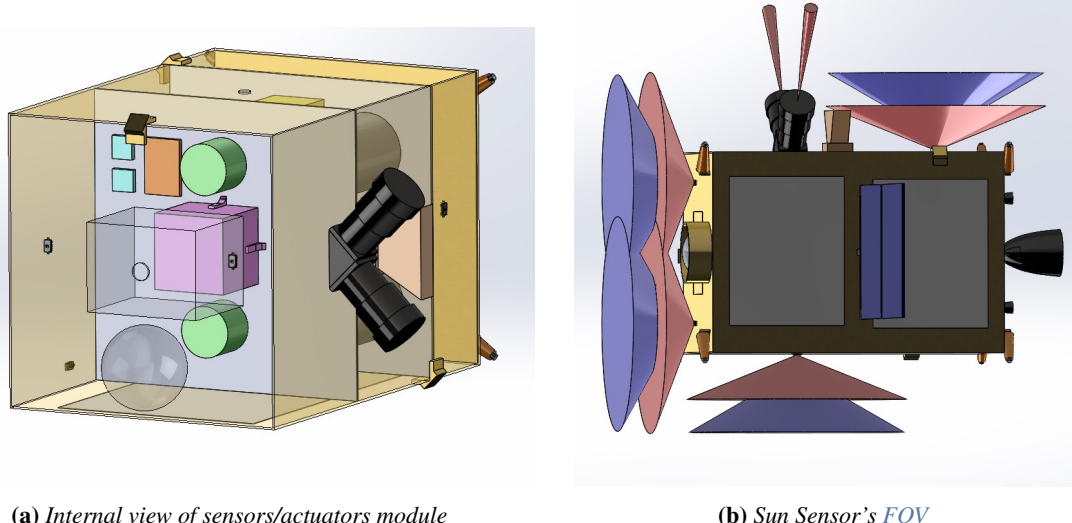
- 1 Reaction wheel block[62]
- 2 IMUs[31]
- 4 Sun Sensors [63]
- 2 Star Trackers [64]

In Figure [Figure 9.9a](#), the depicted components are readily identifiable. The reaction wheels block is represented by the purple box, while the two [IMUs](#) are depicted as green cylinders. Additionally, the Star Trackers are illustrated as black cylinders. In [Figure 9.9b](#), the blue cone represents the effective [FOV](#) of the Sun Sensor, which must be free of disturbances. Conversely, the red area denotes the [FOV](#) of the Sun Sensor that must be free of reflective surfaces. The diagram illustrates that the wider [FOV](#) (red) of the Sun Sensor is devoid of reflective surfaces, ensuring optimal functionality. Conversely, the narrower [FOV](#) (blue) is simply required to be free from any disturbances.

In this setup, the Reaction Wheels block was strategically placed near the spacecraft's [CoG](#), positioned between the coronagraph and the oxidizer tank.

The [IMUs](#) were mounted alongside the reaction wheel on the same plate, as shown in figure [Figure 9.9a](#). This arrangement aimed to consolidate sensors and actuators in close proximity to each other and to the onboard computer.

Regarding the 4 Sun Sensors, 2 were installed on the payload's face (with 1 for redundancy) to trigger the slew maneuver automatically when the Sun is detected, ensuring prompt exposure to shadow. The other two Sun Sensors were placed on the side faces to maintain an unobstructed [FOV](#).



(a) Internal view of sensors/actuators module

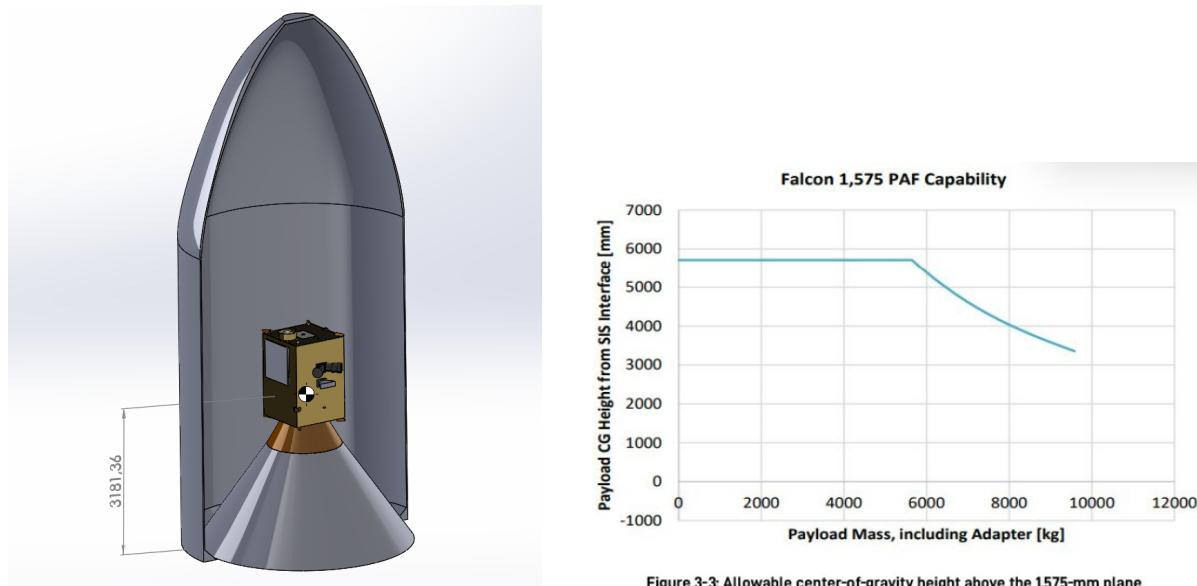
(b) Sun Sensor's FOV

**Figure 9.9:** General view of all actuators/sensors present in the spacecraft

The two Star Trackers, positioned on the secondary payload's face opposite the [HGA](#), are oriented 90 degrees apart to ensure operational redundancy in case of sunlight interference [Figure 9.9a](#). Once again, they are placed near the onboard computer to minimize cable lengths.

## 9.10 Launch configuration

Here is shown the folded Solar Panels configuration, which will be the one present during the launch until [SA](#) deployment.



(a) Luminous spacecraft in folded configuration inside the Launcher's fairing

(b) Maximum allowable CoG height for launcher's specifications [65]

**Figure 9.10:** Launch configuration and CoG height [65]

As it's possible to see in figure 9.10b the [CoG](#) of the folded spacecraft + the launcher adapter is 3.18 meters, well below the stability margin of table 9.10.

# Chapter 10 Structures

The goal of the structures subsystem is to provide mechanical strength and stability to the *s/c* throughout the various phases of the mission. The work done on the *s/s* was in accordance with the mass and  $\Delta V$  budget. Also inputs from other *s/s* like Configuration, EPS & TCS were valuable for sizing the structures *s/s*. The critical phases that were considered for the *s/s* were the launch phase and the science mode because the maximum loads acting on the *s/c* are happening during the launch while the science mode is critical because the subsystem has to ensure stability during observation so as to fulfill the functionality of the mission. In this chapter, various analyses done to size the structure subsystem along with the trade-off in material selection for the *s/c* will be presented. Finally, a note about the need to maintain accuracy and stability while the *s/c* is performing observation during the eclipse time is posted.

## 10.1 Material selection

The selection of materials for the frame of the *s/c* was done based on a trade-off between various metallic and non-metallic alloys & composite materials. The materials that were discarded in the initial trade-off were:

- **Magnesium:** although it is lightweight, it is not strong, and has issues with corrosion in the presence of moisture.
- **Beryllium:** although it has the ability to retain its properties at very high temperatures, it is difficult to fabricate and due to its toxic nature, it poses a health hazard. Also, Beryllium tends to be more expensive than other commonly used metallic alloys.
- **Graphite:** it is fragile at room temperature, although it has the unique property of improving its strength at very high temperatures. Hence its use does not coincide with the LUMINOUS mission.
- **Carbon-Fibre:** susceptible to degradation from atomic oxygen, has very little thermal and electrical conductivity. Carbon fiber composites require specialized manufacturing techniques such as layup, curing, and autoclaving and are much harder to manufacture as compared to other metallic and non-metallic alloys. The cost of obtaining and manufacturing carbon fiber is very high.

After careful consideration, the final set of materials selected was Aluminium 7075, T6, and Titanium Ti-6Al-2Sn-2Zr-2Mo(annealed), the reason being high strength-weight ratio possessed by both & high values of yield strength which supports the spacecraft structurally in extreme load conditions. also, Aluminium and Titanium have been the common choice of engineers for use in space missions which makes them reliable for use in the Luminous spacecraft.

### 10.1.1 Aluminum 7075, T6

- **Strength-Weight ratio:** Aluminium has a low strength-weight ratio. It is 62% lighter than Titanium but not as strong as Titanium.
- **Stiffness:** Aluminum has a very good shape factor of 15 which restricts buckling and yield strength of 460-530 MPa.
- **Thermal & Electrical conductivity:** it exhibits highest thermal and electrical conductivity. The aluminum structure can be doubled as electrical grounding.
  - Thermal Conductivity:  $161 - 174 \frac{W}{m * K}$
  - Electrical Conductivity:  $2.2 * 10^7 - 2.38 * 10^7 \Omega$
- **Temperature Resistance:** -100°C to 1668°C.
- **Manufacturability:** Aluminum is relatively easy to machine, shape, and weld. It is widely used due to its ease of manufacturing into various shapes and structures.



- **Environment risks:** Aluminum is susceptible to corrosion in space due to Atomic Oxygen (AO), radiation, and other space-specific elements.
- **Cost efficiency:** Aluminum is very cost-efficient. Due to the properties stated above and keeping in mind the high TRL, Aluminium 7075, T6 has been chosen as the primary material for the outer frame of the LUMINOUS s/c.

### 10.1.2 Titanium - Ti-6Al-2Sn-2Zr-2Mo (annealed)

- **Stiffness:** it has better stiffness than Aluminum, which makes it a viable option where stresses are high: Some of its mechanical properties are:
  - Yield strength: 933-1210 MPa
  - Tensile strength: 1030-1220 MPa
  - Compressive strength: 933-1220 MPa
- **Strength-Weight ratio:** Titanium has a higher strength-weight ratio than Aluminium.
- **Thermal & Electrical conductivity:** Thermal & Electrical conductivity of Titanium is less than Aluminum:
  - Thermal Conductivity:  $20.5 - 20.7 \frac{W}{m * K}$
  - Electrical Conductivity:  $1.75 * 10^6 - 1.81 * 10^6 \Omega$
- **Temperature Range:** -100°C to 660 °C.
- **Environment Risks:** Titanium exhibits good corrosion resistance in space environments due to its natural oxide layer that protects it from corrosion caused by atomic oxygen.
- **Manufacturability:** Titanium is more challenging to work with compared to aluminum due to its high reactivity and toughness.
- **Cost efficiency:** more expensive than Aluminum.

Due to its high strength and ability to withstand loads before deforming, this Titanium alloy has been chosen as the material for inner horizontal supports, connections, tanks & thrusters in the Luminous spacecraft.

## 10.2 Modal Analysis

The modal analysis was necessary to calculate the natural frequency of the s/c. This is a critical parameter during the launch phase because the natural frequency of the s/c and the frequency of the launch vehicle shall not coincide in order to avoid any instances of resonance that could lead to unwanted vibrations and consequently lead to failure in the launch phase. Hence, careful considerations were taken while performing the modal analysis, keeping a backup solution in mind in case of extreme conditions.

### 10.2.1 Natural Frequency of LUMINOUS spacecraft

To calculate the natural frequency of the s/c, the Young & Budynas [38] was used, which is given by Equation 10.1

$$f_n = \frac{1}{2\pi} \sqrt{\frac{3EIg}{WL^3}} = \frac{1}{2\pi} \sqrt{\frac{3EI}{ML^3}} \quad (10.1)$$

Where  $E$  is the modulus of elasticity,  $I$  is the area moment of inertia,  $g$  is the acceleration due to gravity,  $W$  is the weight of the beam,  $M$  is the mass of the beam ( $W/g$ ), and  $L$  is the length from the beam root to the center of mass.

Some assumptions were made in the Young & Budynas equation to find the natural frequency:

- The s/c is assumed to be a cantilever beam attached at the launch vehicle interface using a ring-shaped structure with an outer diameter of 0.9 m and thickness of 1 mm.
- The modulus of elasticity was considered to be that of Aluminium, so 70 GPa.
- The mass of the s/c was considered to be 813.78 kg based on the final wet mass



## Result

Based on the following assumptions, the first natural frequency of the *s/c* during the launch phase was found to be 52.7374 Hz.

This was compared to the Sound Pressure Level provided by the Falcon 9 vehicle datasheet [65], which is represented in Figure 10.1.

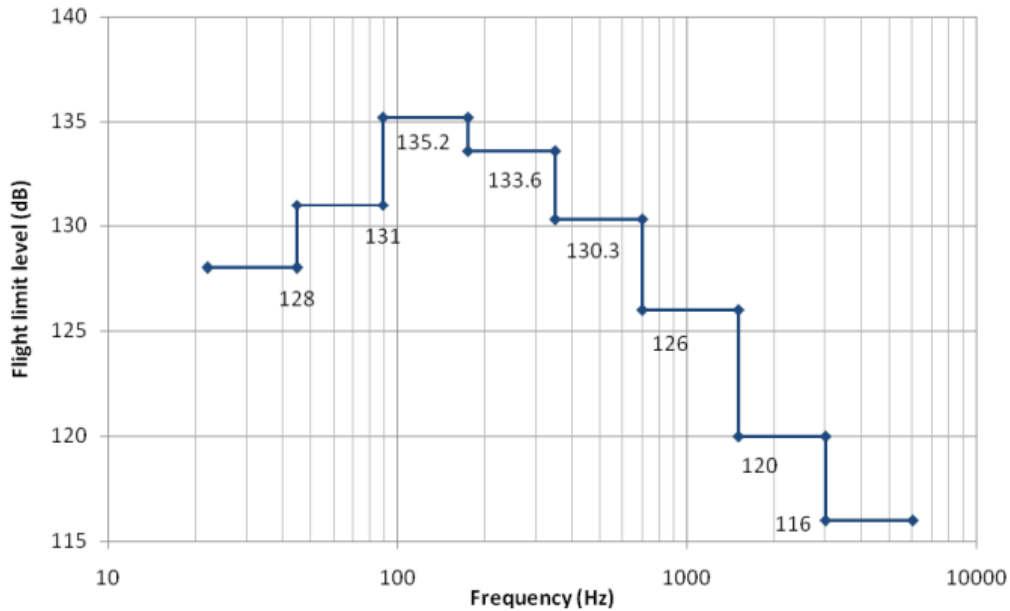


Figure 5-4 - Falcon 9 acoustic environment requirement (OASPL=139.6 dB)

Figure 10.1: Frequency Vs. SPL

From Figure 10.1, it can be seen that the LUMINOUS *s/c* has a Sound Pressure Level of 128 decibels for a natural frequency that was calculated to be 52.7374 Hz, and as mentioned in the datasheet, the overall Sound Pressure Level of Falcon 9 is 139.6 decibels.

These values were compared with each other:

- Due to a significant gap in those numbers, there is no immediate risk of resonance to the mission during the launch phase as resonance will occur when the sound pressure level of both the spacecraft and the launch vehicle come dangerously close to each other.
- Further tests like random vibration testing need to be conducted to understand the vibrational load-bearing capacity of the structure.

In case the vibrational loads tend to be more than what is expected from the modal analysis, a vibration damper can be employed between the *s/c* and the launch vehicle interface.

### 10.2.2 Vibration Damper during Launch

This is a solution that is kept as a backup option for emergency cases where the risk of vibrations is very high. Introducing a vibration damper between the launch vehicle and the *s/c* interface can significantly reduce the amount of vibrational loads acting on the *s/c* during the launch phase, loads that can pose a threat to the mission.

Various vibrational dampers have been employed in previous space missions, for example[66]; NASA used a total of 16 Tuned Mass Dampers in the solid fuel boosters and some conventional vibration isolators between the rocket stages of the Ares 1 crew launch mission. This was part of a design strategy to reduce peak loads from 6 g to 0.25 g.

The choice of damper for the LUMINOUS mission was taken to be "Modular Active Vibration Isolator" by Daeil Systems, shown in Figure 10.2



**Figure 10.2:** Active Vibration Isolation System

The reason for this choice being

- **Load holding capacity is less than 700 kg**, which means two of these platforms shall be used based on LUMINOUS s/c.
- **Active isolation range:** 0.5-100 Hz, which allows the first natural frequency to fall under that range.
- **Very high performance:** higher than 90% for frequency greater than 4Hz.
- **Very low settling time**, almost less than 0.3 seconds, which offers quick stability to the s/c under a vibration environment.

The datasheet for the isolator is provided in [Figure E.1](#)

## 10.3 Static Structural Analysis

The next analysis performed was the static structural analysis of the s/c. For this, the software Ansys was used due to its reliability & accuracy of results in the simulation field.

The static structural analysis was important to be performed in order to find the maximum stress and deformation that will be present during the mission. Based on the calculated stress, the safety factor was determined.

Based on the launch vehicle's datasheet [65], it was found that the s/c undergoes maximum stress during the launch phase which is

- Maximum Axial acceleration: 8.5g
- Maximum Lateral acceleration: 3g

### 10.3.1 Assumptions

Various assumptions were taken into consideration before performing the static analysis:

- A simplified model was considered as seen in [Figure 10.3](#) barring the solar panels and the TTMTC antenna due to ease of meshing but the point of connections was considered in order to analyze the deformation.
- Aluminium 7075, T6 was the material considered for the outer frame structure.
- Titanium alloy Ti-6Al-2Sn-2Zr-2Mo(annealed) was the material considered for the support structures, internal supports, the node of connections, tanks, and thrusters.

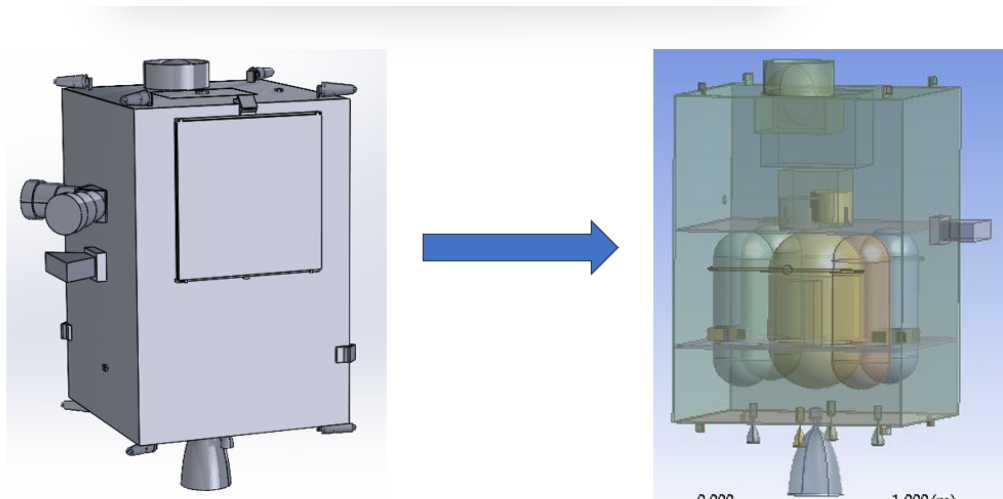


**Figure 10.3:** Real model Vs. Simplified model for analysis

Based on the assumptions, the maximum acceleration acting in the axial and lateral direction during launch and the simplified model, the analysis was performed and results were calculated for the equivalent stress (Von Mises) and total deformation, based on which the safety factor was determined.

## Results

### 10.3.2 Equivalent stress(Von Mises)

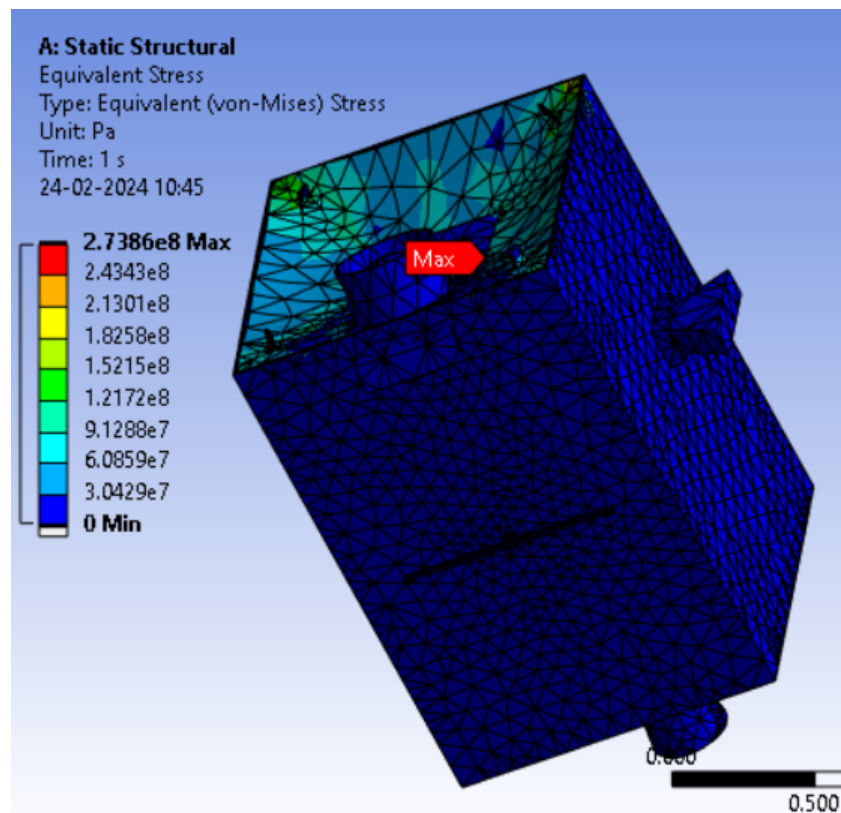


**Figure 10.4:** Equivalent Von Mises stress

From the result, it was seen that the maximum stress acting on the *s/c* during the dynamic launch phase is 273.86 MPa. The point of maximum stress is also highlighted on Figure 10.4.



### 10.3.3 Safety Factor

Based on the maximum stress found, the safety factor was determined by keeping the yield strength of Aluminium 7075, T6 as a reference for worst case scenario as the yield strength of the Titanium alloy is much more than that of Aluminium and also the maximum point of stress is seen to be in the outer frame.

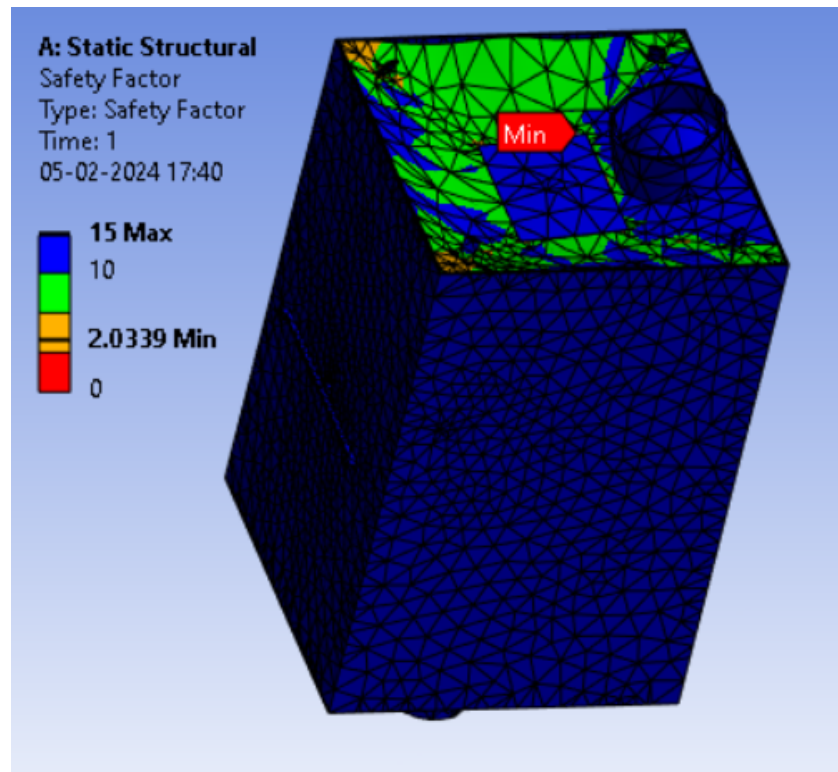


**Figure 10.5:** Safety Factor

From the result of equivalent stress, using the formula

$$SF \text{ (Safety factor)} = \frac{\text{Yield strength}}{\text{Maximum stress}} \quad (10.2)$$

the minimum safety factor was found to be 2.0339.

Then, a 10% margin was applied to the maximum accelerations in both the axial and lateral direction and the resultant safety factor was found to be: 1.8305, which is higher than the universal standard of 1.5.

From this, it was concluded that the structure is safe, and stable and does not yield under the maximum amount of forces that act on the [s/c](#) throughout the mission.



### 10.3.4 Total Deformation

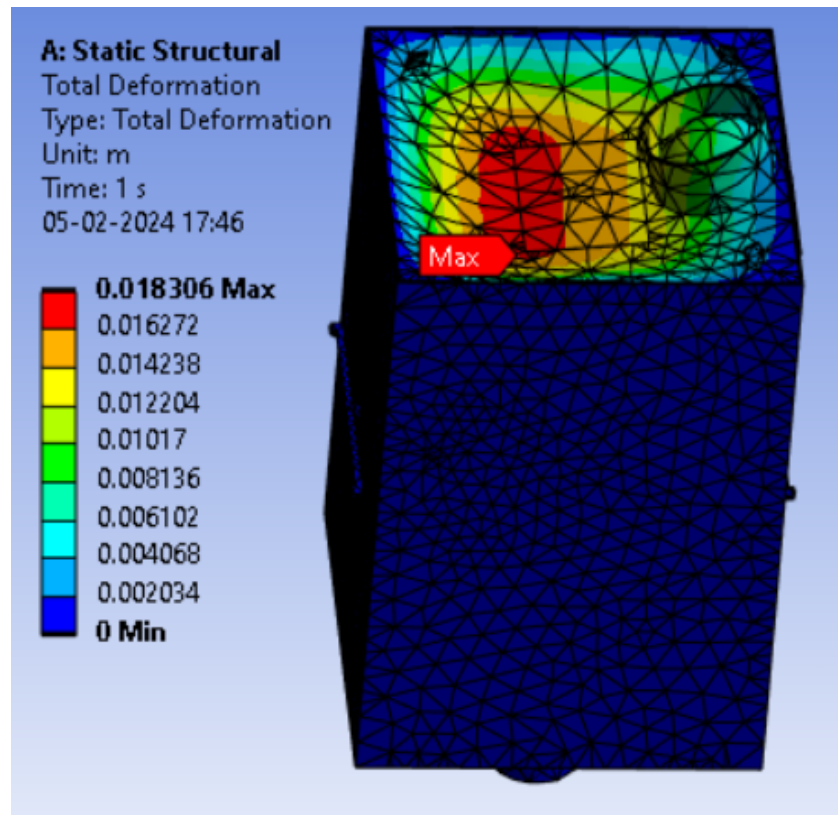


**Figure 10.6:** Total Deformation

A maximum deformation of 18.306 mm was found on the surface experiencing the maximum amount of stress.

The static structural analysis should however be followed with structural load testing before moving forward with the launch.

## 10.4 Science Mode Damping System

In this section, an active damping system using a piezoelectric smart material was developed. The goal was to provide accuracy to the payload while the spacecraft is in eclipse and the payload is doing observations as any unwanted vibrations during the science mode can reduce the efficiency of the observation ultimately hampering the primary goal of the Luminous mission.

For this active damping system, the choice was a piezoelectric actuator(sensor-actuator coupled together), the reason being that it can provide active damping which means it can generate vibrations in the opposite direction of the received vibrations and suppress them before they can reach the payload.

The choice for the piezoelectric material was Polyvinylidene Flouride ([PVDF](#)) as it has a good piezoelectric strain coefficient value and provides good tip deflection[[67](#)], its properties are discussed below:

- Elastic modulus ( $E$ ) =  $2.0 * 10^9 N/m^2$
- Poisson's ratio ( $\nu$ )= 0.29
- Shear modulus ( $G$ ) =  $0.775 * 10^9 N/m^2$
- Piezoelectric strain coefficients:  $d_{31} = 2.2 * 10^{-11}$  ,  $d_{33} = -3.0 * 10^{-11}$
- Operating Voltage: 50-2000 volts [[67](#)]
- Operating temperature range: (-20, +140) degree celsius [[67](#)]



The actuator has dimensions of 0.035 meters in length and 0.01 meters in height and is shown in [Figure 10.7](#)

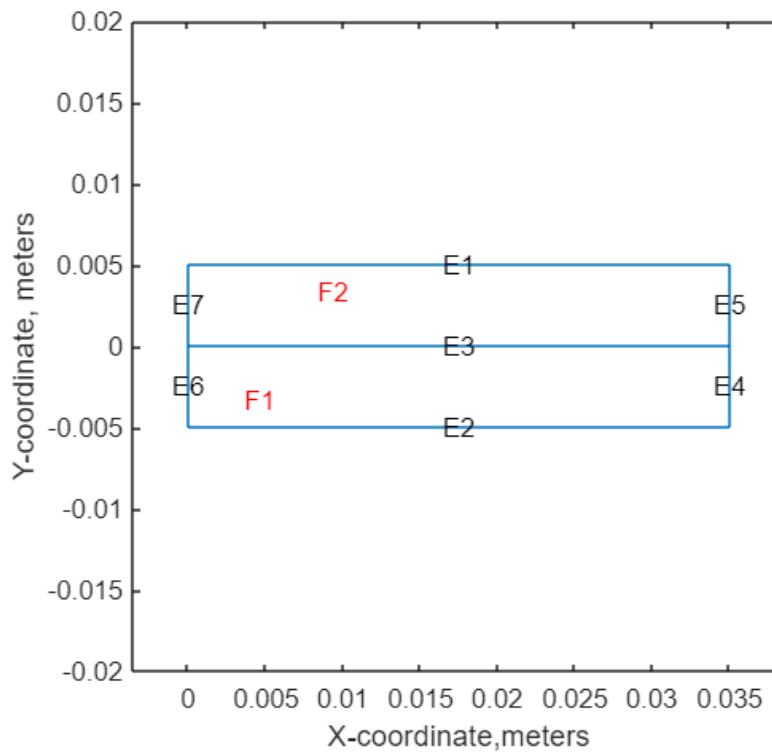


**Figure 10.7:** Piezoelectric Actuator model

The piezoelectric sensor-actuator coupled system works in such a way that the sensor can generate electric potential after sensing the frequency of the vibrations received by the system and hence, the actuator was placed under various electric potential fields from 60 volts to 180 volts with the bottom surface being fixed at 0 volts as shown in [Figure 10.8](#) which shows the top surface at a potential of 100 volts and the bottom surface at a potential of 0 volts.

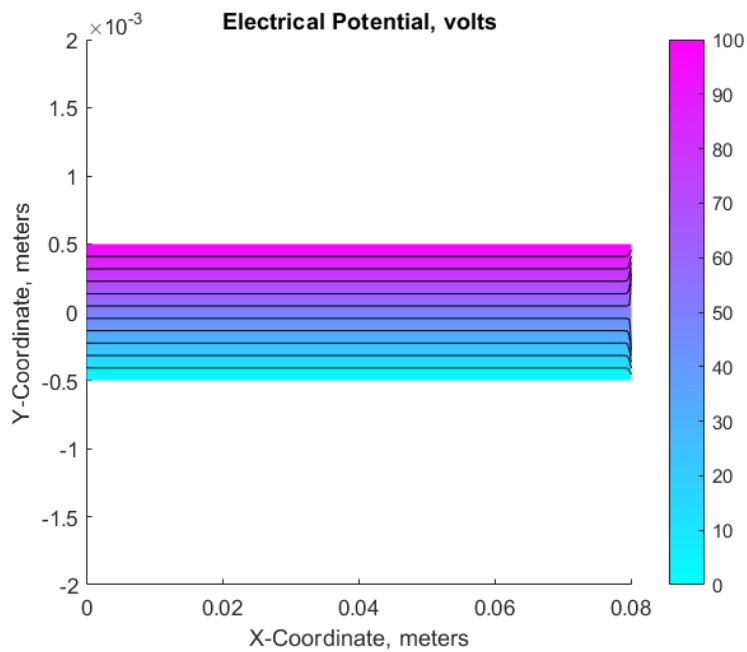


**Figure 10.8:** Flow of electric potential along the piezo y-direction

The y-tip deflections were calculated for the various changes in electric potential, the results of which can be seen in [Figure 10.9](#), [Figure 10.10](#) & [Figure 10.11](#)

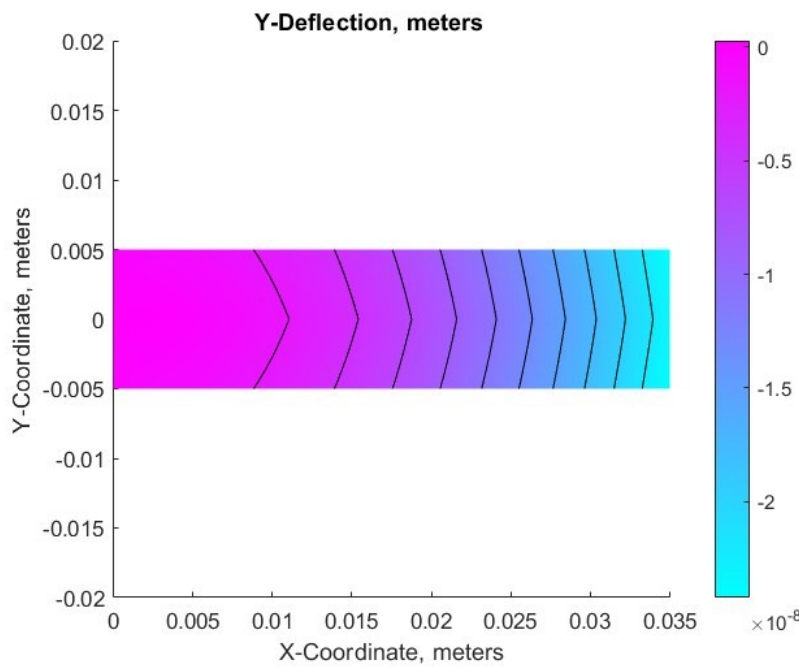


**Figure 10.9:** Tip deflection for 60 volts

- The tip deflection is  $2.4255 * e^{-8}$  in negative Y-direction

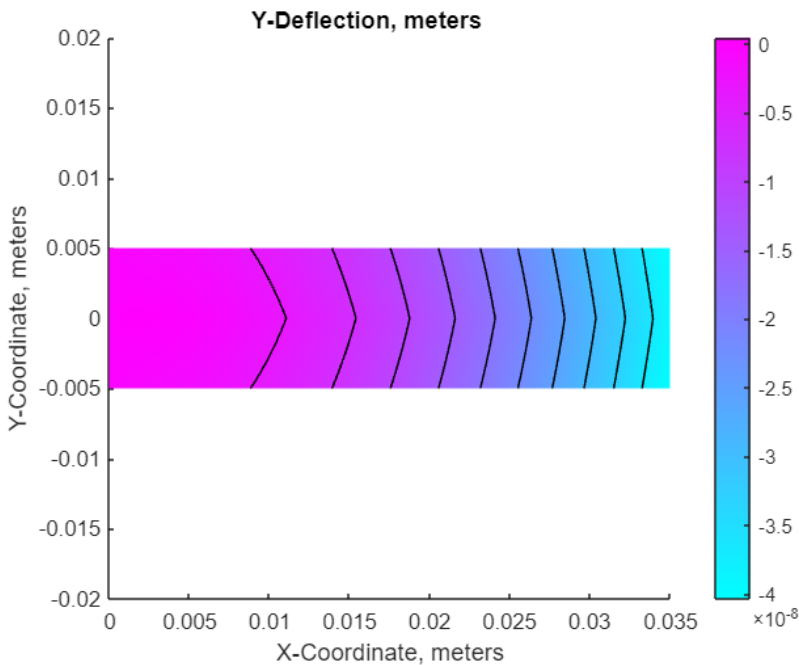


**Figure 10.10:** Tip deflection for 100 volts

- The tip deflection is  $4.0425 * e^{-8}$  meters in the negative Y-direction

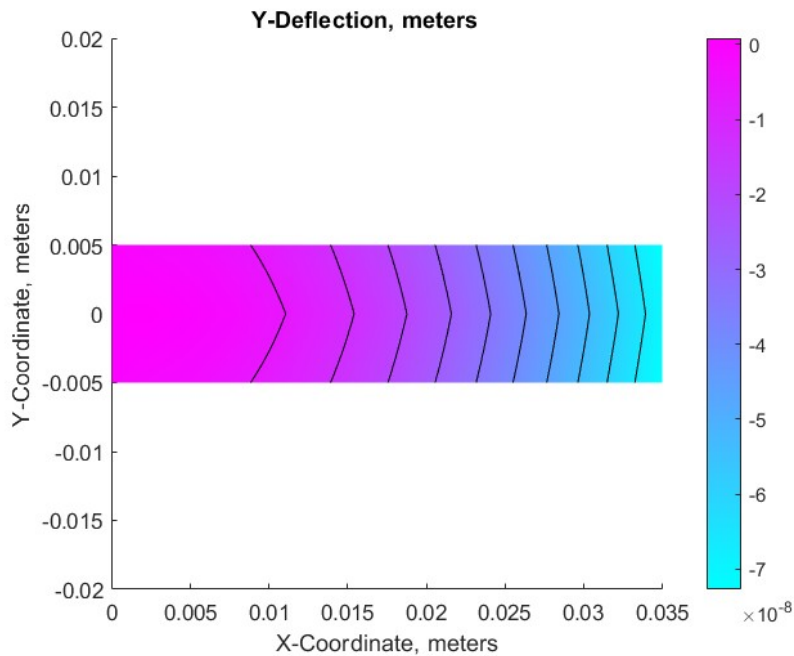


Figure 10.11: Tip deflection for 180 volts

- The tip deflection is  $7.2765 * e^{-8}$  in negative Y-direction

Thus these deflections can be used to generate vibrations in the direction opposite to the received vibrations which would suppress them before they reach the payload and in this way, the observation is carried out without any external disturbances.

#### 10.4.1 Effect on the EPS subsystem

Providing such a high voltage of 180 volts, not to mention 2000 volts which is the operating end voltage of our selected actuator is impossible for the [EPS s/s](#). Thus this constraint was solved by using a Piezoelectric amplifier which amplifies a very low input voltage and supplies a much higher voltage to the actuator in use in order to generate deflections.

The choice of the amplifier was the Low Cost-Piezo Linear Amplifier designed by Piezo Systems, Inc. [68], the reason being

- Only requires a 10-15 volts DC input & 0.7 amperes current at full load
- Gives a 180 volts peak output voltage & provides input and output protection against shorting, turn-on, turn-off, and load-generated voltage occurrences that can damage either the amplifier or the actuator.

The model describing the above amplifier is the EPA-007-012 as shown in [Figure 10.12](#) and its datasheet is provided in [68]



Figure 10.12: EPA-007-012 Piezoelectric amplifier

# Chapter 11 FDIR, Development Plan and Cost Estimation

This chapter aims to highlight the criticalities of the mission in every phase and of each subsystem. From this starting point, it is then possible to provide an initial assessment of the development plan for the subsystems of the mission. With this objective in mind, the phases and subsystems are studied for the possible failures and their consequences, so that a solution can be found. It is important to keep in mind that this chapter is not comprehensive of all possible failures of the mission and instead focuses on the possible "expected" failures.

## 11.1 Fault Detection, Identification, and Recovery

### 11.1.1 Mission criticalities

In the following list, the main phases of the mission are presented with their criticalities and possible failures. Possible solutions are also presented.

- LAUNCH: Launch is always critical, a failure in this phase results in a failure of the mission. Possible failures are related to the launcher and are therefore not under the control of the mission developer.  
Possible solutions: Choice of a trusted and proven launcher and launch organization, such as [ESA](#).
- VERIFICATION: The phase of verification of the subsystems is critical. In case of a failure of the verification of non-essential components, the mission can proceed; In case of a failure in the payload or critical components, the mission fails.  
Possible solutions: Higher reliability of the essential components, reached through intensive testing on the models.
- TRANSFER: The transfer phase is critical, failure of transfer is a failure for the mission. The transfer fails if the main engine is not fired or is fired incorrectly.  
Possible solutions: In case of incorrect transfer/operational orbit insertion, the mission control can recover navigation data and correct the course using the main engine. To avoid failure in firing we can ask for higher reliability of the main engine, reached through intensive testing on the models.
- STATION KEEPING: Station keeping is not critical. Due to the choice of the operational orbit, a failure to [SK](#) does not result in a failure of the mission, but rather in reduced observation opportunities.  
Possible solutions: Higher reliability of the main engine, reached through intensive testing on the models. [SK](#) could also be performed through the [ADCS](#) thrusters, but this would require a choice of more powerful thrusters.
- DECOMMISSIONING: Decommissioning is not critical for the success of the mission, however, it's critical for the credibility of the mission and mandatory per international treaties, therefore failure to decommission is considered a partial failure of the mission and shall be avoided.  
Possible solutions: Higher reliability of the main engine, reached through intensive testing on the models.

### 11.1.2 Subsystems criticalities

In the following list, the subsystems are presented with their possible failures. The redundancies are considered as a solution and presented as such. The critical components of the subsystem are highlighted to understand the choices of the development plan better.

- **TTMTC:** [TTMTC](#) is critical for the mission success. The system is reliant on Lunar Gateway for the Safe Mode emergency signal and is independent of [ADCS](#). In case of [HGA](#) failure, the [LGAs](#) can still dump all data to Lunar Gateway, using more power. In case of failure of up to 2 LGAs, redundancy assures data transfer. The placement of the components is such that communication (either directly with Earth or through a relay) is possible at every orbit.



Criticalities: **LGA**s are more critical than the **HGA**, since they can ensure the success of the mission even without the **HGA**. **HGA** does not have redundancy and shall be tested more.

- **ADCS:** **ADCS** is critical for the mission and is well redundant in all its components. This configuration ensures in any case that single-point failure can't happen. Losing one set of sensors (Sun, IMU, or Star trackers) would still mean that the attitude can be recovered from the other 2 sets, therefore the subsystem accepts the failure of an entire set of sensors. Actuators have redundancies but can't work in case of an entire set failure.

Criticalities: The actuators are more critical than the sensors because they can't fail beyond the redundancy, therefore their testing shall be stricter.

- **EPS** One battery is redundant to cover possible failures during the mission. Each battery has a redundant cell. Solar arrays and **SADA** systems are not redundant and are critical, but solar arrays present a redundant string. **PCDU** is the most critical component of the **EPS** therefore it is subject to strict testing and has a redundancy to avoid failure of the mission.

Criticalities: The subsystem has a single-point failure, therefore intense testing has to be done before the mission to avoid failure to deploy and failure to rotate the solar panels. This failure would result in the end of the mission.

- **TCS TCS** is critical for the mission. The subsystem is not redundant but well-margined for the operational temperatures, the system is also completely passive.

Criticalities: In case of failure the system will overheat, therefore just like for the **EPS**, it shall be subject to strict testing.

- **PS:** The propulsion system has redundancies in the tanks and valves. There is no redundancy for the primary engine, as well as for the secondary engines. Failure of the main engine before the transfer would result in failure of the mission. Failure in station keeping would result in loss of observations, and failure in decommissioning would result in loss of credibility, but not complete failure of the mission.

Criticalities: The necessity for a transfer means that failure is unacceptable for the engine and intense testing must be done, while less critical tests can be applied to the tanks and valves since they have redundancies. The secondary engines are still considered for intense testing since even partial failure of the mission would be detrimental.

- **OBDH:** **OBDH** is critical for the mission. The Guidance, Navigation and Control (**GNC**) algorithm shall not fail before reaching operational orbit to avoid mission failure and should not fail once in operational orbit to allow the station keeping operations. Memories and processors will certainly have redundancies as well as ample margins to avoid losing data.

Criticalities: Since all data has to pass through this subsystem, the **OBDH** shall be the most tested subsystem, on par with the payload

- **PL:** The payload is the heart of the mission. Failure of the payload means the end of the mission. NO failure accepted. Multiple qualification models are suggested.

Criticalities: The payload is not developed by us but shall be strictly tested and protected during the mission, using sun sensors and a sturdy structure.

- **ROBOTICS:** Robotics are partly fundamental for the success of the mission and do not present redundancies. The **SADA** system is fundamental for the success of the mission and allows no failure.

Criticalities: The **SADA** shall be tested strictly with multiple models and a qualification model.

- **STR:** Structures will be tested in the assembly and can therefore be less tested during the subsystem build to avoid unnecessary testing.

Of course, an assembly of all the subsystems is fundamental to test before flight and shall undergo testing for both functionality and qualification model.

## 11.2 Development plan

In the Table 11.1 we can see the development plan for the various subsystems' components. Keep in mind that almost all the components have flight heritage and a **TRL** of 9, therefore they are already qualified. Despite this, the development plan suggests ulterior models to be tested based on the criticality of each component.



Subsystem	Component	TRL	BreadBoard	Virtual Model	Structural-Thermal Model	Engineering Model	Qualification Model	ProtoFlight Model
TTMTC	Low gain antenna (with transceiver)	9						
	High gain antenna (with transmitter)	9						
EPS	Battery	9						
	Solar Array	9						
	PCDU	9						
PS	Primary propulsion: LEROS-1B	9						
	Station keeping thrusters DST-11H	9						
PL	Oxidizer tank	9						
	Fuel tank	9						
	Pressurant tank	9						
ADCS	Coronograph	4 (Estimation)						
	Reaction wheel	9						
	Attitude control: Monarc-5	9						
TCS	Coarse Sun Sensor	9						
	Fine Sun Sensor	9						
	Star Tracker	9						
OBDH	IMU	9						
	Radiator	9						
	MLI	9						
STR	OBC	9						
	Harness	4						
ROBOTICS	Solar Array Drive Assembly	9						
	Assembly of components	4						

**Table 11.1:** Development plan for the components

## 11.3 Preliminary Cost Estimation

A preliminary cost estimation has been conducted to complement this feasibility study. The costs can be divided into costs related to the *s/c* itself, to the mission payloads, and to the selected launcher. The three of them will be briefly assessed in this section and a final cost breakdown will be shown. All the adopted methods can be found in the "New SMAD" book [45] with a more detailed explanation. Please note that all costs provided by these methods are in 2010 USD\$: they will be adjusted to 2024 USD\$ in the final cost breakdown.

### 11.3.1 Spacecraft

The spacecraft's cost estimation is based on the QuickCost method. This approach, developed for NASA projects in 2010, can be applied to unmanned robotic vehicles and it is based on historic cost data. This tool can provide the full program costs, from development up to the first flight unit, based on a few relevant parameters, which are available already at an early development phase. Both recurring and non-recurring costs, as well as contractor plus government costs, are included. The following Equation 11.1 is used to retrieve the cost of the vehicle's development:

$$\begin{aligned} Cost_{sc} = & 2.829 \cdot (DryMass^{0.457}) \cdot (Power^{0.157}) \cdot (2.718^{0.171 * Data\%}) \cdot (2.718^{0.00209 * Life}) \\ & * (2.718^{1.52}) \cdot (2.718^{0.258}) \cdot (2.718^{0.467 * InstrComp\%}) \\ & \cdot \frac{1}{2.718^{0.0145 \cdot (Year - 1960)}} \cdot \frac{1}{2.718^{0.237 \cdot Team}} \quad (11.1) \end{aligned}$$

The values needed to obtain the cost estimation are:

- "Dry Mass": The dry mass of the Luminous *s/c*, instruments included.
- "Power": The **BOL** power in Watts of the *s/c*.
- "Data%": A parameter connected with the data rate required by the mission. A value lower, equal or higher than 0.5 should be selected respectively for low, medium, and high data rate missions.
- "Life": Expected mission duration in months, extended operations excluded.
- "New": A parameter to take into account innovative/new technologies. It can range between 28% to 130%.
- "Planetary": to discriminate between Earth-orbiting missions and planetary missions. The values to be assigned are respectively 0 for the first type and 1 for the second type. Luminous is considered a planetary mission.
- "Year": refers to the "Authority to proceed" year. In theory, the most recent value should be 2005, but we used 2024. This choice impacts the final cost estimation, so its feasibility must be verified.



- "InstrComp%": this parameter takes into account the instrument complexity, from 0% to 100%.
- "Team": a parameter to evaluate the team experience, from 1 (unfamiliar) to 4 (extensive).

In the following Table 11.2 the selected values for the above parameters are reported:

Cost Driver	Luminous
DryMass	402.28 kg
Power	1112.6 W
Data%	0.5
Life	72 months
New	0.6
Planetary	1
Year = 2024;	2024
InstrComp%	0.5
Team	1

**Table 11.2:** *QuickCost Model inputs*

A 2% margin on the [Equation 11.1](#) output will be added to consider also PhaseA costs, while an additional 9% is needed for retrofitting of an existing Ground Station ([GS](#)) facility, terminals and software.

### 11.3.2 Payloads

The cost model adopted for the payload is the NASA Instrument Cost Model ([NICM](#)), developed by the Jet Propulsion Laboratory ([JPL](#)). This model predicts the non-recurring costs of development and the construction costs of one flight model. Contractors' fees are included. The payloads are divided into five categories: the one of interest for Luminous is the one of optical planetary payloads. For these instruments, the statistical formula for the cost estimation is the following [Equation 11.2](#):

$$Cost_{pl} = 328 \cdot Mass^{0.426} \cdot Power^{0.414} \cdot Life^{0.375} \quad (11.2)$$

where:

- "Mass" is the total mass of the instrument in kg
- "Power" is the maximum power required in Watts
- "Life" is the design life of the payload in months

In the following Table 11.3 are stored the characteristic values for both primary and payloads:

Cost Driver	Primary Payload	Secondary Payload
Mass	25 kg	35 kg
Power	22.5 W	22 W
Life	72 months	72 months

**Table 11.3:** *NICM Model inputs*

### 11.3.3 Primary launcher

The primary launcher selected for the Luminous mission is the Falcon9, as detailed in [section 2.7](#). The average launch cost for a Falcon9 is 56.75 million 2010 USD\$ [[45](#)].



### 11.3.4 Results

All the budget costs presented in the sections above need to be actualized to 2024 USD\$. To do so, they shall be multiplied by the inflation, which is equal to 41.4% from 2010 to 2024 [69].

The overall cost budget is reported in the following [Table 11.4](#):

Item	Cost (in million 2024 USD\$)
Spacecraft	332.25
Primary Payload	32.88
Secondary Payload	32.88
Launch	80.02
Total	478.03

**Table 11.4:** Overall Costs, in 2024 million USD\$

Note that the costs of the primary and secondary payloads are equal. This is due to the very small difference between the two, as shown in [Table 11.3](#).

# Chapter 12 System budgets

Hereafter are presented the summarized mass and power budgets, divided per subsystem to better highlight the importance and impact of each one on the mission. It is important to remember that these are reference values taken from already produced and tested components. Therefore, they are subject to margins to account for the possible variation in mass and power during the further stages of mission development.

## 12.1 Mass budget

Subsystem	Component	Quantity (+ redundant)	Mass [kg]	Design Maturity Margin [%]	Total mass [kg]
TMTC	Low Gain Antenna	3	0.44	5	1.37
	High Gain Antenna	1	3	5	3.15
EPS	PCDU	1(1)	12	5	25.20
	Battery	3(1)	4.50	5	18.90
	Solar cells	2	1.58	5	3.32
PS	Primary thruster	1	4.30	5	4.52
	Secondary thruster	4	0.77	5	3.23
	Oxidizer tank	1	2.10	10	2.12
	Fuel tank	4	0.62	10	2.43
	Pressurant tank	1	2.25	10	2.27
PL	Coronograph	1	25	20	30
	SMEI	1	25	20	30
ADCS	Reaction wheel	3(1)	5	5	21
	Attitude thruster	6(2)	0.49	5	4.12
	Fine Sun Sensor	1(1)	0.04	5	0.07
	Coarse Sun Sensor	2(2)	0.11	5	0.46
	Star tracker	1(1)	0.27	5	0.57
	IMU	1(1)	6.50	5	13.65
TCS	Radiator	1	13.01	5	13.66
	MLI	1	1.20	5	1.26
ROB	SADA	2	4.90	5	10.29
OBDH	CPU & Memories	1	TBD	10	15
STR	Harness	1	TBD	10	95

**Table 12.1:** Mass budget per component



Total dry mass [kg]	20% SLM [kg]	Total dry mass+SLM [kg]	Total wet mass [kg]	Adapter mass [kg]	Launch mass [kg]	25% launch level margin [kg]	Total launch mass [kg]
336.14	67.23	403.37	813.78	111.69	925.47	231.37	1156.84

Table 12.2: Margined dry, wet and launch masses

## 12.2 Power budget

Subsystem	Component	Quantity (+ redundant)	Max power [W]	Design Maturity Margin [%]	Total power [W]
TMTC	Low Gain Antenna	3	3.5	5	11.02
	High Gain Antenna	1	10.5	5	11.02
EPS	PCDU	1(1)	21	5	44.10
	Battery	3(1)	82	5	344.40
PS	Primary thruster	1	32	5	33.60
	Secondary thruster	4	41	5	86.10
PL	Coronograph SMEI	1 1	22.50 16	20 20	27 19.20
ADCS	Reaction wheel	3(1)	40	5	168
	Attitude thruster	6(2)	18	5	151.20
	Fine Sun Sensor	1(1)	0.32	5	0.66
	Coarse Sun Sensor	2(2)	0.19	5	0.78
	Star tracker	1(1)	1.50	5	3.15
	IMU	1(1)	6	5	12.60
ROB	SADA	2	8.60	5	18.92
	Solar array deployment mechanism	2	10	10	22
OBDH	CPU & Memories	1	20	10	22

Table 12.3: Peak power budget per component

DETUMBLING MODE		
SUBSYSTEM	COMPONENT	POWER [W]
ADCS	Reaction wheels	168.00
	IMU	6.30
OBDH	CPU & Memories	11.00
EPS	PCDU	21.00
TOT [+20%]		247.56

Table 12.4: Detumbling mode peak power budget



DEPLOYMENT MODE		
SUBSYSTEM	COMPONENT	POWER [W]
ADCS	Reaction wheels	168.00
	IMU	6.30
	Star sensor	1.58
	Sun sensor	0.99
OBDH	CPU & Memories	11.00
EPS	PCDU	21.00
TMTC	Low Gain Antennae	0.21
STR	Deployment mechanism	22
TOT [+20%]		283.63

**Table 12.5:** Deployment mode peak power budget

CHARGING MODE		
SUBSYSTEM	COMPONENT	POWER [W]
ADCS	Reaction wheels	168.00
	IMU	6.30
	Star sensor	1.58
OBDH	CPU & Memories	11.00
EPS	PCDU	21.00
	Battery	86.10
TMTC	Low Gain Antennae	7.35
STR	SADA	18.82
TOT [+20%]		384.29

**Table 12.6:** Charging mode peak power budget

SAFE MODE		
SUBSYSTEM	COMPONENT	POWER [W]
ADCS	Reaction wheels	168.00
	IMU	6.30
OBDH	CPU & Memories	11.00
EPS	PCDU	21.00
TMTC	Low Gain Antennae	7.46
STR	SADA	18.82
TOT [+20%]		279.21

**Table 12.7:** Safe mode peak power budget



SCIENCE MODE		
SUBSYSTEM	COMPONENT	POWER [W]
ADCS	Reaction wheels	168.00
	Sun sensor	0.33
	Star sensor	1.58
	IMU	6.30
OBDH	CPU & Memories	11.00
EPS	PCDU	21.00
TMTC	Low Gain Antennae	7.46
STR	SADA + piezo amplifier	24.20
PL	Coronograph + SMEI	46.20
<b>TOT [+20%]</b>		<b>343.27</b>

**Table 12.8:** Science mode peak power budget

NORMAL ON-STATION MODE		
SUBSYSTEM	COMPONENT	POWER [W]
ADCS	Reaction wheels	168.00
	Star sensor	1.58
	Sun sensor	0.33
	IMU	6.30
OBDH	CPU & Memories	11.00
EPS	PCDU	21.00
TMTC	Low Gain Antenna	7.35
STR	SADA	18.92
PL	SMEI	19.20
<b>TOT [+20%]</b>		<b>304.41</b>

**Table 12.9:** Normal on-station mode peak power budget

MANOEUVERING MODE		
SUBSYSTEM	COMPONENT	POWER [W]
ADCS	Reaction wheels	168.00
	Sun sensor	0.33
	IMU	6.30
OBDH	CPU & Memories	11.00
EPS	PCDU	21.00
TMTC	Low Gain Antenna	7.35
<b>TOT [+20%]</b>		<b>362.38</b>

**Table 12.10:** Manoeuvring mode peak power budget



TELECOMMUNICATION MODE		
SUBSYSTEM	COMPONENT	POWER [W]
ADCS	Reaction wheels	168.00
	Star sensor	1.58
	IMU	6.30
OBDH	CPU & Memories	11.00
EPS	PCDU	21.00
TMTC	High Gain Antenna	11.03
STR	SADA + piezo amplifier	24.20
PL	SMEI	19.20
TOT [+20%]		314.76

**Table 12.11:** *Telecommunication mode peak power budget*

# List of Figures

1.1 CAD image of the Compact CORonograph, including obscurer . . . . .	2
1.2 Sunspot number prediction up to 2032 . . . . .	3
1.3 Solar Radio Flux (10.7 cm) prediction up to 2042 . . . . .	4
1.4 Perturbation accelerations for a lunar orbiter . . . . .	4
1.5 Lunar wake phenomena . . . . .	5
1.6 Plasmasphere density vs distance from the surface of Earth for nearly-equatorial orbits . . . . .	6
1.7 GCR worst case scenario . . . . .	8
2.1 Sketch of the reconstruction of the Moon disk image . . . . .	2
2.2 Example of image reconstruction during an eclipse passage - the Sun disc is visible just for clearness. . . . .	2
2.3 Example of image reconstruction during eclipse passage - the Sun disc is visible just for clearness. . . . .	3
2.4 Example of image reconstruction during eclipse passage from orbits around $L_4/L_5$ Lagrangian points - the Sun disc is visible just for clearness. . . . .	4
2.6 Three selected SPOs . . . . .	5
2.7 Example of image reconstruction during eclipse passage from orbits at 9 Moon radii. . . . .	6
2.8 Initially 16 Moon radii orbit, which leaves the Moon in just 5 revolutions. . . . .	7
2.9 Example of a circular orbit passing through the eclipse cone. Its inclination alone would not be sufficient to make it intersect the Moon's shadow; its RAAN - aligned with the direction of the Sun - guarantees the eclipse passage. . . . .	7
2.10 Evolution of the inclination of different Moon orbits . . . . .	8
2.11 Front view of the 2D sketch of the eclipse cone . . . . .	8
2.12 RAAN's evolution of different moon's orbit vs Sun-Moon movement . . . . .	9
2.13 Parameters' evolution for retrograde 11 Moon radius orbit . . . . .	10
2.14 360° view of the solar corona as a function of orbital parameters for an $11R_{MOON}$ orbit . . . . .	10
2.15 Duration of the observation of the inner corona up to $5 R_{sun}$ . . . . .	11
2.16 Observation zones as a function of orbital parameters . . . . .	11
2.17 Applied example of the SK strategy: evolution of RAAN and inclination . . . . .	12
2.18 Applied example of the SK strategy: eclipse passages observational quality . . . . .	12
2.19 Best transfer for 2027 . . . . .	14
2.20 Example of an "optimized" natural propagation . . . . .	16
2.21 Impact regions . . . . .	17
2.22 Impact in Middle Southern region . . . . .	17
2.23 Impact in Northern region . . . . .	18
2.24 Phases A through D . . . . .	20
2.25 Phase E . . . . .	20
2.26 Phases E and F . . . . .	21
2.27 First half of typical orbit . . . . .	21
2.28 Second half of typical orbit . . . . .	22



3.1 Visualization of <b>Out-Of-Eclipse</b> target attitudes with respect to the celestial bodies. The <b>green</b> face hosts the HGA and its outer normal is $-\hat{\mathbf{X}}$ . The <b>blue</b> face hosts the payload and its outer normal is $\hat{\mathbf{Y}}$ . The <b>yellow</b> panels represent the solar arrays, which can rotate around $\hat{\mathbf{Z}}$ axis. . . . .	24
3.2 Example of the computational error due to spacecraft conjunction with Moon and Sun during Out-Of-Eclipse phase (Proposal <b>B</b> ). The vertical dotted green lines show the boundaries of the identified problematic time interval. The $\hat{\mathbf{X}}$ body frame is not plotted since in the Proposal <b>B</b> it is the well-defined axis. . . . .	26
3.3 Example of the ideal angular profile to be commanded to the SADA . . . . .	28
3.4 Example of the accumulation of angular momentum in the RW . . . . .	29
4.1 Propulsion system architecture . . . . .	33
5.1 The locations of the Deep space ground station network of the ESA (Number 4, 5, and 6 of Blue column) . . . . .	40
5.2 Left: S-band antenna for Low Rate Data, right: X-band Bepicolombo antenna . . . . .	42
6.1 Power source vs lifetime . . . . .	47
6.2 Overview of solar cells efficiency evolution . . . . .	48
6.3 Overview of principal solar cells technologies . . . . .	48
6.4 Specific energy vs specific density for batteries . . . . .	50
6.5 Voltage and power evolution during charging . . . . .	54
7.1 Heating environments . . . . .	56
7.2 Thermal Network . . . . .	57
7.3 Typical MLI stacking arrangement. The schematic cross-section depicts the key elements of an MLI blanket. Not all elements need to be present in every design. [57] . . . . .	58
8.1 Reference ESA architecture . . . . .	62
8.2 Preliminary data budget . . . . .	63
9.1 LASCO Payload's dimensions (300x340x1350 mm) . . . . .	65
9.2 Final spacecraft configuration . . . . .	66
9.3 In Red:Primary Payload [3] in Blue: Secondary Payload [4] . . . . .	67
9.4 Propulsion module . . . . .	68
9.5 Comparison between 2, 3 and 4 tanks configuration . . . . .	69
9.6 Electrical components internal disposition . . . . .	70
9.7 CoG position . . . . .	71
9.8 Antennas and OBDH . . . . .	71
9.9 General view of all actuators/sensors present in the spacecraft . . . . .	73
9.10 Launch configuration and CoG height [65] . . . . .	73
10.1 Frequency Vs. SPL . . . . .	76
10.2 Active Vibration Isolation System . . . . .	77
10.3 Real model Vs. Simplified model for analysis . . . . .	78
10.4 Equivalent Von Mises stress . . . . .	78
10.5 Safety Factor . . . . .	79
10.6 Total Deformation . . . . .	80
10.7 Piezoelectric Actuator model . . . . .	81
10.8 Flow of electric potential along the piezo y-direction . . . . .	81
10.9 Tip deflection for 60 volts . . . . .	82



10.10 Tip deflection for 100 volts . . . . .	82
10.11 Tip deflection for 180 volts . . . . .	83
10.12 EPA-007-012 Piezoelectric amplifier . . . . .	83
A.1 Worst week case for solar protons . . . . .	99
A.2 Worst week case for solar alpha particles . . . . .	100
A.3 Worst day case for solar protons . . . . .	101
A.4 Worst day case for solar alpha particles . . . . .	102
A.5 Worst 5 min case for solar protons . . . . .	103
A.6 Worst 5 min case for solar alpha particles . . . . .	104
B.1 View Factor between two perpendicular surfaces with an infinite extension in the direction normal to the paper . . . . .	109
D.1 AzurSpace 3G30C cells datasheet . . . . .	112
D.2 EaglePicher LP32975 cells datasheet . . . . .	113
D.3 Moog Type 1 SADA datasheet . . . . .	113
D.4 Magellan Aerospace PCDU datasheet . . . . .	114
E.1 Daeil systems isolator datasheet . . . . .	115
F.1 Leros 1c datasheet . . . . .	116
F.2 Secondary bipropellants datasheet . . . . .	117
F.3 Monopropellants datasheet . . . . .	117
G.1 RAD750 PowerPC microprocessor datasheet . . . . .	119
G.2 RAD750 6U CompactPCI single-board computer datasheet . . . . .	119

# List of Tables

1.1	Comparison of existent coronagraphs and LUMINOUS . . . . .	1
1.2	Sun and geomagnetic activity indexes for mission design . . . . .	6
1.3	Effects, their model and reference requirements from [9] . . . . .	7
1.4	Worst case scenario for the modeling of the outer magnetosphere . . . . .	8
1.5	Solar wind parameters (mean and 2- $\sigma$ ) . . . . .	8
2.1	SPO advantages and disadvantages . . . . .	5
2.2	Hours of observation time in terrestrial months for each family . . . . .	5
2.3	SK strategy controlling the inclination - costs . . . . .	8
2.4	SK strategy results . . . . .	12
2.5	SK strategy results: full-Corona observation . . . . .	13
2.6	SK strategy results: Inner corona observations . . . . .	13
2.7	Available transfers . . . . .	14
2.8	Launchers' trade-off . . . . .	19
3.1	The specifications of the IMU . . . . .	23
3.2	The specifications of the Star Trackers . . . . .	24
4.1	Main characteristics of various propulsion system technologies [33] . . . . .	31
4.2	Propellant masses and volumes computed values . . . . .	35
4.3	Propellant masses and volumes computed values . . . . .	35
4.4	Propellant masses and volumes computed values . . . . .	36
4.5	Total propellant masses and volumes . . . . .	36
4.6	Parameters for calculations of the pressurization system . . . . .	37
4.7	Helium mass and volume computed values . . . . .	37
4.8	Density and yield strength of the 6Al-4V titanium alloy . . . . .	37
4.9	Tank parameters computed values . . . . .	37
5.1	Data Volume summarized . . . . .	38
5.2	The distance between Rx and TX in different phases of the mission . . . . .	38
5.3	The different link types, their communication operations, and their communications architecture . . . . .	39
5.4	The Frequency selection for different Links . . . . .	40
5.5	The Modulation selection for different Links . . . . .	40
5.6	The link budget calculation for different links . . . . .	43
5.7	Mass Budget for the System . . . . .	44
5.8	TTMTC Thermal Budget . . . . .	44
5.9	TTMTC Thermal Boundaries . . . . .	45
5.11	TTMTC Pointing Budget . . . . .	45
6.1	Power-timespan requirements for LUMINOUS mission . . . . .	46
6.2	EPS trade-off . . . . .	53
6.3	Solar arrays data . . . . .	53



6.4 Batteries data . . . . .	54
7.1 Overall temperature range . . . . .	55
7.2 Overall temperature range . . . . .	55
7.3 Most critical conditions for TCS . . . . .	57
7.4 Single-node analysis results . . . . .	57
7.5 View Factors . . . . .	59
7.6 TCS results . . . . .	59
7.7 Mass budget for the TCS . . . . .	60
8.1 Results of the sizing . . . . .	64
8.2 Processing partition between ADCS and OBDH . . . . .	64
11.1 Development plan for the components . . . . .	86
11.2 QuickCost Model inputs . . . . .	87
11.3 NICM Model inputs . . . . .	87
11.4 Overall Costs, in 2024 million USD\$ . . . . .	88
12.1 Mass budget per component . . . . .	89
12.2 Margined dry, wet and launch masses . . . . .	90
12.3 Peak power budget per component . . . . .	90
12.4 Detumbling mode peak power budget . . . . .	90
12.5 Deployment mode peak power budget . . . . .	91
12.6 Charging mode peak power budget . . . . .	91
12.7 Safe mode peak power budget . . . . .	91
12.8 Science mode peak power budget . . . . .	92
12.9 Normal on-station mode peak power budget . . . . .	92
12.10 Manoeuvring mode peak power budget . . . . .	92
12.11 Telecommunication mode peak power budget . . . . .	93
B.1 Planetary Properties . . . . .	105
B.2 Orbital data . . . . .	105
B.3 Spacecraft and material properties . . . . .	105
C.1 Maximum distances . . . . .	110

## Appendix A Solar particles

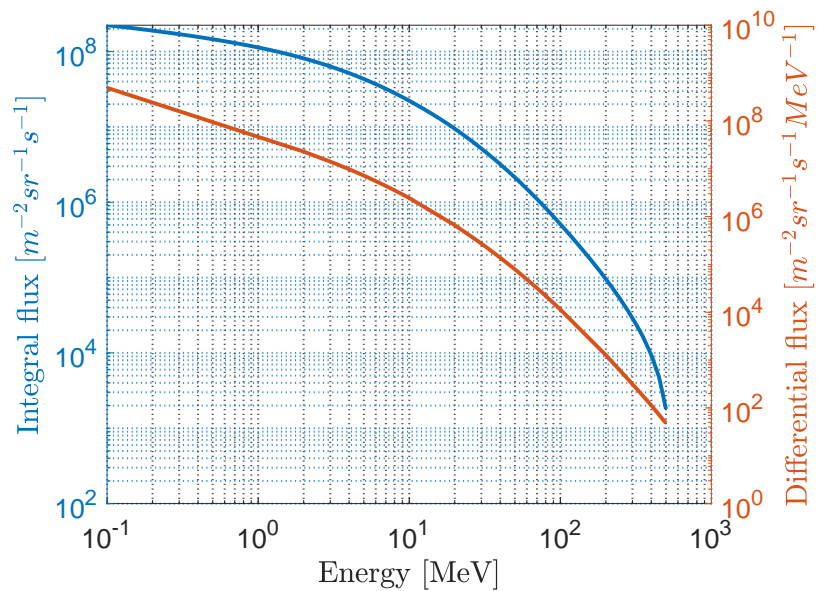


**Figure A.1:** Worst week case for solar protons

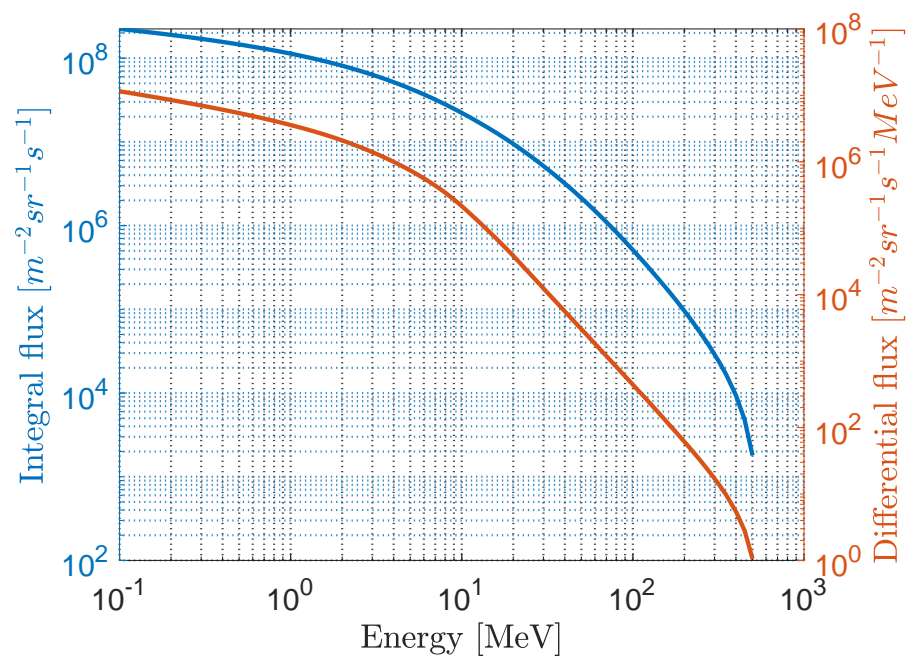


**Figure A.2:** Worst week case for solar alpha particles

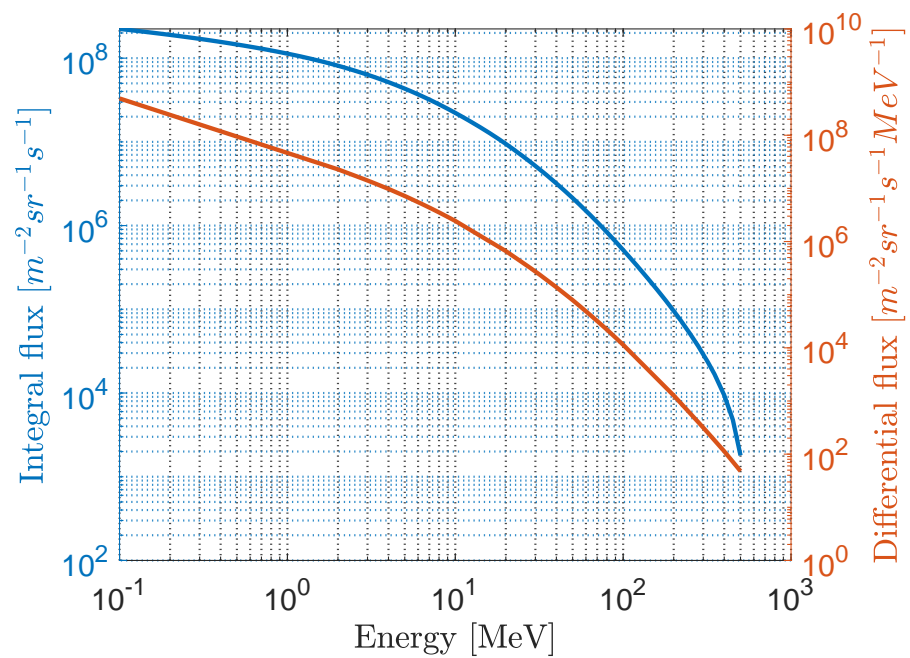


**Figure A.3:** Worst day case for solar protons

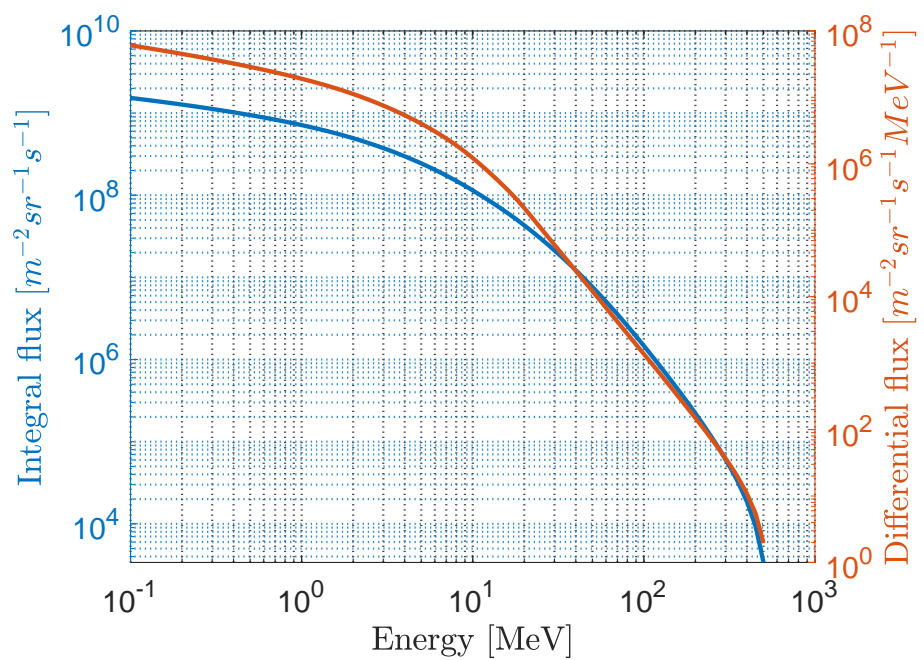


**Figure A.4:** Worst day case for solar alpha particles

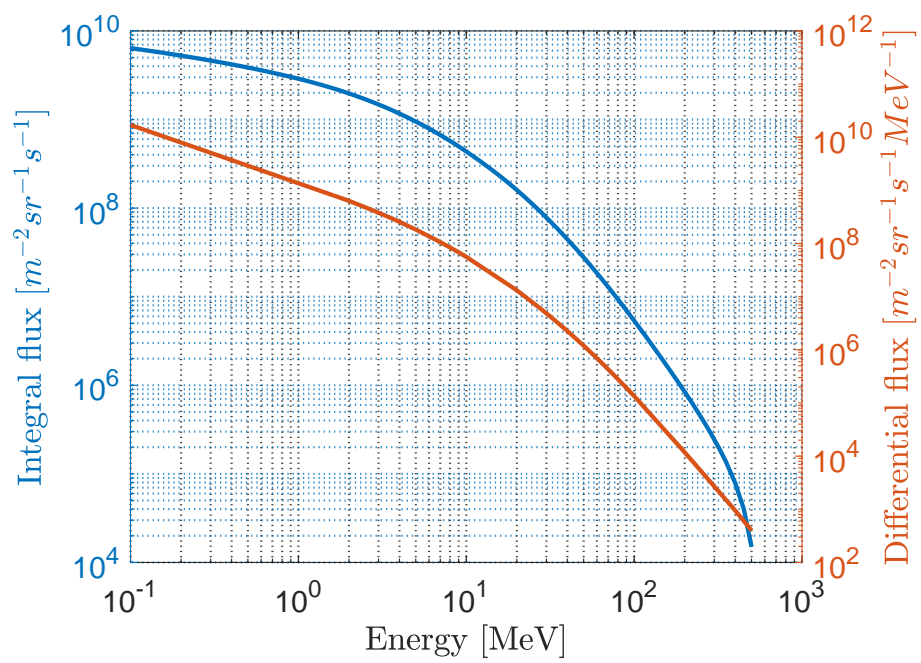


**Figure A.5:** Worst 5 min case for solar protons

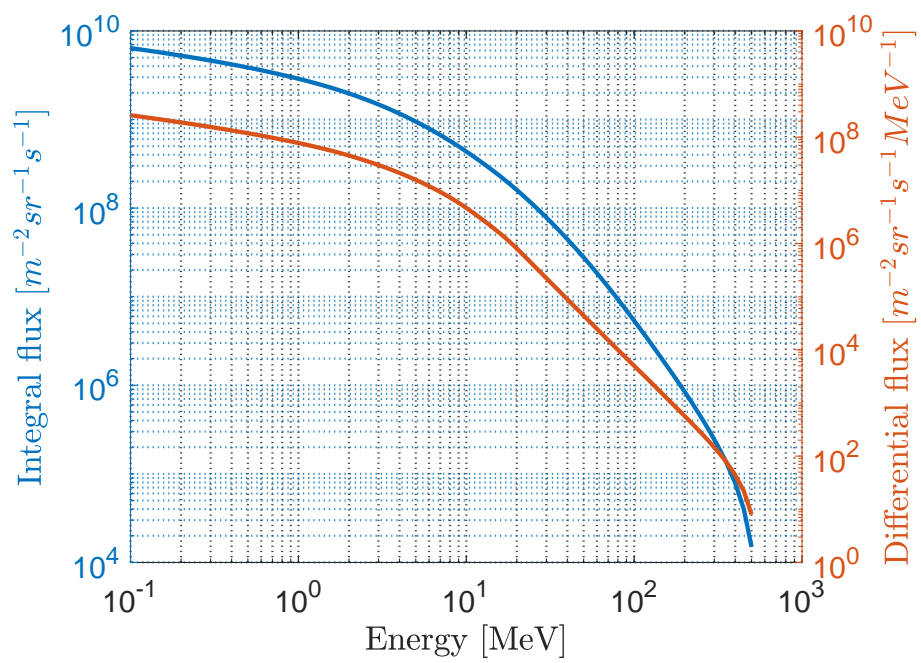


**Figure A.6:** Worst 5 min case for solar alpha particles

# Appendix B Thermal Control Subsystem

## B.1 TCS - Single Node Assumptions

### B.1.1 Planetary Data

The following table displays some data regarding the optical and thermal properties of the two bodies around which the mission will operate, the Earth and the Moon.

	Earth	Moon
Albedo	0.35	0.13
Emissivity $\epsilon$	0.95 [70]	0.75 [71]
Diffusion Factor	1	1
Surface Temperature	+15°C [72]	Bright Side: +197°C [71] Dark Side: -103°C [71]

**Table B.1:** Planetary Properties

### B.1.2 Orbital Data

Here are presented some data regarding the Earth-Moon system. Also the orbital data of the [s/c](#) are needed to compute the heat fluxes.

Quantity	
Mean Earth - Sun distance	1 AU
Mean Earth - Moon distance	384400 km
Earth Radius	6371 km
Moon Radius	1738 km
Closest point to Earth in transfer orbit	250 km
s/c orbit around Moon	$11 \cdot R_M$

**Table B.2:** Orbital data

### B.1.3 Spacecraft and material properties

In the following [Table B.3](#) are stored all the data related to the [s/c](#) and material properties.

Properties	
Spacecraft's Surface	$11.76 m^2$
SSAK absorvibity $\alpha$	0.12 [57, 60]
SSAK emissivity $\epsilon$	0.05 [57, 60]
Number of <a href="#">MLI</a> layers	20 + 2
Radiator's emissivity	0.91 [61]
Radiator's density	$2.707 kg/m^3$ [73]
Paint	$0.24 kg/m^2$ [74]
Kapton density	$0.0111 kg/m^2$ [74]
Thickness of 1 Kapton layer	0.0076 mm2 [57]

**Table B.3:** Spacecraft and material properties



## B.2 TCS - single-node computations

### B.2.1 Heat fluxes

First of all, the heat fluxes for each scenario must be computed as follows.

#### Solar Flux

The equation for the solar flux is the following [Equation B.1](#):

$$q_{sun_{sc}} = q_0 \left( \frac{r_{Earth}}{r_{sc}} \right)^2 \quad (\text{B.1})$$

where:

- $r_{Earth}$  is the mean distance between the Earth and the Sun
- $r_{sc}$  is the distance between the [s/c](#) and the Sun in Astronomical unit ([AU](#))

#### Albedo Flux

The equation for the albedo flux is the following [Equation B.2](#):

$$q_{albedo,body} = q_{sun_{sc}} a \cos(\theta) \left( \frac{R_{body}}{R_{orbit}} \right)^2 \quad (\text{B.2})$$

where:

- $R_{body}$  is radius of the object around which the [s/c](#) is orbiting
- $R_{orbit}$  is the radius of the orbit of the [s/c](#)
- $a$  is the albedo of the object around which the [s/c](#) is orbiting
- $\theta$  is the irradiance angle between the [s/c](#) and the body

#### Infrared Flux

The equation for the infrared flux is the following [Equation B.3](#):

$$q_{IR-body} = \sigma \varepsilon T_{body}^4 \left( \frac{R_{body}}{R_{orbit}} \right)^2 \quad (\text{B.3})$$

where:

- $\sigma$  is the Stefan-Boltzmann constant
- $\varepsilon$  is the emissivity of the [s/c](#)'s surface
- $T_{body}$  is the surface temperature of the object around which the [s/c](#) is orbiting
- $R_{body}$  is radius of the object around which the [s/c](#) is orbiting
- $R_{orbit}$  is the radius of the orbit of the [s/c](#)

## B.3 Heat Power

The second step is to exploit the heat fluxes computed before and compute the heat powers for each scenario. The sum of these heat powers , with the addition of the internal dissipated power, will give the total power to dissipate to the outer space for each scenario.



LUMINOUS

## Sun Power

$$Q_{sun-sc} = A_{absorbing} \alpha q_{sun-sc} \quad (\text{B.4})$$

where:

- $A_{absorbing}$  is the surface which faces the Sun
- $\alpha$  is the [s/c](#) solar absorvity
- $q_{sun-sc}$  the solar heat flux

## Albedo Power

$$Q_{albedo} = A_{body} F_{body-sc} \alpha K_a q_{albedo,body} \quad (\text{B.5})$$

where:

- $A_{body}$  is the surface of the single-node approximation
- $F_{body-sc}$  is the body-sc view factor, computed as in [Equation B.6](#)
- $\alpha$  is the [s/c](#) solar absorvity
- $K_a$  is the diffusion factor of the celestial body
- $q_{albedo,body}$  is the albedo heat flux

with:

$$F_{body-sc} = \frac{1}{2} \left[ 1 - \frac{\sqrt{\left(\frac{h_{orbit}}{R_{body}}\right)^2 + 2\frac{h_{orbit}}{R_{body}}}}{1 + \frac{h_{orbit}}{R_{body}}} \right] \quad (\text{B.6})$$

where:

- $h_{orbit}$  the altitude of the orbit where the [s/c](#) is placed
- $R_{body}$  the radius of the body around which the [s/c](#) is orbiting

## Infrared Power

$$Q_{IR} = A_{radiating} F_{body-sc} q_{IR-body} \quad (\text{B.7})$$

where:

- $A_{radiating}$ , which is equal to the total surface of the [s/c](#) for the approximation used
- $F_{body-sc}$  is the body-sc view factor, computed as in [Equation B.6](#)
- $q_{IR-body}$  is the infrared heat flux



## B.4 Temperature, radiators, heaters

### B.4.1 Spacecraft Temperature and radiators

Given the maximum heat received by the *s/c* computed with the formulas above and assumed its optical properties, it is possible to compute its temperature as in the following [Equation B.8](#):

$$T_{sc_{hot}} = \sqrt[4]{\frac{Q_{received_{hot}}}{\sigma * \epsilon_{MLI} * A_{body}}} \quad (\text{B.8})$$

If the *s/c* temperature is higher than the maximum one allowed by the on-board components, radiators are needed to dissipate heat in the deep space. In order to find the minimum radiators' surface it shall be considered that the radiators' area is to be subtracted by the total emitting area of the *s/c*. An optimisation can be conducted keeping the area of radiators as a variable, starting from an initial guess, as in the following [Equation B.9](#):

$$A_{rad_{min}} = Q_{received_{hot}} - \frac{\sigma * \epsilon_{MLI} * (A_{body} - A_{rad}) * T_{max}^4}{\sigma * \epsilon_{rad} * T_{max}^4} - A_{rad} \quad (\text{B.9})$$

where  $A_{rad}$  is the variable, with an initial guess of  $10m^2$ .

### B.4.2 Spacecraft Temperature and heaters

Given the maximum heat received by the *s/c* computed with the formulas above and assumed its optical properties, it is possible to compute its temperature as in the following [Equation B.10](#):

$$T_{sc_{cold}} = \sqrt[4]{\frac{Q_{received_{cold}}}{\sigma * [\epsilon_{MLI} * (A_{body} - A_{rad_{min}}) + \epsilon_{rad} * A_{rad_{min}}]}} \quad (\text{B.10})$$

If the *s/c* temperature is lower than the minimum one allowed by the on-board components, two options are available:

- If a passive thermal control is preferred, passive thermal louvers are an option, in order to cover a portion of the radiators' surface, in order to increase the heat retained inside the spacecraft.
- If louvers are not enough, or if the power consumption is not an issue in the cold case, heaters could be adopted. In this case, the power the heaters shall provide can be computed as in [Equation B.11](#):

$$Q_{heaters} = \sigma * [\epsilon_{MLI} * (A_{body} - A_{rad_{min}}) + \epsilon_{rad} * A_{rad_{min}}] * T_{min}^4 - Q_{received_{cold}} \quad (\text{B.11})$$

Note that in [Equation B.10](#) and [Equation B.11](#) louvers are not considered. In case they are adopted, the formulation of the areas shall be changed to take them into account.



## B.5 TCS - thermal network computations

### B.5.1 Sink temperature

The sink temperature, so the temperature of a node when it is insulated from everything except from space and the external fluxes it receives, can be computed as in the following [Equation B.12](#):

$$T_{sink} = \sqrt[4]{\frac{1}{\sigma} \left( \frac{\alpha_{SSAK}}{\varepsilon_{SSAK}} * q_{sun_{sc}} + \frac{\alpha_{SSAK}}{\varepsilon_{SSAK}} * q_{albedo,body} + q_{IR-body} \right)}; \quad (\text{B.12})$$

### B.5.2 View Factors

The view factor between the [SA](#) and the external surface 2 has been computed with the following ??:

$$F_{panels-node2} = \frac{1}{2} \left[ \left( 1 + \frac{h}{w} \right) - \sqrt{1 + \left( \frac{h}{w} \right)^2} \right] \quad (\text{B.13})$$

where w is the longest side of the solar panels, while h is half of the lenght of the side of the surface on which the [SA](#) are mounted.

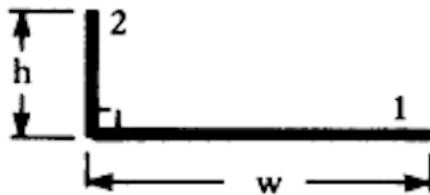


**Figure B.1:** View Factor between two perpendicular surfaces with an infinite extension in the direction normal to the paper

# Appendix C EPS sizing

## C.1 Preliminary analysis

The sizing process starts from the orbital profile of the mission. The distance from the Sun influences the power output of the solar arrays, since solar radiation lowers:

$$I = \frac{F_S}{D^2} \quad (\text{C.1})$$

being  $F_S=1368 \text{ W/m}^2$  the solar constant at 1 AU, and  $D$  the distance from the Sun, in AU. Maximum distance is obtained when the Moon is in opposition with respect to Earth and the [s/c](#) is in opposition with respect to the Moon at Earth aphelion, i.e.:

$$D_{max} = D_{aphelion} + D_{Earth-Moon} + R \quad (\text{C.2})$$

$D_{aphelion}$ [km]	$D_{Earth-Moon}$ [km]	$R$ [km]
1.52e8	405696	19118

**Table C.1:** Maximum distances

Nevertheless, the main figure of merit is Earth distance from the Sun, as [Table C.1](#) highlights.

The orbiter is designed to sustain 6 years of operative lifetime. Orbital radius, period, maximum time in eclipse and number of cycles are inherited from mission analysis. Power requests come from the analysis of the instruments which are supposed to be switched on in every mode. The maximum power request of each instrument is first margined with the proper Design Maturity Margin ([DMM](#)); then, the total power budget is margined with the System Level Margin ([SLM](#)) of 20% coming from ESA margins philosophy document. Please note that only the peak power request is considered in the sizing. From the secondary energy source viewpoint, this is directly translating into an overshooting of the capacity request, meaning that the imposed [DOD](#) shall be intended as an upper limit, i.e., the case in which all switched-on instruments are consuming the maximum power for the entire duration of the eclipse phase.

## C.2 Solar arrays sizing

Data regarding solar cells are collected in [Appendix D](#). Each solar array is intended to provide half of the total power request. The sizing scenario is the one for which peak power request in sunlight is maximum (the charging mode) and Sun distance is the maximum as well, at [EOL](#) -i.e., when degradation has depressed performance. The system is designed to be capable to provide the required output for a maximum [SAA](#) of 30 deg. Please note that, in nominal condition, such angle is not exceeding 1.5 deg (combining [ADCS](#) and [SADA](#) pointing error).

The specific power at [EOL](#) reads:

$$I_{EOL} = \varepsilon_{BOL} I(Id)(1 - dpy)T_{life} \cos(30\text{deg}) \quad (\text{C.3})$$

- $\varepsilon_{BOL}$  the efficiency at [BOL](#)
- $Id$  the inherent degradation
- $dpy$  the degradation per year

$Id$  and  $dpy$  are taken from [\[45\]](#).

The number of cells in series is given by:

$$N_{series} = \text{ceil}\left(\frac{V_{bus}}{V_{cell}}\right) \quad (\text{C.4})$$

- $V_{bus}$  the bus voltage
- $V_{cell}$  the cell voltage



$V_{bus}$  (28 V) is corrected with a +2 V to take into account voltage losses in the bus, and  $V_{cell}$  retrieved by datasheet. The area of the single solar array reads:

$$A = \frac{P_{array}}{I_{EOL}} \quad (\text{C.5})$$

Given the area of a single cell (from datasheet), the total number of cells can be retrieved. Since this number shall be an integer, it must be rounded, so the power output would be slightly major than the expected one. From the total number of cells and the number of cells in series, it is trivial to compute the number of strings; at the end of the sizing, one string is add for redundancy and better protection from lock-ups.

### C.3 Batteries sizing

For battery sizing both energy and power budget  $P_{ecl}$  shall be considered. The eclipse time  $T_{ecl}$  used in the sizing process is the longest one expected for the mission (as retrieved by mission analysis), margined of 5%.

The capacity to be provided is computed as:

$$C = P_{ecl} T_{ecl} \quad (\text{C.6})$$

The number of cells to be put in series is retrieved by employing [Equation C.4](#). This number fixes the voltage of the battery.

The capacity of the battery pack is given by:

$$C_{battery} = \frac{C}{(DOD)N_{battery}\varepsilon_{trans}} \quad (\text{C.7})$$

- DOD the nominal imposed DOD
- $N_{battery}$  the number of batteries (design choice)
- $\varepsilon_{trans}$  the transmission efficiency (97%, a typical value)

The final design features the minimum number of batteries (recall that one is fully redundant) and the minimum DOD to have a single string in the battery.

The electric charge capacity of each battery reads:

$$q_{battery} = \frac{C_{battery}}{V_{battery}} \quad (\text{C.8})$$

The real capacity of the string (and hence, of the battery, in this case) is:

$$C_{string} = \varepsilon_{pack} C_{cell} V_{battery} \quad (\text{C.9})$$

with  $\varepsilon_{pack}$  the packaging efficiency (taken to be 87%)

# Appendix D EPS datasheets

30% Triple Junction GaAs Junction Solar Cell Type: TJ Solar Cell 3G30C - Advanced (80µm)				
Design and Mechanical Data				
Base Material	GaInP/GaAs/Ge on Ge substrate			
AR-coating	$\text{TiO}_2/\text{Al}_2\text{O}_3$			
Dimensions	40 x 80 mm ± 0.1 mm			
Cell Area	30.18 cm <sup>2</sup>			
Average Weight	≤ 50 mg/cm <sup>2</sup>			
Thickness (without contacts)	80 ± 20 µm			
Contact Metallization Thickness (Ag/Au)	3 – 10 µm			
Grid Design	Grid system with 2 contact pads			
Electrical Data				
Average Open Circuit V <sub>oc</sub>	BOL	2,5E14	5E14	1E15
[mV]	2700	2616	2564	2522
Average Short Circuit I <sub>sc</sub>	[mA]	520.2	518.5	514.0
Voltage at max. Power V <sub>mp</sub>	[mV]	2411	2345	2290
Current at max. Power I <sub>mp</sub>	[mA]	504.4	503.2	500.6
Average Efficiency η <sub>base</sub> (1387 W/m <sup>2</sup> )	[%]	29.5	28.6	27.8
Average Efficiency η <sub>base</sub> (1353 W/m <sup>2</sup> )	[%]	29.8	28.9	28.1
Standard: CASOLBA 2005 (0.5-20MV1, etc). Spectrum: AM0 WRC = 1367 W/m <sup>2</sup> ; T = 28 °C @fluence 1MeV [e/cm <sup>2</sup> ]				
Acceptance Values				
Voltage V <sub>op</sub>	2350 mV			
Min. average current I <sub>op avg</sub> @ V <sub>op</sub>	505 mA			
Min. individual current I <sub>op min</sub> @ V <sub>op</sub>	475 mA			
Temperature Gradients				
Open Circuit Voltage	ΔV <sub>oc</sub> /ΔT↑	[mV/°C]	- 6.2	- 6.5
Short Circuit Current	ΔI <sub>sc</sub> /ΔT↑	[mA/°C]	0.36	0.33
Voltage at max. Power	ΔV <sub>mp</sub> /ΔT↑	[mV/°C]	- 6.7	- 6.8
Current at max. Power	ΔI <sub>mp</sub> /ΔT↑	[mA/°C]	0.24	0.20
@fluence 1MeV [e/cm <sup>2</sup> ]				
Threshold Values				
Absorptivity	≤ 0.91 (with CMX 100 AR)			
Pull Test	> 1.6 N at 45° welding test (with 12.5µm Ag stripes)			
Issue date: 2016-08-19	AZUR SPACE Solar Power GmbH Theresienstr. 2 74072 Heilbronn phone: +49 7131 67 2603 telefax: +49 7131 67 2727 e-mail: info@azurspace.com website: www.azurspace.com			
DB 0004148-00-01 Page 2 of 2	Certified Company ISO 9001 ISO 14001 OHSAS 18001			
Copyright © 2010 AZUR SPACE Solar Power GmbH	Space			

Figure D.1: AzurSpace 3G30C cells datasheet



Specifications	
Part Number	LP32975
Nominal Cell Weight	465 g (1 lb)
Dimensions	See details on back
Voltage Range	3.0 to 4.1 V
Nominal Voltage	3.6 V
Nominal Capacity	12 Ah at C/5 at 20°C (68°F)
Energy Density	285 Wh/L
Specific Energy	114 Wh/kg
Discharge Rates	Max constant current 96 A Max pulse current (<1 sec.) 180 A
Nominal Cell Impedance	2.5mΩ at 20°C (68°F)
Cycle Life (80% capacity measured at 0.5C discharge current at 20°C (68°F))	>2000 at 100% DOD
Standard Charging Method	Constant current 6 A (0.5C) to 4.1 V Constant voltage 4.10 V to 0.24 A (C/50)
Operating Temperature	-20 to 60°C (-4 to 140°F)
Storage Temperature	-40 to 60°C (-40 to 140°F)

Figure D.2: EaglePicher LP32975 cells datasheet

SPECIFICATIONS	
Parameter	Data
Output Step Size	0.0375 Degrees
Output Torque	8.4 Nm
Unpowered Holding Torque	4.9 Nm
Power	8.6 W
Operating Temperature Range	-30° C to +65° C
Mass	1.16 Kg
Slip Ring Complement	30 @ 2 amp derated capacity / 45 volts
Position Sensor	Potentiometer ±0.36 degree

Figure D.3: Moog Type 1 SADA datasheet



## EXAMPLES OF REPRESENTATIVE PCU CONFIGURATIONS

	Flagship-Class Mission <sup>1</sup>	Generic SmallSat Mission <sup>2</sup>	
Card Complement:	<ul style="list-style-type: none"><li>• 2 controller cards (dual string)</li><li>• 4 switch cards with 24 switches each</li><li>• 2 propulsion/pyrotechnics cards</li><li>• 1 solar array card</li><li>• 1 battery card</li></ul>	<ul style="list-style-type: none"><li>• 1 controller card (single string)</li><li>• 1 switch card with 24 switches</li><li>• 1 solar array card</li><li>• 1 battery card</li></ul>	<sup>1</sup> Actual values for an upcoming flagship-class mission with an undisclosed customer.
Power:	<ul style="list-style-type: none"><li>• Peak dissipation under peak load: &lt;50 W<ul style="list-style-type: none"><li>- Assuming 1,500 W peak spacecraft power, with 600 W from solar array and 900 W from battery</li></ul></li><li>• Dissipation under orbit-average load: &lt;35W<ul style="list-style-type: none"><li>- Assuming orbit-average spacecraft power demand of 500 W</li></ul></li></ul>	<ul style="list-style-type: none"><li>• Peak dissipation under peak load: &lt;35 W<ul style="list-style-type: none"><li>- Assuming 500 W peak spacecraft power, with 250 W from solar array and 250 W from battery</li></ul></li><li>• Dissipation under orbit-average load: &lt;30 W<ul style="list-style-type: none"><li>- Assuming orbit-average spacecraft power demand of 150 W</li></ul></li></ul>	<sup>2</sup> Representative values for a hypothetical small satellite mission.
Input Voltage:	• 28±6 VDC unregulated	• 28±6 VDC unregulated	
Mass:	• 25 kg	• 12 kg	
Dimensions (LxWxH):	• 32×37×23 cm	• 18×37×23 cm	
Quiescent Power:	• 20 W	• 20 W	

## SCALABLE HARDWARE CONFIGURATION

The innovative "by the slice" modular design of the Magellan PCU allows customers to choose only the mission-specific functionality and level of redundancy required, thereby optimizing mass, power and volume. For example, a generic smallsat mission requiring less than 750 W could be supported with four cards (controller, solar array, battery, switch).

- Controller card
- Switch card(s) (>99% switch efficiency)
- Solar array card (>98.5% efficiency @ 1.5 kW)
- Battery card
- Propulsion/pyrotechnics card

Enhanced functionality for more complex missions would require the inclusion of additional cards.

## RADIATION TOLERANCE

Total Ionizing Dose: >50 krad (Si)  
Single Event Latchup Threshold: 59 MeV·cm<sup>2</sup>/mg

## FLIGHT HERITAGE

- RADARSAT Constellation Mission (launched June 2019)
- Upcoming mission (undisclosed customer)

**Figure D.4:** Magellan Aerospace PCDU datasheet

# Appendix E Structures

Model	DVIA-UB350	DVIA-UB700
Platform Dimensions (L x W x H)	Custom-made	Custom-made
Maximum Load Capacity	350 kg	700 kg
Actuator	Electromagnetic Actuator	
Maximum Actuator Force	Vertical: 6 N, Horizontal: 3 N	Vertical: 12 N, Horizontal: 6 N
Degrees of Freedom	6 degrees	
Active Isolation Range	0.5 - 100 Hz	
Vibration Isolation $\geq$ 4 Hz.	$\geq$ 90%	
Input Voltage (V)	AC100 - 240V / 50 - 60 Hz / 1A	
Power Consumption (W)	Maximum 110W, <50 W in normal operation	
Operating Range	Temperature (°C)	5 - 50 °C
	Humidity (%)	20 - 90%

**Figure E.1:** Daeil systems isolator datasheet

# Appendix F PS datasheet

Typical Application	Apogee or Main delta V engine
Typical Operational Mode	Long duration burns: typically 3 x 5000 sec
Propellant	MON / Hydrazine
Thrust range	386 N to 470 N [87 lbf to 106 lbf]
Thrust at nominal inlet pressure	458 N [103 lbf]
Mixture Ratio Range	0.78 to 0.89 [oxidiser to fuel]
Mixture Ratio, nom inlet pressures	0.85 [oxidiser to fuel]
Specific Impulse	324 sec minimum
Total Impulse	13,200,000 Nsec
Propellant Throughput	4760 kg
Inlet Pressure Range	13 bara to 21 bara [190 psi to 300 psi]
Restarts Demonstrated	117 Chamber temp. <100°C [start], >1300°C [finish]
Maximum Duration Single Firing	>5,800 seconds performed in orbit
Cumulative Duration	>40,000 seconds demonstrated duration
Engine Mass	4.3 kg
Operating Temperature	1380°C maximum
Propellant Temperature	+10°C to +35°C
Storage Temperature	-53°C to +65°C
Storage Life	4 years
Operational Life	19 years
Reliability	0.995
Valve Type	2 off Solenoid, Single Seat, Redundant Coil
Qualified Valve Cycles	10,500 on/off cycles
Valve Voltage per coil	27.5 Vdc to 35.5 Vdc
Technology Readiness Level	TRL9

**Figure F.1:** Leros 1c datasheet



**Design**

Propellant	Hydrazine/MON	MMH/MON	MMH/MON	MMH/MON
Nominal Steady State Thrust	5 lbf (22N)	5 lbf (22N)	5 lbf (22N)	5 lbf (22N)
Feed Pressure	80 – 400 psia (5.5 – 27.6 bar)	60 – 400 psia (4.1 – 27.6 bar)	80 – 400 psia (5.5 – 27.6 bar)	39 – 320 psia (2.8 – 22.1 bar)
Nozzle Expansion	300:1	300:1	300:1	150:1/300:1
Nominal Mixture Ratio	0.85	1.61	1.65	1.61/1.65
Valve	Solenoid	Latching Torque Motor	Solenoid	Latching Torque Motor or Solenoid
Valve Power	41 watts max (2 coils wired in series)	6 watts max (Latch) 7 watts max (primary) 9 watts max (secondary)	41 watts max (2 coils wired in series)	6 watts max (Latch) 7 watts max (primary) 9 watts max (secondary) (Torque Motor) 15.6 watts max (solenoid)
Mass	1.7 lbm (0.77 kg)	1.4 lbm (0.64 kg)	1.5 lbm (0.68 kg)	1.4 – 2.0 lbm (0.64 – 0.91 kg)
Length	10.3 in (262 mm)	9.6 in (244 mm)	10.4 in (264 mm)	9.7-13.5 in (248 - 343 mm)
Chamber Material	Platinum/Rhodium Alloy	Platinum/Rhodium Alloy	Platinum/Rhodium Alloy	C-103

Performance	DST-11H	DST-12	DST-13	5 lbf
Specific Impulse	310 secs	302 secs	298 secs	288 secs/292 secs
Throughput	907 kg (2000 lbm)	1073 kg (2365 lbm)	637 kg (1404 lbm)	484 kg (1068 lbm)
Programs	Intelsat, BepiColombo, Wild Geese, Tenacious, GOES-R	AsiaSat 5, Telstar, Himawari, Turksat	NASA SDO	ETS-8, QZSS, Superbird-7, ST-2, WGS, Intelsat
Highlights	DST-11H provides highest performance available in a hydrazine/MON ACS Thruster	DST-12/13 Provides highest performance available in MMH/MON ACS Thruster		Engine has been in production for more than 30 years, with > 2000 delivered and flown

Figure F.2: Secondary bipropellants datasheet

**PERFORMANCE CHARACTERISTICS**

Engine	MONARC-1	MONARC-5	MONARC-22-6	MONARC-22-12	MONARC-90LT	MONARC-90HT	MONARC-445
Steady State Thrust	0.22 lbf (1N) @275 psia	1.0 lbf (4.5 N) @325 psia	5 lbf (22N) @275 psia	5 lbf (22N) @190 psia	20 lbf (90 N) @ 235 psia	26 lbf (116 N) @ 235 psia	100 lbf (445N) @ 275 psia
Feed Pressure	70 – 400 psia (4.8 – 27.6 bar)	80 – 420 psia (5.5 – 29.0 bar)	70 – 400 psia (4.8 – 27.6 bar)	70 – 400 psia (4.8 – 27.6 bar)	80 – 400 psia (5.5 – 27.6 bar)	80 – 370 psia (5.5 – 25.5 bar)	70 – 400 psia (4.8 – 27.6 bar)
Nozzle Expansion	57:1	135:1	60:1	40:1	40:1	50:1	50:1
Valve Power	18 watts	18 watts	30 watts	30 watts	72 watts	72 watts	58 watts
Mass	0.83 lbm (0.38 kg)	1.08 lbm (0.49 kg)	1.58 lbm (0.72 kg)	1.51 lbm (0.69 kg)	2.47 lbm (1.12 kg)	2.47 lbm (1.12 kg)	3.5 lbm (1.6 kg)
Engine Length/Exit Diam	5.2 in (13.3 cm) / .2 in (0.5 cm)	9.4 in (41.8 cm) / 1 in (2.5 cm)	8 in (20.3 cm) / 1.5 in (3.8 cm)	9 in (22.9 cm) / 1.2 in (5.3 cm)	12 in (30 cm) / 3.3 in (8.4 cm)	12 in (30 cm) / 3.3 in (8.4 cm)	16 in (41 cm) / 5.8 in (14.8 cm)
Specific Impulse	227.5 sec	226.1 secs	229.5 secs	228.1 secs	232.1 secs	234.0 secs	234.0 secs
Minimum Impulse Bit	0.0006 lbf-sec (2.6 mN-sec)	0.0007 lbf-sec (3.1 mN-sec)	0.07 lbf-sec (312m N-sec)	0.12 lbf-sec (526m N-sec)	0.04 lbf-sec (1.8 N-sec)	0.26 lbf-sec (1.16 N-sec)	2.59 lbf-sec (11.52 N-sec)
Total Impulse	25,000 lbf-sec (111,250 N-sec)	138,000 lbf-sec (613,852 N-sec)	120,000 lbf-sec (533,784 N-sec)	263,720 lbf-sec (1,173,085 N-sec)	786,000 (3,500,000 N-sec)	459,100 lbf-sec (2,042,178 N-sec)	1,250,000 lbf-sec (5,600,000 N-sec)
Pulses	375,000	205,000	230,000	160,000	50,000	70,000	12,000

Figure F.3: Monopropellants datasheet



## F.1 Pressurization system sizing

Here are the equations used to calculate the mass and volume of the pressurizing gas.

$$m_{gas} = \frac{p_{tank,in} V_{prop}}{\Re T_{tanks}} \left( \frac{\gamma_{gas}}{1 - p_{tank,in}/p_{press,in}} \right) \quad (\text{F.1})$$

$$V_{gas} = \frac{m_{gas} \Re T_{press}}{p_{press,in}} \quad (\text{F.2})$$

## F.2 Tank sizing

Here, the equations used to calculate the parameters related to the spherical tank are provided. The parameters of the cylindrical tanks were calculated by considering a cylinder with two hemispheres at the ends.

$$m_{tank,sphere} = \rho_{tank} \frac{3}{4} \pi \left( (r_{tank} + t_{tank})^3 - r_{tank}^3 \right) \quad r_{tank,sphere} = \left( \frac{3}{4} \frac{V_{tank}}{\pi} \right)^{\frac{1}{3}} \quad t_{tank,sphere} = \frac{P_{tank} r_{tank}}{2\sigma} \quad (\text{F.3})$$

# Appendix G OBDH datasheets

## Specifications

### Rad-tolerant RAD750®

Technology	0.25 $\mu$ m radiation-hardened bulk CMOS
Speed	110 to 132 MHz
Radiation-hardness	Total dose: 200 Krad (Si) SEU: <1.6 E-10 errors/bit-day (90 percent W. C. GEO) Latchup-immune
Performance	>260 Dhrystone 2.1 MIPS at 132 MHz
Temperature range	-55 degrees celsius to +125 degrees celsius
Packaging	360-pin ceramic package with column grid array (CGA)

### Rad-hard RAD750®

Technology	0.15 $\mu$ m radiation-hardened bulk CMOS
Speed	200 MHz
Radiation-hardness	Total dose: 1Mrad (Si) SEU: <1.6 E-10 errors/bit-day (90 percent W. C. GEO) Latchup-immune
Performance	>400 Dhrystone 2.1 MIPS at 200 MHz
Temperature range	-55 degrees celsius to +125 degrees celsius
Packaging	360-pin ceramic package with CGA

**Figure G.1:** RAD750 PowerPC microprocessor datasheet

## Specifications

Form factor	CompactPCI 6U (233 mm x 160 mm) CompactPCI 6U-220 (233mm x 220mm) Weight: 1000 to 1220 grams, varies with memory
Memory	SRAM: 4 to 48 MB EEPROM: 4 MB
Radiation-hardness	Total dose: >100 Krad (Si) SEU: 1.9 E-4 errors/card-day (90 percent W. C. GEO) varies with orbit Latchup-immune
Performance	>260 Dhrystone 2.1 MIPS at 132 MHz 4.3 SPECint95 4.6 SPECfp95 at 132 MHz
Power supply	– 5 volts $\pm$ 10 percent and 3.3 volts $\pm$ 5 percent (2.5 volts generated via onboard regulator)
Power dissipation	11 to 14 watts
Rail temperature range	-28 degrees celsius to +70 degrees celsius

**Figure G.2:** RAD750 6U CompactPCI single-board computer datasheet

# Bibliography

- [1] J. F. Cooper, S. R. Habbal, B. Boe, V. Angelopoulos, D. G. Sibeck, N. Paschalidis, E. C. Sittler, L. Jian, and R. M. Killen. 8. *Frontiers in Astronomy and Space Sciences*, 10.
- [2] GE Brueckner, RA Howard, MJ Koomen, CM Korendyke, DJ Michels, JD Moses, DG Socker, KP Dere, PL Lamy, A Llebaria, et al. The large angle spectroscopic coronagraph (lasco) visible light coronal imaging and spectroscopy. *The SOHO mission*, pages 357–402, 1995.
- [3] Renee P Dudley, Alexander Krimchansky, Sivakumara K Tadikonda, Arnaud F Thernisien, Rebecca A Baugh, Melissa Dahya, Dimitris Vassiliadis, and Clarence Korendyke. Compact coronagraph (ccor) accommodation on goes-u. Technical report, 2023.
- [4] CJ Eyles, GM Simnett, MP Cooke, BV Jackson, A Buffington, PP Hick, NR Waltham, JM King, PA Anderson, and PE Holladay. The solar mass ejection imager (smei). *Solar physics*, 217:319–347, 2003.
- [5] I. G. Usoskin. A history of solar activity over millennia. *Living Reviews in Solar Physics*, 14(1):3, 2017.
- [6] B. C. Low. Solar activity and the corona. *Solar Physics*, 167:217–265, 1996.
- [7] NASA. Solar activity, 2012. <https://www.nasa.gov/solar-cycle-progression-and-forecast/>.
- [8] A. K. Singh and A. Bhargawa. Predictions for solar cycles 25 & 26: a substantial weakening trend in solar activity. . Held 28 January-4 February, 43:1044, 2021.
- [9] ECSS Secretariat. Ecss-e-10-04a (space environment). Technical report, ESA Publications Division, 2008.
- [10] B. De Saedeleer and J. Henrard. The combined effect of j2 and c22 on the critical inclination of a lunar orbiter. *Advances in Space Research*, 37(1):80–87, 2006.
- [11] T. Nie and P. Gurfil. Lunar frozen orbits revisited. *Celestial Mechanics and Dynamical Astronomy*, 130(10):61, 2018.
- [12] S. Tzirtzi, K. Tsiganis, and H. Varvoglis. Effect of 3rd-degree gravity harmonics and earth perturbations on lunar artificial satellite orbits. *Celestial Mechanics and Dynamical Astronomy*, 108:389–404, 2010.
- [13] P. J. Coleman Jr, B. Lichtenstein, C. Russell, L. Sharp, and G. Schubert. Magnetic fields near the moon. In *Lunar and Planetary Science Conference Proceedings*, volume 3, page 2271, 1972.
- [14] Lunar and Planetary Institute. The lunar wake as a unique plasma physics laboratory”. [https://www.lpi.usra.edu/meetings/LEA/whitepapers/Farrell\\_NAC\\_wake\\_farrell.pdf](https://www.lpi.usra.edu/meetings/LEA/whitepapers/Farrell_NAC_wake_farrell.pdf).
- [15] S. Xu, A. R. Poppe, J. S. Halekas, D. L. Mitchell, J. P. McFadden, and Y. Harada. Mapping the lunar wake potential structure with artemis data. *Journal of Geophysical Research: Space Physics*, 124(5):3360–3377, 2019.
- [16] P. Giles. Time-distance measurements of subsurface rotation and meridional flow. <http://soi.stanford.edu/papers/dissertations/giles/thesis/PDF/>, 1998.
- [17] Sebastian Doroba, David Canales Garcia, Hancheol Cho, Rasika Kale, Octavi Fors, Stephen Eikenberry, Andrea Richichi, and Jose Gomez. Leveraging the moon and stable libration point orbits around l4/l5 to observe the solar corona. 2023.
- [18] F. Topputo. On optimal two-impulse earth-moon transfers in a four-body model. *Celestial Mechanics and Dynamical Astronomy*, 117:279–313, 2013.
- [19] Roberto Armellin, Pierluigi Di Lizia, M Rasotto, G Di Mauro, and M Landgraf. Disposal strategies for spacecraft in lagrangian point orbits. In *The 24th AAS/AIAA Space Flight Mechanics Meeting*, pages 26–30, 2014.
- [20] NASA. Intuitive machines 1 (odysseus). <https://nssdc.gsfc.nasa.gov/nmc/spacecraft/display.action?id=IM-1-NOVA>, 2024.



- [21] ULA. Vulcan. <https://www.ulalaunch.com/rockets/vulcan-centaur>.
- [22] Arianespace. Ariane 6 user's manual. [https://www.arianespace.com/wp-content/uploads/2021/03/Mua-6\\_Issue-2\\_Revision-0\\_March-2021.pdf](https://www.arianespace.com/wp-content/uploads/2021/03/Mua-6_Issue-2_Revision-0_March-2021.pdf), 02 2021.
- [23] Space-X. Capabilities services. <https://www.spacex.com/media/Capabilities&Services.pdf>.
- [24] Joey Roulette. Vulcan rocket's debut brings long-awaited challenge to spacex dominance. <https://www.reuters.com/technology/space/vulcan-rockets-debut-brings-long-awaited-challenge-spacex-dominance-2024-01-1#:~:text=The%20starting%20price%20for%20a,sometimes%20more%20for%20Pentagon%20missions.,> 01 2024.
- [25] Rich Smith. Europe complains: SpaceX rocket prices are too cheap to beat. <https://www.fool.com/investing/2018/06/02/europe-complains-spacex-rocket-prices-are-too-chea.aspx>.
- [26] Falcon9-block5. [https://it.wikipedia.org/wiki/Falcon\\_9\\_Block\\_5](https://it.wikipedia.org/wiki/Falcon_9_Block_5).
- [27] Jeff Foust. Vulcan centaur launches peregrine lunar lander on inaugural mission. <https://spacenews.com/vulcan-centaur-launches-peregrine-lunar-lander-on-inaugural-mission/#:~:text=%20United%20Launch%20Alliance%27s%20Vulcan%20Centaur,designated%20Cert%2D1%20by%20ULA.>, 01 2024.
- [28] Space-X. Falcon9. <https://www.spacex.com/vehicles/falcon-9/>.
- [29] Jeff Foust. Impulse space announces plan to develop high-energy kick stage. 2024.
- [30] eoPortal.org. Soho (solar and heliospheric observatory), quick facts. <https://www.eoportal.org/satellite-missions/soho>.
- [31] [https://www.airbus.com/sites/g/files/jlcbta136/files/2022-02/ScE-AVIONICS-ASTRIX120v3\\_2022.pdf](https://www.airbus.com/sites/g/files/jlcbta136/files/2022-02/ScE-AVIONICS-ASTRIX120v3_2022.pdf).
- [32] <https://www.jena-optronik.de/products/star-sensors/astro-xp.html>.
- [33] J. Pritchard, K. Simon, C. Dowd, and E. Joshi. Solar power concentrators for space applications. *PAM Review Energy Science & Technology*, 3:2–26, 2016.
- [34] Carina Ludwig and Michael Dreyer. Analyses of cryogenic propellant tank pressurization based upon ground experiments. In *AIAA SPACE 2012 Conference & Exposition*, page 5199, 2012.
- [35] Walter Tam, Ian Ballinger, and Don Jaekle. Conceptual design of space efficient tanks. In *42nd AIAA/ASME/SAE/ASEE Joint Propulsion Conference & Exhibit*, page 5058, 2006.
- [36] D JAEKLE, JR. Propellant management device conceptual design and analysis-vanes. In *27th Joint Propulsion Conference*, page 2172, 1991.
- [37] Margin philosophy for science assessment studies. [https://sci.esa.int/documents/34375/36249/1567260131067-Margin\\_philosophy\\_for\\_science\\_assessment\\_studies\\_1.3.pdf](https://sci.esa.int/documents/34375/36249/1567260131067-Margin_philosophy_for_science_assessment_studies_1.3.pdf).
- [38] W. Wertz. *Space Mission Analysis and Design*. Springer, 1999.
- [39] ESA. Europe's access to deep space. [https://esamultimedia.esa.int/multimedia/esoc\\_esoc\\_newnorcia\\_brochure.pdf](https://esamultimedia.esa.int/multimedia/esoc_esoc_newnorcia_brochure.pdf), 2007.
- [40] ITU Regulation. *HANDBOOK ON SPACE RESEARCH COMMUNICATION*. International telecommunication Unit, 2017.
- [41] V. Sanchez et al. Measurement of bepicolombo mission medium gain antenna parameters under realistic thermal conditions. *International Journal of Microwave and Wireless Technologies*, 2017.
- [42] S. Madry J. N. Pelton and S. Camacho-Lara. *Handbook of Satellite Applications*. Springer, 2013.
- [43] C. G. Marirrodriga et al. Solar orbiter: Mission and spacecraft design. *Astronomy and Astrophysics*, 2020.
- [44] <https://satsearch.co/products/endurosat-x-band-transmitter>.



- [45] J. R. Wertz, D. F. Everett, and J. J. Puschell. *Space Mission Engineering: the New SMAD*. Microcosm Press, 2011.
- [46] A. Baiju and M. Yarema. Status and challenges of multi-junction solar cell technology. *Frontiers in Energy Research*, 10:971918, 2022.
- [47] K. B. Chin, E. J. Brandon, R. V. Bugga, M. C. Smart, S. C. Jones, F. C. Krause, W. C. West, and G. G. Bolotin. Energy storage technologies for small satellite applications. *Proceedings of the IEEE*, 106(3):419–428, 2018.
- [48] E. Gaddy, M. Ballarotto, C. Drabenstadt, J. Nichols, M. Douglas, B. Spence, R. A. Stall, C. Sulyma, and P. Sharps. Transformational solar array final report. Technical report, 2017.
- [49] R. Verduci, V. Romano, G Brunetti, N. Yaghoobi, A. Di Carlo, G. D’Angelo, and C. Ciminelli. Solar energy in space applications: review and technology perspectives. *Advanced Energy Materials*, 12(29):2200125, 2022.
- [50] S. Wojtczuk, P. Chiu, X. Zhang, D. Derkacs, C. Harris, D. Pulver, and M. Timmons. Ingap/gaas/ingaas 41% concentrator cells using bi-facial epigrowth. In *2010 35th IEEE Photovoltaic Specialists Conference*, pages 001259–001264. IEEE, 2010.
- [51] P. Fortescue, G. Swinerd, and J. Stark. *Spacecraft systems engineering*. John Wiley & Sons, 2011.
- [52] R. M. Ambrosi, H. Williams, E. J. Watkinson, A. Barco, R. Mesalam, T. Crawford, C. Bicknell, P. Samara-Ratna, D. Vernon, N. Bannister, et al. European radioisotope thermoelectric generators (rtgs) and radioisotope heater units (rhus) for space science and exploration. *Space Science Reviews*, 215:1–41, 2019.
- [53] A. D. Pathak, S. Saha, V. K. Bharti, M. M. Gaikwad, and C. S. Sharma. A review on battery technology for space application. *Journal of Energy Storage*, 61:106792, 2023.
- [54] D. Mourembles, B. Buergler, L. Gajewski, A. Cooke, and C. Barchasz. Li-s cells for space applications (lissa). In *2019 European Space Power Conference (ESPC)*, pages 1–5. IEEE, 2019.
- [55] G. Palissat, L. Farhat, and J. Carreira. Supercapacitors for space applications: trends and opportunities.
- [56] Jesus Gonzalez-Llorente, Aleksander A Lidtke, Ken Hatanaka, Lakhdar Limam, Isai Fajardo, and Kei-Ichi Okuyama. In-orbit feasibility demonstration of supercapacitors for space applications. *Acta Astronautica*, 174:294–305, 2020.
- [57] M.M. Finckenor. Multilayer insulation material guidelines. <https://ntrs.nasa.gov/api/citations/19990047691/downloads/19990047691.pdf>, 04 1999.
- [58] T. Flecht. Thermal modelling of the picsat nanosatellite platform and synergetic prestudies of the circus nanosatellite. <https://www.diva-portal.org/smash/get/diva2:1039610/FULLTEXT01.pdf>, 09 2016.
- [59] E. L. Christiansen. Handbook for designing mmod protection. <https://ntrs.nasa.gov/api/citations/20090010053/downloads/20090010053.pdf>, 01 2009.
- [60] Dunmore. Aluminized kapton® film. <https://www.dunmore.com/products/aluminized-polyimide-film.html>.
- [61] AZ Technology. Az-93. <https://www.aztechnology.com/product/1/az-93>.
- [62] <https://www.rocketlabusa.com/assets/Uploads/Rocket-Lab-12-Nms-RW4-RW5-reaction-wheel-datasheet.pdf>.
- [63] <https://www.solar-mems.com/wp-content/uploads/2020/04/Solar-MEMS-SSOC-D60.pdf>.
- [64] <https://www.arcsec.space/web/sites/default/files/2023-07/arcsec%20Sagitta%20star%20tracker%20Datasheet%20V2.0.pdf>.
- [65] Space X. <https://www.spacex.com/media/falcon-users-guide-2021-09.pdf>. Technical report, Space Exploration Technologies Corps, 2021.
- [66] Flight Gobal. <https://www.flightglobal.com/nasa-selects-tuned-mass-dampers-to-solve-ares-i-oscillation-problem/82336.article>. *Flightglobal.com*, 2008.
- [67] PolyK PA USA. Electroactive polymer eap actuator: Pvdf piezoelectric film. <https://piezopvdf.com/eap-actuator-pvdf-piezoelectric-film/>.



- [68] Piezo systems inc. Piezo amplifier datasheet. <https://info.piezo.com/hubfs/Manuals/PSI-catalog.pdf>.
- [69] <https://www.usinflationcalculator.com>.
- [70] Jet Propulsion Laboratory. Joint emissivity database initiative. <https://emissivity.jpl.nasa.gov>.
- [71] H. Ren, J. Nie, J. Dong, R. Liu, W. Fa, L. Hu, and W. Fan. Lunar surface temperature and emissivity retrieval from diviner lunar radiometer experiment sensor. *Earth and Space Science*, 8(1):e2020EA001436, 2021.
- [72] NASA. Solar system temperatures. <https://science.nasa.gov/resource/solar-system-temperatures/>, 09 2023.
- [73] N. Iwata, S. Nakanoya, N. Nakamura, N. Takeda, and F. Tsutsui. Thermal performance evaluation of space radiator for single-phase mechanically pumped fluid loop. *Journal of Spacecraft and Rockets*, 59(1):225–235, 2022.
- [74] Charles D. Brown. Elements of spacecraft design. <https://doi.org/10.2514/4.861796>, 01 2002.

